Silicon Micromachined Sensors and Actuators for Fluid Mechanics Applications

Thesis by
Chang Liu

In Partial Fulfillment of the Requirements
for the Degree of
Doctor of Philosophy

California Institute of Technology
Pasadena, California

1996

(Defended December 6, 1995)

Approved:

.....

Chairman, date

.....

.....

.....

To my beloved parents

Acknowledgements

It is my great pleasure to acknowledge the many people who have offered me guidance, help, support and entertainment throughout my academic career at the California Institute of Technology.

First I would like to thank my academic advisor, Prof. Yu-Chong Tai. Prof. Tai admitted me into this wonderful micro world, an academic field of my heart's desire. Without his inspiration, expert advise, understanding, patience and support, I would never have become successful in this field and fully enjoyed my Caltech years. His influence on me will be felt for a long way to come.

I thank many other professors who have guided me on various academic and career matters. Prof. Chih-Ming Ho at the MANE department of UCLA and Dr. Denny K. Miu at Caltech have been very understanding and patient in helping me with many questions and difficulties.

I would like to thank Thomas Tsao who, as my research partner, has contributed tremendously to the success of many projects discussed in this thesis. The technical capacity, patience, un-selfishness and sense of humor he has demonstrated during our collaboration is whole-heartedly appreciated by me.

I thank fellow members of the project teams, especially Mr. Fukang Jiang, Dr. Steve Tung, Dr. Jin-Biao Huang, Dr. Jeremy Leu, Mr. Bhusan Gupta, Mr. Raanan Miller, Mr. Amish Desai, Mr. Vincent Lee and Mr. Charles Grosjean. My part of the project would never be complete without their parallel efforts. Also, special thanks go to Dr. Denny K. Miu and Dr. Weilong Tang, for sharing with me the Permalloy electroplating technique they have developed.

I am grateful to Mr. Trevor Roper at the Micromachining Laboratory for the skillful technical support he has provided to the whole lab. Without his diligent and expert work (including *magic touches*), all projects will never be finished so quickly and

successfully. Collaboration with Trevor has always been an enriching and fun-filled experience for me.

I would like to thank members of my thesis defense committee: Prof. Erik Antonsson, Prof. Rodney Goodman, Prof. David Rutledge and Prof. Theodore Wu. I truly appreciate their interest in my thesis work and their effort in helping me improve the quality of my dissertation. I am also indebted to Prof. Ho, John Wright, Tom Tsao and Fukang Jiang for their thorough proof-reading of my thesis.

I thank Dr. Svetlana Tatić-Lučić, for her wonderful technical collaboration and friendship. In many ways she have been an example for me to learn from. Ceca, I enjoyed the years when we were office-mates (thank you for always answering the phone!), and I wish peace and harmony will return to your home country.

I deeply thank members, past and present, of the Caltech micromachining group, for their technical collaboration and friendship. Each and every individual has inspired and influenced me with their own good traits. It has always been my privilege and pleasure to work in such a highly talented and motivated group.

I deeply appreciate the work of Ms. Janice Tucker, secretary of Prof. Tai. Janice, you have always been there for me and every other member of the group; our everyday life would have been a lot harder were not for your constant support. Thank you.

I owe my precious Caltech education and experiences to the generous tuition scholarship that the institute has provided for the past five years. My previous and current research projects have received financial support from Topometric Corp., BEI Corp., the Air Force Office of Scientific Research and the Advanced Research Programs Agency (ARPA).

I understand fully that my life and career is built on the patience and support from my parents and family. Long before my college and graduate-school years, my parents taught me important lessons about life through words and examples. My past, current and future achievement will forever be my tribute to their un-conditional love.

Silicon Micromachined Sensors and Actuators for Fluid Mechanics Applications

by

Chang Liu

In Partial Fulfillment of the
Requirements for the Degree of
Doctor of Philosophy

Abstract

The major contributions of this thesis are the developments of silicon micromachined flow shear-stress sensors and magnetic actuators, together with original studies on two fundamental issues of micro fabrication. Sensors and actuators applications in two fluid-mechanics projects have been successfully demonstrated.

Micro shear-stress sensors utilize boundary-layer thermal transfer principles. For the proposed fluid-mechanics applications these sensors must have higher sensitive compared with conventional sensors, among other requirements. This has been realized by implementing a unique vacuum-sealed cavity which greatly reduces heat loss to the substrate silicon.

Fluid applications present unique challenges to micromachined actuators: they must achieve large out-of-plane motion and withstand large forces. We have developed two types of magnetic actuators that fit these requirements. The first type is based on interaction between the magnetic dipole moment of a current-carrying coil and an external magnetic field. A second-type uses the torque generated by an electroplated Permalloy ($Ni_{80}Fe_{20}$) plate inside an external magnetic field.

The two fundamental micro-fabrication issues are the reactive sealing of cavities and the magnetic-levitation assisted release of surface structures. We have conducted systematic experiments to determine the dependance of sealing performance on the test-structure geometric parameters, sealing materials and other factors. Release/drying of micro actuators, with their large surface areas, is especially challenging. The idea for magnetic-levitation assisted release is obtained while we were developing the Permalloy magnetic actuator. Magnetic forces counteract the surface tension forces during the drying to avoid structure stiction to the substrate. Original results from these fundamental studies add to the general micromachining knowledge base.

The applications of developed sensors and actuators are demonstrated in two fluid-mechanics projects. In the first, we explore a unique scheme for active drag reduction, which is possible only by using a Micro Electro Mechanical System (MEMS). The MEMS consists of an array of shear-stress sensors, actuators and embedded neural-network (NN) circuitry. The goal of the second project is to achieve enhanced maneuverability of delta-wings using MEMS devices. Shear-stress sensors are successfully applied to identify the flow separation lines along the delta-wing's leading edges. Permalloy magnetic actuators interact with the leading-edge flow for controlling the wing motion.

Contents

List of Figures

List of Tables

Chapter 1

INTRODUCTION

1.1 Silicon Micromachining and MEMS

Silicon micromachining is the science and technology of constructing integrated, three-dimensional electro-mechanical structures, with characteristic length scales in the micrometer to millimeter range, using fabrication technologies derived from and compatible with integrated circuit (IC) fabrication. Micromachining provides the technological foundation for Micro Electro Mechanical Systems (MEMS). A MEMS contains integrated electro-mechanical structures (sensors and actuators) and electronic IC circuitry; these components are built on single chips or within hybrid packages.

The micromachining field has been undergoing rapid growth during the past ten years. A number of mile-stone events include a 1984 paper by Kurt Petersen titled "Silicon as a Mechanical Material" [91], a first demonstration of an electrostatic micromotor in 1989 [109], an electrostatic comb-drive mechanism for polysilicon micro devices [115] and a micro mirror array for image projection by Texas Instruments [98]. MEMS facilitates and inspires fundamental scientific research as well; for example, studies of fluid flows in micro flow channels have been conducted [73]. It is predicted that application of micromachined devices in such fields as biology (e.g., cell and DNA handling), optics (e.g., micro optical bench, displays and imagers), data storage and

	Single crystal Silicon	Stainless Steel	Silicon nitride	Permalloy (Ni 80 Fe 20)
Yield strength (10^9 N/m^2)	7	2.1	14	1.52
Knoop hardness (kg/mm^2)	850	130	3480	580
Young's modulus (10^{11} N/m^2)	1.3-1.9	0.7	3.85	-
Thermal conductivity (W / cm ^oC)	1.57	1.38	0.19	-
Thermal expansion coefficient (10^{-6} /^oC)	2.33	17.3	0.8	-

Table 1.1: Mechanical properties of various materials.

micro-instrumentation will undergo quantum advancements in the future [92].

Nowadays, silicon, polysilicon and silicon compound materials are predominantly used for micromachining. A comparison of selected mechanical properties of silicon, silicon nitride, stainless steel and Permalloy [1] is shown in Table. 1.1. For example, silicon has larger yield strength, hardness, Young's modulus and thermal conductivity compared with those of the stain-less steel material. The single crystalline silicon structure can have inherently large Q factors. As sizes of structures are reduced, it has been predicted that fatigue strength could also improve. On the other hand, silicon is also a brittle material: the fracture strain for single crystal silicon and poly-crystalline silicon is below 2%.

Several other types of materials can also be used for micromachining; a partial list of those include quartz [25], diamond [56], silicon carbide [120] and gallium arsenide [46].

1.1.1 Advantages of Micromachining and MEMS

Micromachined structures and devices have the following advantages:

1. **Small size.**

Characteristic lengths of micromachined devices range from micrometers (10^{-6}m) to

[1]Properties of Permalloy material is obtained from [78]

millimeter. Small sizes potentially translate into reduced real-estate requirements and smaller mass of functional units. As a result, mechanical, electrical and thermal response times of MEMS are much smaller compared with those of macro-scaled devices. Some important scaling rules of physical characteristics are illustrated. Let L be the length parameter, then according to [28], the mass of a structure scales by

$$mass \propto L^3 \tag{1.1}$$

and the bending stiffness of a rod scales by [2]

$$stiffness \propto L \tag{1.2}$$

The mechanical vibrational frequency, described in lumped model, would therefore scale by

$$frequency \propto \sqrt{\frac{stiffness}{mass}} \propto L^{-1}. \tag{1.3}$$

Similar to the mechanical frequency response, general thermal response frequency ($\propto L^{-3/2}$) and electrical oscillation frequency ($\propto L^{-1}$) both increase when the dimension L is reduced.

An important fact is that the ratio of an object's surface area ($\propto L^2$) to its volume ($\propto L^3$) increases substantially with a diminishing L, because

$$\frac{area}{volume} \propto L^{-1} \tag{1.4}$$

This relationship implies that surface effects (e.g., stiction and friction) will have a more important role for determining the performance of micro devices, whereas volume effects (e.g., gravitation and inertia) are relatively more important in macro devices.

[2] stiffness $\propto$ moment of inertia / length^3 $\propto$ L^4 / L^3

2. **Three-dimensional geometry and multi-degrees-of-freedom of motion.**
Integrated electronics elements have fixed positions within a shallow layer atop the silicon substrate. Micro mechanical structures and devices, on the other hand, are three-dimensional and can achieve multiple degrees of motion freedom. Using a large number of existing micromachining techniques (briefly described in the next section), structure heights ranging from tens of angstrom to hundreds of micrometers can be realized. Movements in many degrees of freedom have been demonstrated using previously developed micro structures: micro sliders, for in-plane linear translation, micro motors for in-plane rotation, flap-action actuators and hinged micro structures for out-of-plane rotation, and symmetrically suspended structures for out-of-plane translation.

3. **Compatibility with microelectronics (IC).**
Micromachined sensors and actuators are fabricated using a set of processing tools compatible with IC fabrication. This makes integration of mechanical and electrical components at the chip level possible. Large number of devices can be batch fabricated using photolithography techniques. From the stand-point of industrialization, micromachined structures, devices and systems have the potential of greatly reducing production cost and improving performance.

1.1.2 Micro Fabrication Techniques

Silicon micro fabrication techniques are mainly categorized into bulk micromachining and surface micromachining.

Bulk micromachining (Fig. 1-1) involves using crystal-orientation-dependant, deep substrate (bulk) etching to realize free-standing mechanical structures (diaphragms, suspension beams, etc.). Wet chemical etchant such as ethylenediamine pyrocatechol

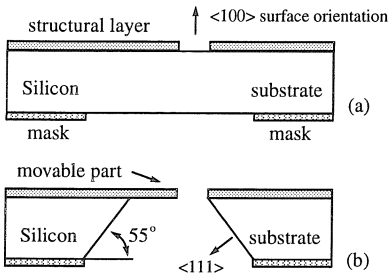

Figure 1-1: Schematic diagram of bulk-micromachining technique used to create a movable structure. (a) A $< 100 >$ oriented, single crystal silicon wafer with patterned silicon nitride on both sides; (b) using EDP etch, a cavity is created on the back-side and the structure on the front-side is freed.

(EDP), potassium hydroxide (KOH), hydrofluoric acid/nitric acid/acetic acid (HNA) and tetramethyl ammonium hydroxide (TMAH) are typically used. The etch-rate dependence on crystal planes and impurity doping levels vary for different etchant [91]. Some complex three-dimensional geometries can be realized by adopting proper mask shapes and etching sequences [54, 9]. Shown in Fig. 1-2 is an array of Si pyramids created using EDP, which is an isotropic etchant with slowest etch rate in the $< 111 >$ crystal orientation; each pyramid (7 μm tall) is bounded by four (111) crystalline planes [72]. Bulk micromachining techniques have been successfully applied in making several types of commercial sensors, for measuring thermal radiation, pressure and acceleration.

Surface Micromachining (Fig. 1-3), on the other hand, performs chemical etching and forms micro structures within a very thin (typically $<10\mu$m) layer on the substrate surface. Here, *Sacrificial-layer etching* is a key technique to realize free-standing structures. In this, structural layers are first deposited over a sacrificial layer; structures become free after the sacrificial layer is removed by wet or dry (plasma) chemical etching. Low Pressure Chemical Vapor Deposited (LPCVD) phosphosilicate glass (PSG), a phosphorous-doped (4-8 wt %) silicon dioxide, is the most commonly used sacrificial layer. In this case, 49% hydrofluoric acid (HF) is an effective etchant; its etch rate on PSG is on the order of 1 micrometer per minute, faster than its etch

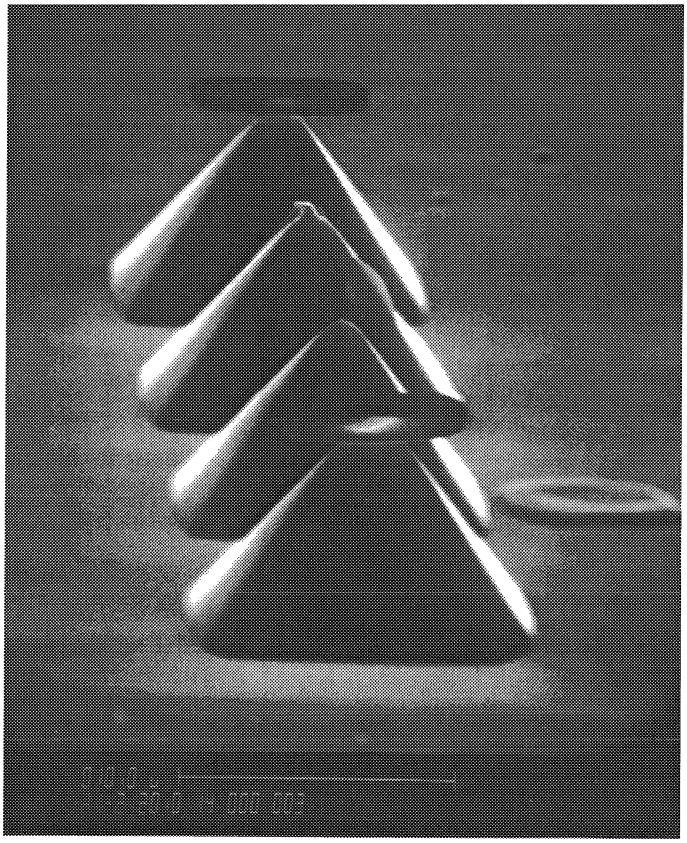

Figure 1-2: An array of pyramidal-shaped micro tips formed using EDP chemical etching. The flat plates on some tips are remaining etch masks.

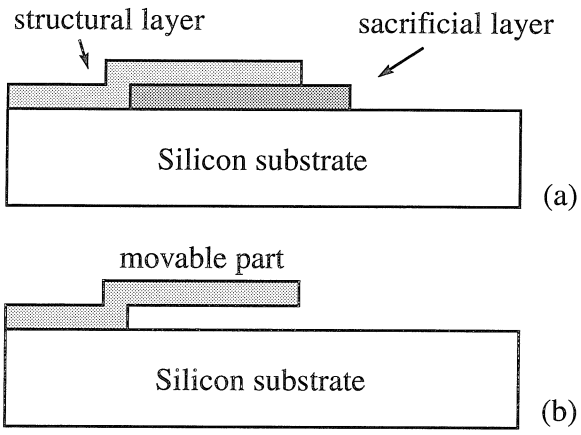

Figure 1-3: Schematic diagram of surface-micromachining technique used to create a free-standing structure over a wafer surface. (a) Patterned structural layer lies over the sacrificial layer; (b) after removal of the sacrificial-layer, the mechanical structure is free.

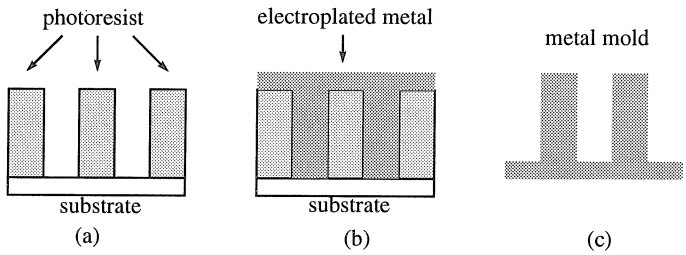

Figure 1-4: A schematic diagram of LIGA micromachining. (a) Thick photoresist is patterned using deep X-ray lithography; (b) metal electroplating fills cavities; (c) the finished metal parts extracted.

rates on silicon nitride and silicon by several orders of magnitude [74]. A number of microstructures made from poly-crystalline silicon and polysilicon/silicon nitride composite layers have been demonstrated including, for example, pin joints, gears, springs, sliders and resonant structures [115]. Metals (aluminum, copper, etc.) and organic polymers (photoresist, polyimide, etc.) have also been reported as sacrificial materials.

Other micro-fabrication techniques include fast prototyping (using laser or focused

ion beams) [56, 112], wafer-to-wafer bonding [121] and electroplating [58]. LIGA [3] is a hybrid-type technology using established planar processing sequences together with metal electroplating to produce metal structures with high aspect ratios. In some cases, finished metal products can be further used as master molds. Today's LIGA structures can be as thick as 500 μm and only several micrometers-wide in some parts. However, the LIGA process requires lithography with a synchrotron-based, deep X-ray beam source, limiting its accessibility.

1.2 Fluid Mechanics Concepts

1.2.1 Reynolds and Mach numbers

Flow over a surface is typically divided into three regimes: laminar, transitional and turbulent. In the laminar regime, flow particles move in smooth paths; interchange of momentum between layers, or *laminas*, is through molecule motion. The turbulent flow, on the other hand, has very erratic motion of fluid particles with a large transverse interchange of momentum. The nature of the flow, i.e., whether laminar or turbulent, and its relative position along a scale indicating the relative importance of turbulent to laminar tendencies, are characterized by the *Reynolds number*. The Reynolds number is defined as

$$Re = \frac{U_\infty l \rho}{\mu} \tag{1.5}$$

where U_∞ is a characteristic velocity of a flow field, l a characteristic length, ρ the density of the flow media, and μ the *dynamic viscosity*. The *kinematic viscosity*, ν,

[3] LIGA (Fig. 1-4) is the German word for *LIthographie* (lithography), *Galvanofornung* (electroplating) and *Abformund* (molding).

is the ratio between μ and ρ, [4]

$$\nu = \frac{\mu}{\rho} \tag{1.6}$$

Using Eqs. 1.5 and 1.6, the Reynolds number can be expressed as

$$Re = \frac{U_\infty l}{\nu} \tag{1.7}$$

In a particular flow situation, there is a critical Reynolds number that distinguishes among flow regimes. For example, in a channel flow situation, the characteristic length is the half width of the channel; the flow becomes turbulent when $Re > 8000$.

The Mach number is the ratio of velocity of a fluid to the local velocity of sound in the medium,

$$M = \frac{U_\infty}{U_{sound}} \tag{1.8}$$

The velocity of sound in dry air (at sea-level pressure and 20 °C) is 343 m/s. Incompressible fluid model is assumed for flow analysis when $M < 0.3$.

Flows over geometrically similar bodies with the same Mach and Reynolds numbers are considered dynamically similar [5].

1.2.2 Turbulent boundary layer

In 1904 Ludwig Prandtl developed the concept of the boundary layer. It provides an important link between viscous and invisid fluids. He suggested that the viscous effect is confined in a thin layer near the wall. In a wall-bound channel flow, for example, the flow at the boundary has zero velocity relative to the boundary according to the non-slip boundary condition; the flow velocity increases with increasing distance

[4]For air at room temperature, ρ is $1.18 kg/m^3$ at 27 °C for air, [24], μ is 1.847×10^{-4} g/s cm (poise), or 1.847×10^{-5} kg/s m, and ν is $1.57 \times 10^{-5} m^2/s$.

[5]Two flows are defined as dynamically similar if (1) streamline patterns are similar; (2) velocity, temperature and pressure distribution throughout the flow field are similar when plotted against common non-dimensional coordinates; (3) the force (life, drag) coefficients are the same.

from the boundary (Fig. 1-5). This fluid layer which has a velocity shear is called the *boundary layer*. Some arbitrary point is used to designate the transverse position where the boundary layer ends. The thickness of the boundary layer, δ, is usually chosen as the vertical distance when the local flow velocity, u, is 99% of the mean flow velocity U_∞ [107]. The shear stress is proportional to the derivative of flow speed with respect to the vertical distance,

$$\tau = \mu \frac{du}{dy} \mid_y \tag{1.9}$$

The flow outside of a boundary layer is usually treated as invisid flow.

Understanding of wall-bound channel flows is important for our current studies. The characteristics and profiles of the boundary layer near the channel wall are described here. The boundary layer is laminar and also thin at the upstream end. As the flow travels down-stream, the continual action of shear stress tends to slow down additional fluid particles, causing the thickness of the boundary layer to increase with distance from the upstream point (Fig. 1-6). When the flow travels beyond a critical distance from the leading edge, small disturbances in the flow begin to be amplified. The flow becomes transitional and eventually a *turbulent boundary layer* is formed in which the fluid particles move in random paths. Near the wall, laminar motion is still retained; this layer is called a *laminar sub-layer*.

The transition from laminar to turbulent occurs typically when [48]

$$Re_x = \frac{U_\infty x_c}{\nu} \geq 5 \times 10^5 \tag{1.10}$$

with x_c being a critical stream-wise distance. On the other hand, x_c can be influenced by many factors such as surface roughness and stream-wise pressure gradient.

Within turbulent boundary layers there exist *coherent wall structures*, noticeably *quasi-deterministic vortices*. The higher-energy fluid elements from the outer region

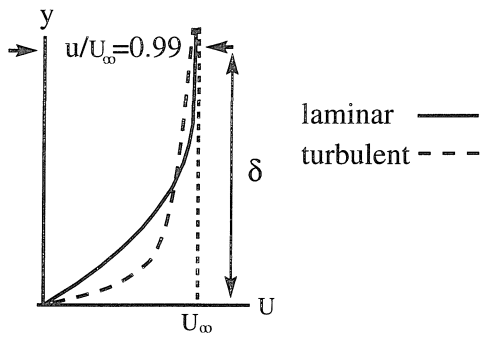

Figure 1-5: Schematic of velocity profiles for laminar and turbulent flows in the boundary layer.

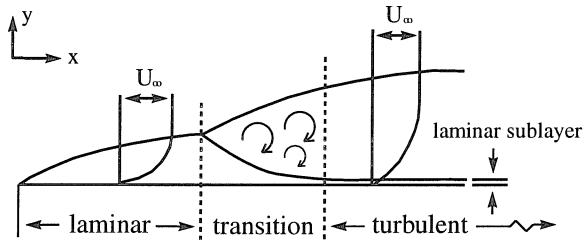

Figure 1-6: Evolution of wall-bound boundary layer in the stream-wise direction.

of the flow are pumped close to the surface. The laminar flow velocity profile is approximately parabolic in shape, while the turbulent flow velocity profile is more blunt. Hence, the average flow velocity gradient near a wall is larger for a turbulent flow in comparison with laminar flow (Fig. 1-5) [5]. Viscous friction is most effectively created within the turbulent boundary layer.

It can be proved that the pressure is a function of stream-wise location x only for a 2-D boundary layer, and it decreases with increasing x.

1.2.3 Quasi-deterministic wall structures

Flow turbulence is encountered in many situations and it is one of the most challenging problems of the fluid sciences due to its seemingly random nature. It has been discovered, however, that turbulence flow has dual features, deterministic and

random [62]. In the above-mentioned situation of a wall-bound channel flow, so called *quasi-deterministic* wall structures exist within the fully turbulent region; these structures are so-named because they have specific features and yet are not exactly identical.

Wall structures are responsible for most of the mass and momentum transfers. Many researchers study analytical modeling and experimental visualization of such vortices; the methods and results vary. However, it has been generally accepted that a quasi-deterministic wall structure is a pair of counter-rotating stream-wise vortices. In a typical life-time of a vortex pair, there is a sequence of four events: gradual outflow, lift-up, oscillation and breakup. Here, *lift-up* refers to the vortex pair being separated from the wall. Such a process has been successfully visualized [63].

The physical dimensions of near-wall structures are determined by the viscous scales of the channel flow [16]. In a channel flow, the length and time scales of associated wall structures are demonstrated within a range of flow velocity. The characteristic length scale l is 1.25 cm. The flow velocities (U_∞) are between $10 \sim 40 m/second$; within this range, the flow will be characterized as being turbulent.

First, a *wall friction velocity*, U_{tau}, is defined using the following formula

$$U_\tau / U_\infty = 0.1079 Re^{-0.089} \tag{1.11}$$

where Re is calculated based on the half channel width. As a result,

$$U_\tau = 48.3 \sim 170 cm/s \tag{1.12}$$

for the given flow velocity range. The *wall length scale*, y^+, is

$$y^+ = \nu / U_\tau = 31 \sim 8.8\mu\ m \tag{1.13}$$

Using Eq. 1.7, the length scale can also be written as a function of only U_∞

$$y^+ = \frac{\nu}{0.1079 U_\infty (\frac{U_\infty l}{\nu})^{-0.089}} \tag{1.14}$$

The averaged physical dimensions of the wall structures are as follows [16]:

$$length = 1000y^+ = 3.1 \times 10^4 \sim 8.8 \times 10^3 \mu\ m \tag{1.15}$$

$$width = 100y^+ = 3.1 \times 10^3 \sim 8.8 \times 10^2 \mu\ m \tag{1.16}$$

$$height = 10y^+ = 3.1 \times 10^2 \sim 8.8 \times 10\mu\ m \tag{1.17}$$

The *turbulent time scale*, t^*. is defined as

$$t^* = y^+/U_\tau = 64 \sim 5.2\mu s \tag{1.18}$$

The reported average life span of wall structures varies within a wide range as

$$life = 500t^* \sim 2500t^* \tag{1.19}$$

The length and time scales at selected velocities are summarized in Table 1.2. Also, according to Eq. 1.10, the critical distance for flow to become fully developed is

$$x_c = 0.78 \sim 0.196m \tag{1.20}$$

for the given range of flow speeds.

Flow velocity (m/s)	Reynolds Nunber	Y^+ (μm)	t* (μs)
10	8333	31	64
20	16667	16.5	18
30	25000	11.4	8.7
40	33333	8.8	5.1

Table 1.2: A summary of Reynolds number, length and time scale associated with a 2-dimensional channel flow, with the flow velocity between 10 – 40 m/s.

1.2.4 Flow separation and pressure drag

The shear stress within a boundary layer is related not only to the viscous drag, but also to the flow separation from a surface (usually a curved one). On a certain portion of an airfoil with an angle-of-attack, surface pressure may increase in the flow direction. As an example (Fig. 1-7), the pressure at stations S3, S2, and S1 are in a decreasing order. Such a trend of pressure with stream-wise distance is called an *adverse pressure gradient.* This gradient further reduces the motion of the flow near the surface along with friction forces in the boundary layer. If the adverse pressure gradient is sufficient, the flow near the wall will be stopped and the wall shear stress will reach zero at a certain stream-wise location (station S2 in this diagram). Beyond S2, the flow near the wall is reversed and the flow is said to have separated from the surface.

Because of the flow separation, the overall pressure distribution along the surface of a body will be different from the case when no separation happens. The net effect is to create a pressure distribution over the actual body surface which results in an integrated force against the flow direction, i.e. a pressure drag. For different shapes of bodies, the ratios of friction drag force and pressure drag vary within a wide range. It is noticeable that for common streamline bodies, the two drag components are almost equally divided; whereas for blunt objects, pressure drag dominate due to massive

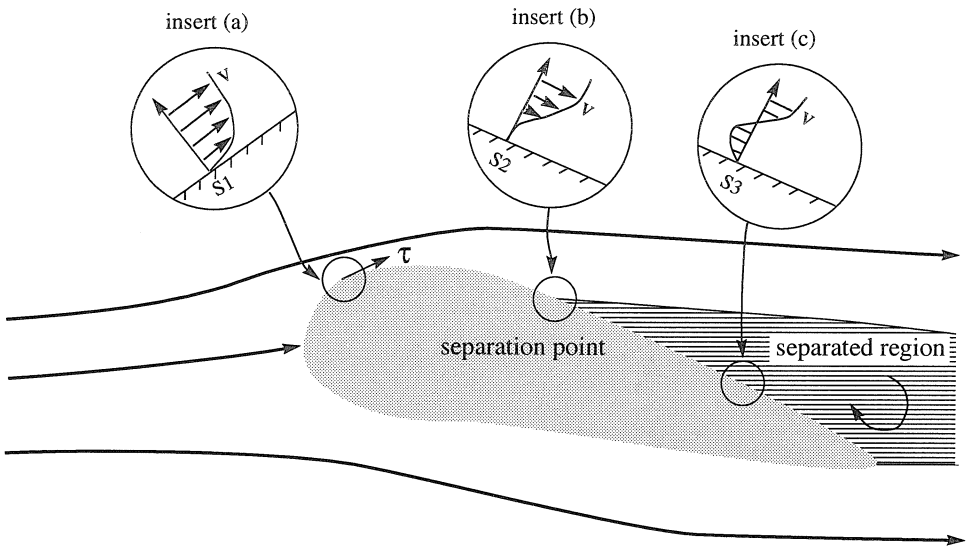

Figure 1-7: Effect of viscosity on a body in a moving fluid: local flow velocity profiles at different stream-wise locations and flow separation.

regions of flow separation.

1.3 MEMS for Fluid Mechanics - New Challenges

The interdisciplinary research of using micromachined devices in fluid mechanics and aerodynamics is a brand new effort. Each field creates opportunities and challenges to the other; as a result, new results in both fields can be discovered.

From the perspective of fluid mechanics studies, micromachined devices present new research directions in several ways. First, micromachining techniques improve the performance of conventional fluid measurement devices (in the current case, shear-stress sensors). Secondly, micromachined actuators can adequately influence the boundary-layer flow field to produce macro-scale fluid-mechanics effects. Micro actuators are interesting because they have smaller mass and higher response frequency compared with macro actuators. Thirdly, micromachining technology makes it possible to create large scale, distributed sensor or actuator arrays that are previously impossible be-

cause of technology and cost limitations associated with conventional manufacturing .

To satisfy the requirements of fluid mechanics applications using micro devices, new structures and operating principles must be realized. Two examples are demonstrated with our research. First, a new-type of thermal-isolation structure is proposed and realized, which results in improved shear-stress sensor performance. Secondly, actuators with relatively large areas, large displacements and forces must be used; therefore we have developed magnetic actuators using surface micromachining techniques and Permalloy electroplating.

1.4 Overview of Chapters

Chapter 2 discusses the concept, design, fabrication and testing (in still air and in a wind-tunnel) of a surface-micromachined shear-stress sensor based on thermal-transfer principle. The forced heat transfer, from a heated resistive element to the flow, is related to the boundary layer velocity profile, i.e., the shear stress. A unique vacuum sealed micro cavity, made possible using micromachining techniques, reduces the heat loss from the heated element to the substrate, thereby increasing the sensitivity drastically compared with conventional counter-parts. Sensors are operated in three modes: constant voltage (CV), constant current (CC) and constant temperature (CT). Sensor calibration in these three modes are conducted in a 2-dimensional wall-bound channel flow.

In **Chapter 3**, two types of micromachined magnetic flexural-type actuators are presented. The out-of-plane displacements of these sensors will interact with boundary-layer; these actuators must achieve displacements on the order of 1 mm and be able to sustain wind loading within the boundary layer. These requirements present unique challenges for MEMS.

In one actuator scheme, the displacement is produced as the result of interaction between magnetic dipole moment created by in-plane air-coils and an external magnetic field. Magnetic actuation in both up and down directions is achieved. However, this type of actuator suffers from intrinsic and thermal-stress bending which are un-desirable for its intended application. In the second actuator scheme, when an external magnetic field is applied, a piece of electroplated Permalloy ($Ni_{80}Fe_{20}$) material becomes magnetized and the Permalloy material's internal magnetic moment interacts with the external magnetic field to produce a bending moment to the actuator.

The concept, design, fabrication and testing of these magnetic actuators are presented in this chapter.

Chapters 4 introduces two micro-fabrication issues encountered in sensor and actuator development. Although micro-machined processes are largely derived from the IC fabrication, unique process requirements and challenges exist. As a simple example, deep etch (tens to hundreds of micrometers) is frequently encountered in micromachining while rarely of used for IC devices.

The goal of the first study is to find optimal combination of geometry and material factors that result in the most efficient sealing of micro cavities using LPCVD (Low Pressure Chemical Vapor Deposition) materials. This is currently a first systematically study on the sealing performance under the influence of geometry, sacrificial-material thickness, deposition material and thickness. Many previously-unknown sealing behaviors have been discovered.

Through the development of magnetic actuators, we discovered a unique method for drying surface micromachined cantilever-beam structures after their wet chemical etch/release. This technique is a unique augmentation to a growing family of anti-stiction methods for surface micromachined structures. It uses magnetic forces to overcome surface tension forces; micro structures are lifted during the drying process

to avoid contact and bonding with the wafer substrate. Simple equipment and chemical treatment are involved in the release and drying process. Special test structures are used to study the drying mechanism and evaluate its result.

Chapter 5 discusses current progress in two fluid mechanics applications. One application involves a distributed MEMS containing a large array of shear-stress sensors, magnetic micro actuators and neural network IC circuitry. The goal of the system is to actively reduce air-drag by detecting and controlling individual quasi-deterministic wall structures. Several fluid mechanical testings will be described; shear-stress sensors and micro actuators discussed in Chapters 3 and 4 have been proven effective in their intended fluid applications.

In another application, the purpose is to demonstrate the feasibility of using micromachined actuators to control a macro aerodynamic device. The control is performed by manipulating the boundary layer around the leading edges of a model delta-wing. Micro thermal shear-stress sensors are used to detect the flow separation line along the leading edges. The information on the flow-separation lines is used for positioning actuators for delta-wing controlling. Micro magnetic actuators are positioned along the delta-wing to influence the wall bound stream before natural separation occurs, in an effort to control the delta-wing rolling moment.

Convention In parts of Chapters 2 and 3 where micro fabrication process is described, frequently encountered steps are summarized in Appendix A. As a convention, the names of these important steps are underlined in the chapters.

Chapter 2

Thermal Shear-Stress Sensors

2.1 Introduction

The determination of wall shear stress, τ, is very important in fluid mechanics and aerodynamics studies. As an example, the overall viscous drag over an object in a flow field corresponds to the shear stress integrated over the surface area; the ability to map shear stress with a resolution comparable with the dimension of wall structures is critical for controlling these structures. In another example, high-resolution shear-stress measurements can also be used to pin-point flow separation locations.

2.1.1 Flow Shear-Stress Measurements

Shear stress measurement techniques can be categorized into indirect and direct methods [43, 35].

Direct measurement methods

Direct measurement relays on detection of the total amount of viscous drag on a surface-mounted force balance. The drag (F_d) on a surface with an area of S can be

obtained by integrating τ over the area,

$$F_d = \oint_S \tau \, ds. \tag{2.1}$$

This technique requires that a portion of the wall be movable in the direction of the flow; the force-balance plate must have a gap surrounding its perimeter. The presence of this gap, however, can introduce unwanted change in flow condition [26]; it is a major drawback for direct measurement techniques.

Indirect measurement methods

In indirect methods, τ is extracted from other measured physical parameters (e.g., pressure and wall temperature) that are indirectly related to the shear stress. For example, stream-wise pressure distribution inside a boundary layer can be related to τ and is the foundation of some well-established fluid mechanics calibration devices. Variations of Pitot tubes,[1] such as Preston tubes [94, 35] and Stanton tubes [49, 29], have been used for measurements of this nature. However, there are many disadvantages to these types of devices; the Preston and Stanton gauges both present obstruction to the flow and requires modifying the wall (e.g., drilling a hole).

Shear-stress measurements based on thermal transfer principles (hot-wire and hot-film sensors)[2] belong to the indirect method category and have been in wide use [43]. Compared with Pitot-tube measurement techniques, sensors based on thermal-transfer principles have the following advantages: they can be used in a wide variety of flow conditions, they present minimal disturbance to the flow itself because of the surface flush mount, and they offer the possibility of measuring time-varying flows.

[1] A flow pressure measurement device with one or multiple pressure-input ports. The device must extend into the flow region to measure local pressure; this device will therefore create disturbance to the flow field.

[2] Mass transfer (electrochemical) probes are similar to probes based on transfer of chemicals.

Micromachined shear-stress sensors

Traditional shear-stress sensors have serious disadvantages. The miniaturization of these sensors are difficult because their manufacturing typically requires delicate handicraft. For the same reason, mass-production with good device repeatability was very difficult to achieve. Micromachined sensors, on the other hand, are small in size and easy to produces in large quantities with precision. In recent years, both indirect and direct measurement techniques have been implemented using bulk and surface micromachining technology.

Micromachined surface floating-element balances for direct shear-stress measurements have been reported [101, 103]. The measured sensitivity was 52 μV(ac)/Pa in a gaseous-medium using a differential capacitor readout scheme, and 13.7 μV/V-kPa in a liquid medium using a piezoresistive readout scheme.

Traditional hand-made thermal-transfer based sensors suffer from two major drawbacks. First, because metal (e.g., nickel and platinum) is used as the heating and sensing element, the resistance of sensing element is low and a large biasing current is required to produce required surface-heating effects. Secondly, the sensitivity of such devices will be compromised because there is no effective heat insulation between the heated element and the substrate, due to fabrication and packaging difficulties. In recent years, however, micro shear-stress sensors have been demonstrated [127, 93, 110] using both bulk and surface micromachining technology. Micro sensors present device-performance improvement in two ways. First, the semi-conductor material employed as the heating/sensing element has a much higher resistivity compared to metal. Secondly, unique heat insulation features are are realized, only by using micromachining techniques, to solve the common but major problem that the heat loss to the substrate limits the performance of the conventional thermal shear-stress sensors. Such features include free-standing beams [79, 118, 34], free-standing diaphragms [126] and low thermal-conductivity layer such as polyimide [76, 106].

Overview of the current shear-stress sensor

In our fluid-mechanics applications, shear-stress sensors are required to have high sensitivity and to achieve real-time (frequency > 15 kHz) shear-stress measurement with fine spatial resolution (about 100 μm). In this chapter, we discuss our work on the development of a new, surface-micromachined thermal shear-stress sensor, with the fundamental design of a hot wire on a free-standing silicon nitride diaphragm. The novel aspect of the sensor is that the diaphragm lies on top of a vacuum cavity which minimizes the heat conduction from the diaphragm to the substrate through the gap; this feature offers much more effective thermal isolation to the substrate compared with the heat-insulation schemes previously discussed. The design, fabrication and testing of such a device is presented in this chapter. In Chapter 5, micro sensors application in two fluid mechanics applications are furthered explored.

2.1.2 Thermal Transfer Principle

The operation principle of the shear stress sensors is as follows: based on a fully developed turbulent flow condition, the rate of heat loss from a heated resistive element to the air-flow is dependent on the boundary-layer velocity profile, therefore the flow shear stress. The temperature change of the resistor is measured by the change in its resistance. Theories and analysis related to this sensing scheme are introduced in the following sections.

Resistance vs. temperature characteristics

The resistance, R, of a semiconductor sensing element at an elevated temperature T is expressed as

$$R = R_0(1 + \alpha(T - T_0)) \tag{2.2}$$

where R_0 is the resistance at room temperature T_0 and α is the temperature coefficient of resistance – TCR.

An important parameter governing the thermal shear-stress sensor operation is the *temperature over-heat ratio*, α_T, defined as the relative change of sensor temperature compared to the ambient temperature,

$$\alpha_T = (T - T_0)/T_0 \tag{2.3}$$

It is also practical to define a *resistance over-heat ratio*, α_R, as the relative change of sensor resistance compared to the resistance at the ambient temperature,

$$\alpha_R = (R - R_0)/R_0 \tag{2.4}$$

From Eqs. 2.2 and 2.4, the resistance over-heat ratio is related to the temperature over-heat ratio by

$$\alpha_R = \alpha T_0 \alpha_T \tag{2.5}$$

The *thermal resistance*, θ, is defined as a sensor element's temperature change $\triangle T$ due to an input power P; as in

$$\triangle T = T - T_0 \equiv \theta P \tag{2.6}$$

Plug this expression into Eq. 2.2, the sensor resistance can be written as

$$R = R_0(1 + \alpha\theta P) \tag{2.7}$$

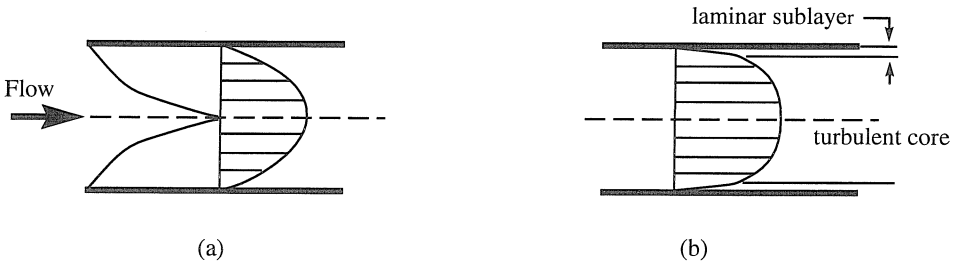

Figure 2-1: (a) Velocity and boundary-layer profiles for laminar flow region (up-stream) in a channel. (b) Profiles for a fully-developed turbulent flow region (down-stream).

Fully developed flow field

Consider a two-dimensional flow inside a channel with up-stream and down-stream portions of its stream-wise cross-section shown in Fig. 2-1. Boundary layers develop at the entrance on the top and bottom walls. As the boundary layer thickness grows with the flow travelling downstream, the boundary layers fill the whole channel at a certain down-stream position – the flow is termed *fully developed* beyond this point. If the flow is laminar, a parabolic velocity profile is experienced as is shown in Fig. 2-1a. When the flow is turbulent, a blunt profile is observed outside of the laminar sub-layers (Fig. 2-1b).

Thermal boundary layer

Just as the velocity boundary layer is defined as the region of the flow where velocity gradient is felt, a thermal boundary layer is characterized as a region where temperature gradients are present in the flow. Profiles for thermal and velocity boundary layers are illustrated in Fig. 2-2 for the case of a two-dimensional heat generating/sensing element (area = A_{eff}) inside of a two-dimensional channel flow. The resistor's long side is perpendicular to the direction of the mean flow. The relative velocity and temperature profiles are also shown in the diagram: within the thermal boundary layer, flow temperature decreases with the increasing distance away from

the heated element; outside of the thermal boundary layer, the flow temperature remains constant.

The relationship between the relative thickness of the velocity boundary layer and the thermal boundary layer is characterized by the *Prandtl number*,

$$Pr = \frac{\nu}{k_d} \tag{2.8}$$

where k_d is the thermal diffusivity defined by Eq. 2.16. At a downstream location x, the thermal boundary layer resides entirely within the velocity boundary layer when the Pr of larger than 0.7. This condition is true for most gases and liquids [48].

Because the flow velocity is zero at the wall, the heat transfer into the fluid takes place by conduction only. Under equilibrium conditions,

$$\frac{q}{A_{eff}} = -k_t \frac{d}{dy} T \mid_{y=0} \tag{2.9}$$

where q is the rate of heat transfer to the fluid, T is the temperature of the flow near the heated element, A_{eff} is the effective area of the heated element and k_t is the thermal conductivity of the air. The same amount of energy will be transferred by forced convection according to

$$\frac{q}{A_{eff}} = h(T - T_f) \tag{2.10}$$

where h is the heat convection coefficient and T_f is the temperature of the flow media. Therefore, by equalizing these two equations above, h can be related to the thermal conductivity at the wall by

$$h = \frac{-k_t \frac{d}{dy} T \mid_{y=0}}{T - T_f} \tag{2.11}$$

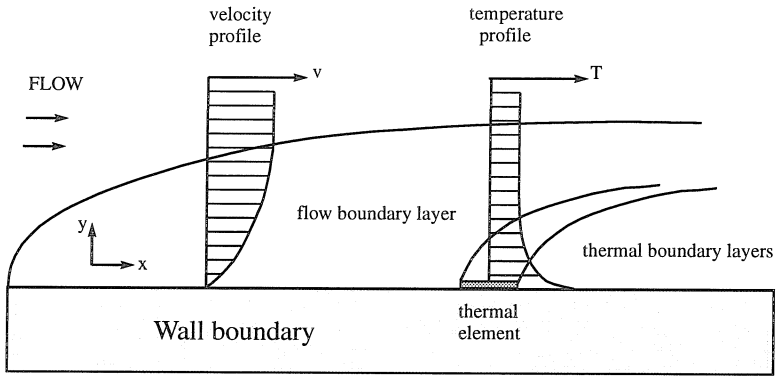

Figure 2-2: Schematic of velocity and thermal boundary layers.

Relation between shear stress and thermal transfer

To derive this relationship, it is commonly assumed that the velocity profile close to the wall is linear, therefore

$$U_y = y\frac{d}{dy}U_y \mid_{\ y=0} \tag{2.12}$$

where U_y is the flow velocity at a distance y from the wall. If $\frac{d}{dy}U_y$ at the wall is known, then the shear stress is simply

$$\tau = \mu\frac{d}{dy}U_y \tag{2.13}$$

The relationship between τ and the temperature difference between the heated resistor and the ambient is first solved by Mitchell and Harantty [84] under a major assumption that the thermal boundary layer over the element is thin enough that it lies within the velocity boundary layer. The following briefly demonstrate the procedure and major assumptions used in the calculation.

The complete thermal balance equation for a two-dimensional field is written as [35]

$$\frac{\partial}{\partial t}C + U_y\frac{\partial}{\partial x}C + V\frac{\partial}{\partial y}C = D(\frac{\partial^2}{\partial^2 x}C + \frac{\partial^2}{\partial^2 y}C + \frac{\partial^2}{\partial^2 z}C) \tag{2.14}$$

with

$$C = \rho C_f T \tag{2.15}$$

and

$$D = k_d = k_T / \rho C_f \tag{2.16}$$

Here, ρ is the density of air, C_f is the flow heat capacity, V is the flow velocity normal to the wall and $D = k_d$ is the *thermal diffusivity* of the flow media.

The following major conditions are also satisfied in a fully-developed channel flow in order to solve Eq. 2.14:

1. Thermal transfer in the span-wise direction is ignored;

2. Forced convection is strong so that diffusion in the stream-wise direction can be neglected;

3. Effects of natural convection is small compared to that of forced convection.

Under a pseudo-steady-state assumption, $\frac{\partial}{\partial t}C$ becomes negligible. Using assumption 3, the term $V\frac{\partial}{\partial y}C$ in Eq. 2.14 is taken as zero. In addition, under assumptions 1 and 2, $\frac{\partial^2}{\partial^2 y}C$ and $\frac{\partial^2}{\partial^2 z}C$ are ignored. As a result, Eq. 2.14 is re-written as

$$U_y \frac{\partial}{\partial x}C = D\frac{\partial^2}{\partial^2 y}C \tag{2.17}$$

Eq. 2.17 can be solved under the following boundary conditions

at $y = 0$, $T = T_w$ and

at large y and $x = 0$, $T = T_f$.

The solution for $T(x, y)$, obtained from solving Eq. 2.17 is used to calculate the av-

erage heat transfer rate, denoted q, from the resistor to the flow; finally we have

$$\frac{q}{\triangle T} = 0.807 \frac{{C_p}^{1/3} {k_T}^{1/3}}{L^{1/3} \mu^{1/3}} (\rho\tau)^{1/3} \tag{2.18}$$

where $\triangle T = T_{y=0} - T_f$ and L is the length (in the stream-wise direction) of the resistor.

Thermal heating power is related to the current input and the sensor resistance. Since part of the input power is transferred to the flow while the rest is lost through the substrate, the power balance is expressed as

$$i^2 R = \triangle T (A(\rho\tau_w)^{1/3} + B) \tag{2.19}$$

where $A = 0.807 A_e {C_p}^{1/3} {k_T}^{1/3} / L^{1/3} \mu^{1/3}$, and B determines the conduction heat loss to the substrate. At a certain input power $i^2 R$, the larger B is compared with ${A\tau_w}^{1/3}$, the smaller the shear stress sensitivity will be. Therefore, to design a successful shear-stress sensor, the heat loss to the substrate must be minimized.

2.2 Micro Thermal Shear-Stress Sensor

2.2.1 Sensor Design

Fig. 2-3 shows the schematic top and side views of a shear-stress sensor. The heating and heat-sensing element is a resistor made of phosphorous-doped polysilicon. The resistors are 50–200 μm long, 2 μm wide and 0.45 μm thick. Each resistor is located at the center of a cavity diaphragm. The diaphragm is typically 200×200 μm^2 in area, 1.5 μm in thickness and is separated from the bottom of the cavity by approximately 2 μm. The pressure inside the cavity is nominally lower than 300 mtorr, which is the pressure used in the LPCVD nitride sealing process. The resistors are uniformly doped

to a low sheet-resistance value of 50 $\Omega/\square$, with typical resistances between 1.25–5 kΩ at the room temperature for the range of resistor lengths. Two metallization wires, each 10 micro wide, connect the polysilicon resistor to the external electronics.

A number of sacrificial-material etch channels surround each cavity; these channels connect the oxide material inside the cavity to a etch holes. At the end of each etch channel, etch hole exposes the sacrificial material for access by the sacrificial-layer etchant. Etching starts at all etch hole openings at time zero and etch fronts gradually develop toward the center of the cavity. The sacrificial-layer etching fronts at two different time intervals (t_1 and t_2, with $t_2 > t_1$) are shown in Fig. 2-4; dark areas indicate remaining sacrificial material. In designing sensor geometry, it is important to arrange etch-channel locations so that the diaphragm free-etch can be done in a short time with a minimum number of etching channels; because the fewer etch-channel openings each sensor has, the easier it is for the cavity to be sealed.

During high-temperature deposition-seal process, the pressure inside the cavity is typically several hundred mtorr, much lower than the atmosphere pressure (760 torr). When the wafer is cooled to the room temperature after the CVD process, pressure inside each sealed-cavity is decreased.

Throughout the cavity diaphragm, the maximum bending occur at its center; the deflection magnitude can be estimated using the following equation [135],

$$bending = \frac{0.01516 \cdot ql^4(1-\upsilon^4)}{Et^3} \tag{2.20}$$

where l is the side length of the square-shaped cavity, υ is the Poisson's ratio of the diaphragm material, and q is the uniformly applied pressure (here being 1 atm = 760 torr = $1.01325 \times 10^5 N/m^2$). As an demonstration, let υ, t, l and E be 0.3, 1.5 μm, 200 μm and $160 \times 10^9 N/m^2$, respectively; a typical magnitude of deflection is 4.5 μm. We speculate the actual deflection is much smaller than this calculated value because of two reasons. First, the rigidity of the diaphragm is enhanced by the metallization

and the polysilicon resistor on top of the diaphragm. Secondly, diaphragm-clamping boundary conditions are changed due to the Bird's Beak geometry (to be introduced in the fabrication section). Further, the intrinsic tensile stress within the silicon nitride material will decrease the bending magnitude.

Designing the thickness of the diaphragm is a trade-off. For as the thickness of the diaphragm increases, thermal conduction to the substrate is enhanced due to the increased cross-sectional area of the diaphragm. On the other hand, if the diaphragm is too thin, the atmosphere pressure would make the diaphragm contact the substrate, increasing the heat conduction to the substrate.

The length of the resistive element will have an effect on the thermal conduction to the substrate. The longer the element is, the easier the heat transfer to the substrate will be. However, if the element is too short, the sensitivity will be reduced due to its reduced resistance value.

The size of each cavity will have a secondary effect on the heat transfer to the substrate. Obviously, as the size of the cavity becomes larger, the heat-transfer rate will be reduced due to the increase in conduction length. The thickness and width of the metal lines will also have a second-order effect on the heat transfer. If the cross-sectional areas of the line increase, more efficient heat conduction will take place between the resistive element and the substrate.

Studies have shown that a shear-stress sensor will be most sensitive when the mean flow velocity is perpendicular to its width dimension [83]. If the mean flow velocity is at an angle θ to the longitudinal direction of the sensing element, the sensitivity of the sensor will be proportional to $\sin\theta$.

Heat transfer modeling The dynamic performance of sensors can be characterized by using a structure with three composite layers. The resistor is the top layer, the silicon nitride diaphragm in the middle is the insulation layer, while the silicon substrate at the bottom is treated as a heat sink. Ohmic heat generated by the

resistor is conducted through the diaphragm and then into the substrate.

The heat conduction across the vacuum cavity is negligible. The thermal conductivity of the gas trapped within the sealed cavity is a function of pressure and temperature. Gas conductivity in the high-pressure regime is nearly independent of the pressure; while in low-pressure range, the mean-free-path becomes comparable with the dimension of the cavity and the thermal conductivity becomes strongly dependent on the pressure [27]. The conductivity of air at 1 atm (760 Torr) is about 1000 times larger than that of air at 200 mtorr.

A simple energy balance can be written as

$$i^2R = H_{cond} + H_{conv} = k_{nitiride}A_{eff}\frac{\triangle T}{\triangle d} + LA_{eff}{}' \triangle T \tag{2.21}$$

where H_{cond} and H_{conv} are the rate of heat loss by substrate conduction and airflow convection, respectively. $k_{nitride}$ is the thermal conductivity of the silicon nitride diaphragm, and A_{eff} is the effective area associated with the conduction heat loss. L is the convective coefficient, and $A_{eff}{}'$ is the surface area. Both A_{eff} are A'_{eff} are not exactly $w \times l$ but are modified by fringe factors. The heat transfer process can be modeled analytically or using electrical circuit analogy; cut-off frequency of the sensors can be deduced. Theoretical analysis and experiments both show that the time constant of a sensor with a cavity tends to be longer than if the cavity is replaced by substrate [53].

2.2.2 Sensor Fabrication

The micromachining fabrication process is discussed here. Fig. 4-17 shows the cross-sectional sketches of a shear-stress sensor at different process stages (1 through 8). Material deposition and removal on the backside of the wafers are neglected because they are not relevant to device fabrication and performance.

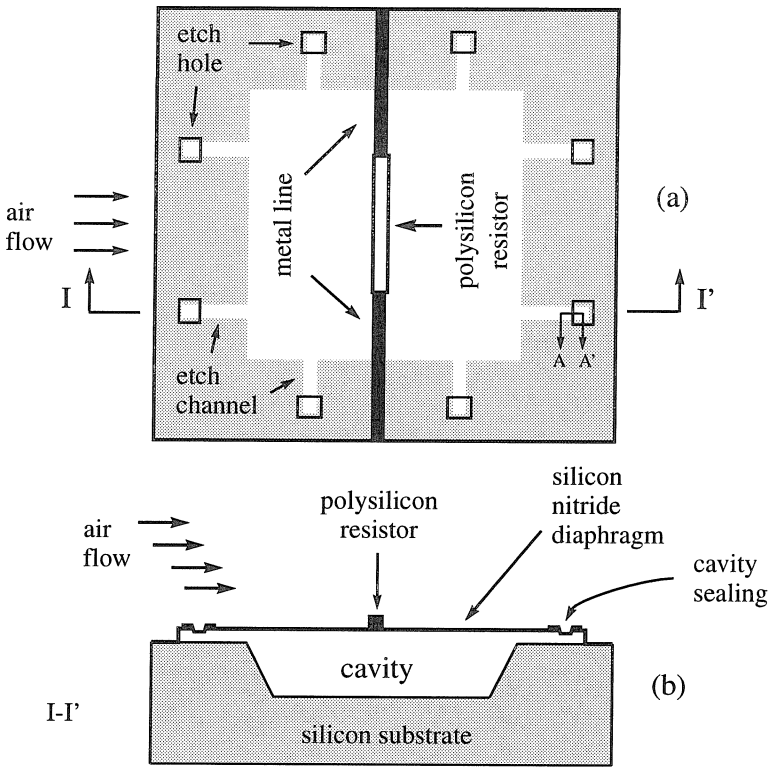

Figure 2-3: Schematic top and side views of a shear-stress sensor using thermal-transfer principles.

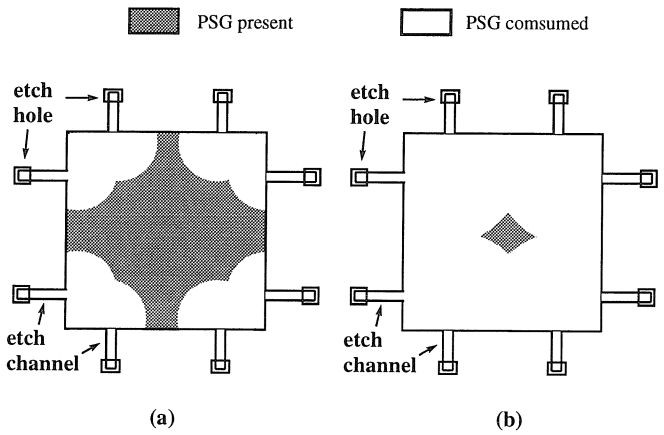

Figure 2-4: The profiles of sacrificial layer etching fronts at two different time intervals. The corresponding profile of the remaining sacrificial layer at (a) t_1 and (b) t_2 ($t_2 > t_1$).

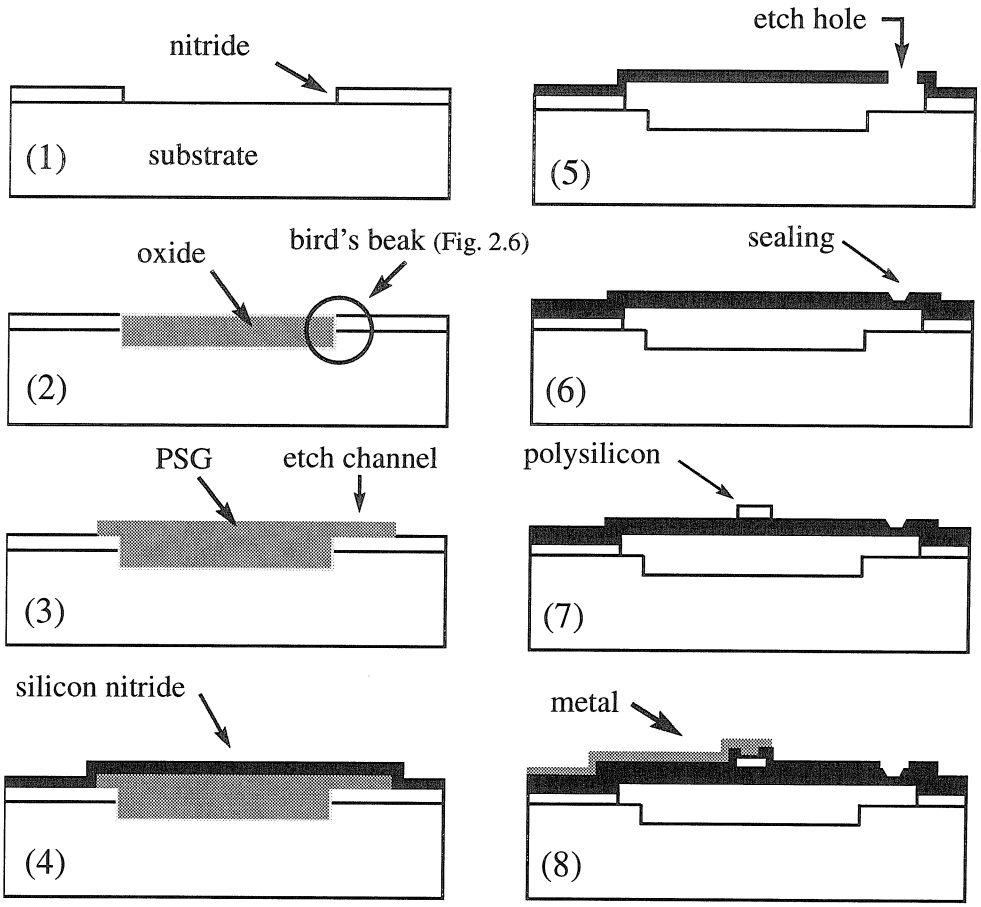

Figure 2-5: Fabrication steps of a shear stress sensor.

Stage 1

The starting wafer is a 4-inch-diameter, front-side polished silicon wafer that is 500 μm thick. First, a 0.4-μm LPCVD silicon nitride[3] layer is deposited on the wafer and photolithographically patterned to define the cavities (using KTI (viscosity=27 CS) photoresist). Each future cavity is defined as a 200×200 μm^2 square window. Silicon nitride material within the exposed window areas are etched away using SF6 plasma etching at approximately 700 Å per minute; the underlying silicon substrate is exposed in the windows. Since the plasma etch rate of silicon is approximately 1 μm per minute, to control the etch depth to within 10% of the expected depth is important for the next step – thermal oxidation. The photoresist layer is then removed using standard wafer cleaning procedures.

Stage 2

The ideal depth of each cavity, measured from the silicon nitride surface to the bottom of the silicon surface, is controlled to be close to 0.7 μm over the whole wafer area. If the resulting cavity depth after stage 1 is less than 0.7 μm, silicon is slowly etched to the correct depth by using HNA etchant (hydrofluoric acid: nitric acid: acetic acid = 1:3:8). HNA etches silicon at a slow rate of 0.5 μm per minute and therefore allows for easy timed-control of the cavity depth. HNA etch silicon nitride layer with a minimal rate.

This measure ensures that when a controlled thickness of silicon dioxide is selectively grown within the cavity areas, the final oxide surface will line up with the silicon nitride wafer surface exactly. This will minimize the surface roughness.

A 1.3 μm-thick silicon dioxide is grown using thermal oxidation at 1050°C in four hours. During the oxidation process, the silicon/silicon dioxide interface moves into

[3]see Appendix for fabrication details of underlined steps.

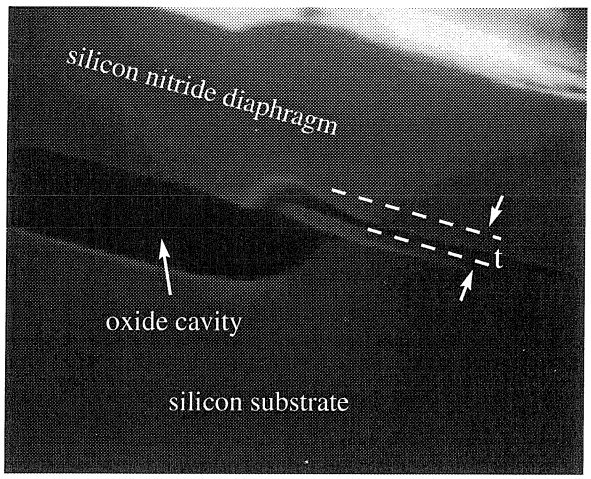

Figure 2-6: Birds's beak structure at the perimeter of the cavity.

the substrate. At the end of this oxidation process, 44% of the 1.3 μm oxide thickness will be contributed by oxidation below the original silicon surface [132].

At the boundaries of the cavity, lateral thermal oxidation will occur between the interface of silicon substrate and the first layer of silicon nitride, resulting in a so-called *bird's beak* structure (Fig. 2-6). A typical height of the bird's beak structure, denoted as t in the figure, is 300 – 400 nm. This lateral diffusion can be reduced using several schemes [108] however the current t will not cause major concern in fabrication and performance.

Stage 3

A 500 nm LPCVD sacrificial phosphosilicate glass (PSG) is then blanket deposited and the wafer is annealed in an annealing furnace at 950 °C for an hour. This step activates the dopant (P) and dopes the thermal oxide underneath the PSG layer to increase HF etch rate on the thermal oxide. The PSG layer is then patterned using photolithography (KTI (viscosity=100 CS) photoresist), to define the sacrificial layer and the etching channels overlying etch cavity. Unmasked PSG is etched away with buffered hydrofluoric acid within 20 seconds. The photoresist is then removed and the wafer is cleaned with Piranha.

Stage 4

A 1.2 μm-thick low-stress silicon nitride is then deposited as the diaphragm material. Etching holes are patterned in the silicon-nitride layer; the silicon nitride material within these holes are removed with SF6 plasma to expose the underlying sacrificial PSG. This plasma etch has a slow etch rate on the PSG layer and therefore 20% (time-wise) over-etch is done to ensure that all etch holes of the entire wafer area are clear.

Stage 5

In this stage, the sacrificial material is removed. Both sacrificial PSG and the thermal oxide is completely etched away using (49%) hydrofluoric acid in 20 minutes (Fig. 2-4). HF solution also etches silicon nitride, but at a very slow rate of approximately 40 Å /min.

After etching, the wafer is thoroughly rinsed in DI (de-ionized) water for 1 hour, to purge HF from within the empty cavity through out-diffusion. The water within cavities is then removed by spin drying the wafer at 7 krpm rotation speed; this is followed by convection-oven baking at 120 °C for an hour.

Stage 6

A second LPCVD silicon-nitride layer (400 nm thick) is deposited at approximately 300 mTorr (0.04 Pa) and 850 °Cto seal the cavities under vacuum [70]. Because there are still water molecules inside the cavities after the baking in stage 5, the deposition chamber is nitrogen purged at 600°C for 30 minutes before deposition starts; this step completely removes residue moisture before the high-vacuum nitride deposition begins.

The two deposition fronts meet to permanently seal the cavity; this is shown in Fig. 2-7. It also shows that the deposition thickness is different for different parts of

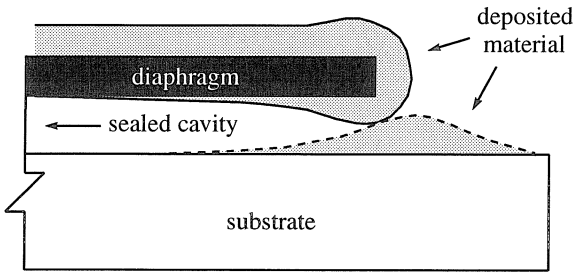

Figure 2-7: A close-up cross-sectional view at the etch hole opening (A-A' cross-section depicted in Fig. 2-3) of a sealed etching channel opening.

the sensor. On top of the diaphragm there is an average deposition thickness; near the entrance of the etch channel the deposition thickness is above average due to the increased space angle. Deposition thickness inside the etch channel and the cavity is dependant on the surface diffusion process and surface re-emission of particles (see 4.2.2); it is usually much less than the average thickness. Detailed studies of the sealing process can be found in Chapter 4.

The cavity diaphragm is now approximately 1.4 μm; it is equal to the original 1.2 μm silicon nitride (stage 4) and the 0.4 μm silicon nitride used for sealing, minus the silicon nitride thickness (approximately 2000 Å) consumed during the HF sacrificial etch.

Sealed cavities remain sealed for at least two years after they are formed.

Stage 7

To form the resistor, a 450 nm LPCVD polysilicon layer is deposited at 620°C . The polysilicon film deposited at this temperature is completely crystallized [57] with crystal grain sizes on the order of 600Å . Polysilicon doping is done by ion implantation with phosphorus using a total dose of $1 \times 10^{16}/\text{cm}^2$ at 40 keV of energy. The wafer is then annealed at 1000°C for 1 hour to activate the dopant and to reduce intrinsic stress in the as-deposited polysilicon material. The measured sheet resistivity of the polysilicon 50 $\Omega/\square$. The polysilicon is then patterned and plasma etched to form

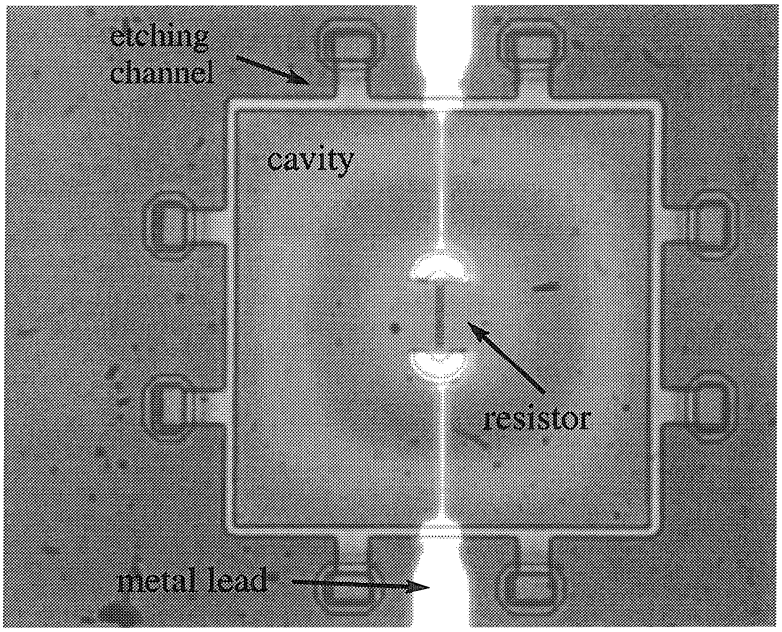

Figure 2-8: Optical micrograph of a shear-stress sensor with a sealed cavity.

individual resistors. After the photoresist removal, another 100 nm layer of LPCVD silicon nitride is deposited to passivate the polysilicon resistor. This film prevents resistance from long-term drifting due to spontaneous oxidation of the polysilicon resistor in air [100]. Contact holes are patterned and etched in plasma to allow for access to the polysilicon resistor through the last silicon nitride layer.

Stage 8

Finally, thermal evaporation produces the aluminum metallization (300 nm thick) which is patterned to form the leads. This thickness is found to be sufficient to ensure continuity of metal lines at the perimeter of the cavity.

Micrographs of the fabricated devices are shown in Fig. 2-8. The cavity is $200 \times 200\ \mu m^2$; the resistor is 40 μm long and 2 μm wide. Since the cavity is held under vacuum, the diaphragm is bent down by the external atmospheric pressure so that optical interference patterns (Newton Ring) can be seen under the microscope. Fig. 2-9 is a Scanning Electron Microscope graph of the polysilicon resistor.

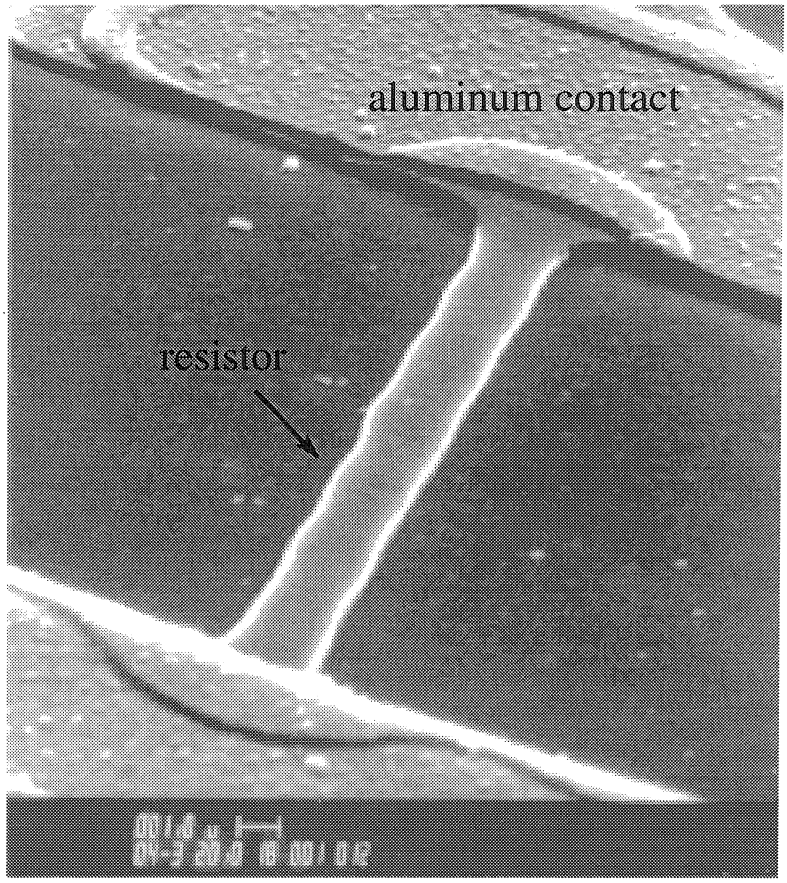

Figure 2-9: A Scanning Electron Micrograph of the polysilicon resistor.

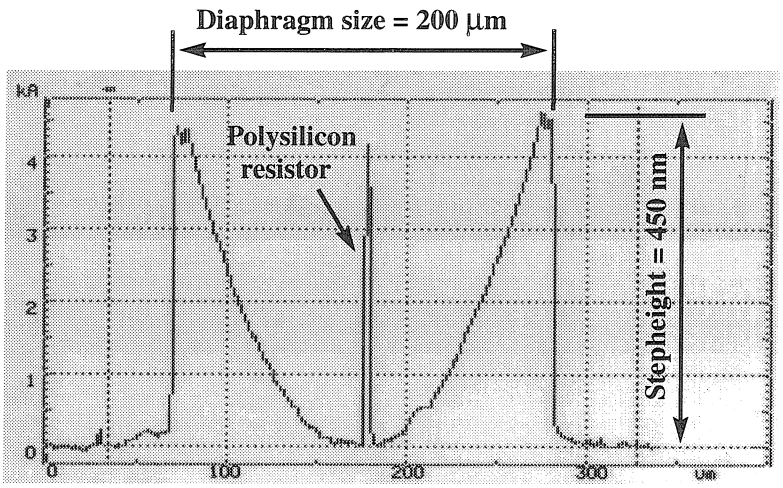

Figure 2-10: Surface roughness profile across the sensor diaphragm and through the resistor.

It is important that the top surface of the shear-stress sensors be smooth so that the surface roughness will not cause unwanted flow fluctuation [35]. Surface profiles of our sensors are examined using a surface profilometer (Tencor Instrument Alpha-Step 200) with a stylus force of 4 mg. Fig. 2-10 shows that, even under simultaneous loading of both the stylus and the atmosphere, the diaphragm has an over-all roughness of only 450 nm. This maximum step height corresponds to the t of the bird's beak plus the thickness of the top PSG layer deposited in step 3. It has been pointed out that surface roughness of less than $5y+$ should not change the flow analysis [123]. The current roughness is far less than 1 y^+ within our designed channel-flow velocity range; flow disturbance is negligible. In addition, this surface profile measurement also confirms that the diaphragm is not in contact with the cavity bottom under normal pressure conditions.

2.3 Sensor Testings

2.3.1 Wind-tunnel Setup

Shown in Fig. 2-11 is an experimental wind-tunnel (located at UCLA); its test section is 5 m long, 60 cm wide and 2.5 cm (h) high. The wind-tunnel has a maximum mean-stream velocity of 30 m/s. Since the width over height ratio of the test section is 60/2.5=24, flow is assumed to be two dimensional, i.e., flow pattern is independent of span-wise location.

The characteristic length used in the Re estimation is the half height, $h/2 = l =$ 1.25 cm. The associated Reynolds number Re, length scale Y^+ and time scale t^* of vortex wall structures at 10, 20 and 30 m/s are summarized in Table 1.2. For example, Re at 30 m/s is equal to 25000; at a flow speed of 9.6 m/s, Re will reach the critical value of 8000. The temperature of the flow inside the wind tunnel is also closely monitored though not close-loop controlled.

The sensor package is about 2×2 cm^2 in area and the sensor surface is mounted flush with the wind-tunnel side wall. The sensor package is located in the mid-span on the top wall of the wind tunnel, in a down-stream region where turbulence flow is fully developed (for the velocity range between 10-30 m/s). Fig. 2-12 shows the end portion of the wind-tunnel's test section where the sensor package is installed. Also shown in this figure are pressure taps along the side wall of the wind-tunnel. These taps are normally closed; they can be selectively accessed for stream-wise pressure measurement.

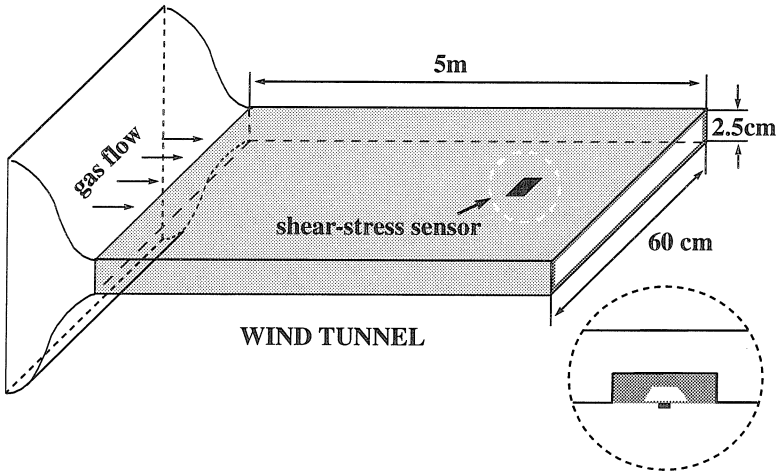

Figure 2-11: Location of the shear-stress sensor within a wind tunnel.

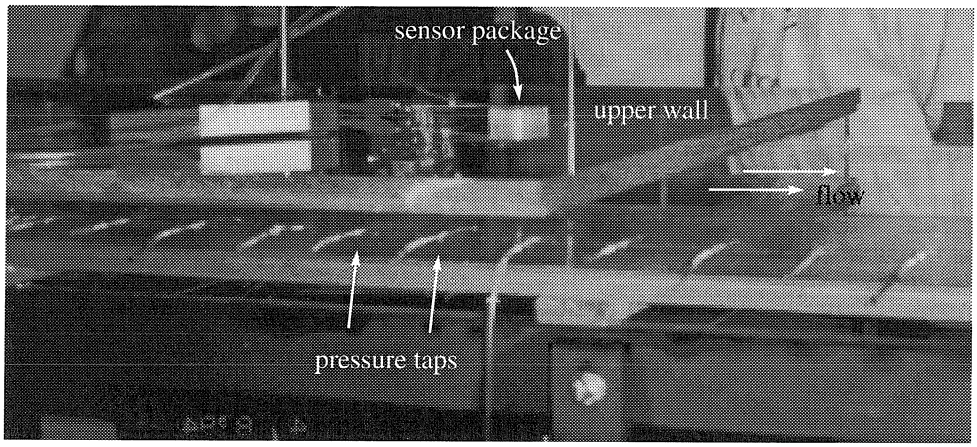

Figure 2-12: A picture showing the end portion of the wind-tunnel. The sensor package is located on the top wall, in the mid-span of the tunnel.

	Tungsten	Platinum	80% Platimum 20% iridium	Doped Polysilicon - Phossphorus
TCR ($^oC^{-1}$)	0.0045	0.0039	0.0008	0.0013
Resistivity (Ω·cm)	5.5×10^{-6}	10×10^{-6}	31×10^{-6}	2.2×10^{-3}
Thermal conductivity (W / cm K)	1.965	0.69	0.176	0.32 [ref:]

Table 2.1: Thermal properties of materials.

2.3.2 Thermal and Electrical Characteristics

Measurement: temperature coefficient of resistance

To measure the temperature coefficient of resistance (TCR) of resistors, we use a hot plate to heat up the sensor chip and measure the resistance at different temperatures. Here, the measured data of a typical resistor, phosphorus-doped, 100 μm long and 2 μm wide, is used as an example. The resistance vs. temperature relationship is plotted in Fig. 2-13. Enough time (20 minutes) is allowed between each temperature change to allow for thermal equilibrium. The slope of the linear curve represents the TCR (α) of the heated resistor (Eq. 2.2): 0.13%/°C . The TCR of some materials commonly used in thermal shear-stress sensors and anemometers are listed in Table. 2.1.

Doping the resistors with boron instead of phosphorus will yield higher TCRs; for example, TCR as high as - 6% has been demonstrated at a Boron doping level of approximately $10^{16} cm^{-3}$. However, boron-doped polysilicon resistors have severe non-linear resistance vs. temperature characteristics, which will create in-stability problems in common sensing-biasing circuit. Phosphorus-doped resistors show very linear relation which greatly simplifies the sensor-driving circuitry.

Thermal isolation

The thermal isolation characteristics of vacuum-sealed cavities of micro shear-stress sensors are evaluated by comparing I-V characteristics of sensors under three situa-

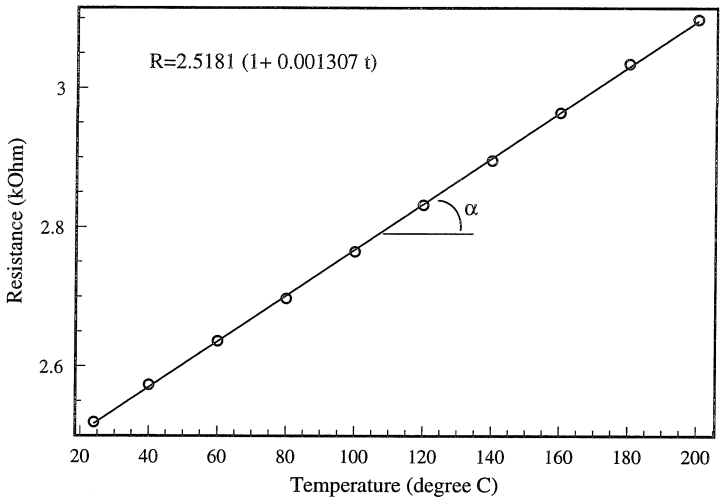

Figure 2-13: Temperature coefficient of resistance (TCR) of phosphorus-doped polysilicon resistors.

tions (Fig. 2-14). This is demonstrated using a sensor that is 50 μm long, 2 μm wide; the nominal resistance (according to measured resistivity) is1.25 kΩ.

In the first case, the resistor sits on top of a standard vacuum sealed cavity. In the second case, a crack is created in the diaphragm of the previous sensor with the help of a micro-manipulator probe; air therefore fills the cavity. In the last case, a replicate sensor element, identical with the first two resistors in geometry and resistance, is deposited directly on top of silicon substrate. I-V characteristic measurements in these cases are shown in Fig. 2-15 [4]. The first resistor (located on the vacuum cavity) has the largest I-V-curve non-linearity because its temperature effect is the most pronounced among all three; the I-V curve for the resistor directly over the silicon substrate is almost linear, indicating that the thermal conduction to the substrate dominates the heat transfer process and little temperature variation has been created.

Using data from Fig. 2-15, resistance (V/I) as a function of input power (V·I) is re-plotted in Fig. 2-16. Further, using the data from Fig. 2-16 and the resistor's known TCR, local temperature increases can be deduced; figure 2-17 shows the temperature

[4]Experiments are conducted in static room air

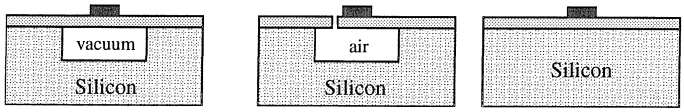

Figure 2-14: Sketch diagrams of (a) a polysilicon resistor located over a vacuum cavity and (b) on top of an air-filled cavity, (c) an identical resistor directly on top of the substrate.

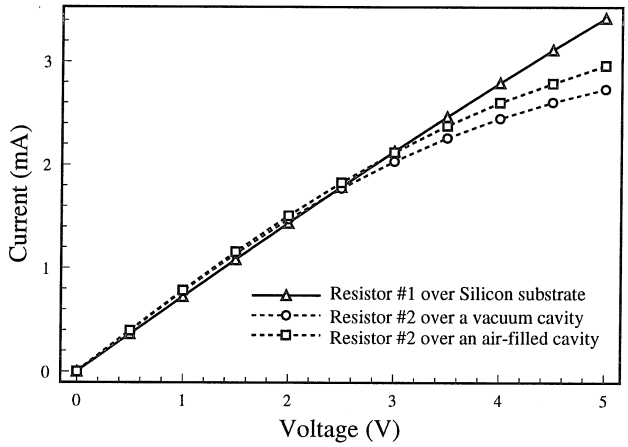

Figure 2-15: I-V characteristics of three resistors in Fig. 2-14.

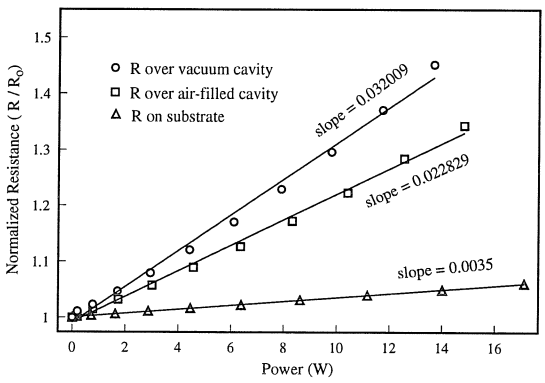

Figure 2-16: Calculated sensor resistance at various power inputs.

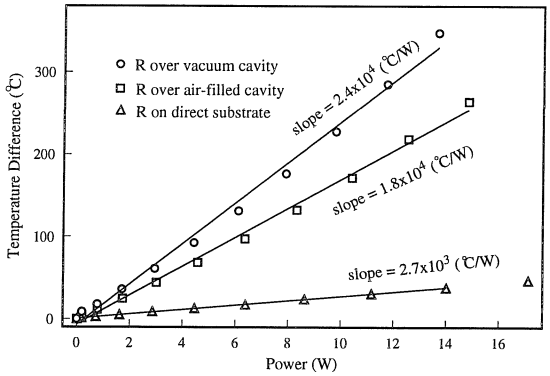

Figure 2-17: Resistor surface temperature (derived from the previous figure) at various power inputs.

variation as a function of the power input. According to Eq. 2.7, the slope of these three curves indicate the thermal resistivity θ. It is found that θ is 2.4×10^4°C/W for case 1 (resistor on a vacuum cavity), 1.8×10^4°C /W for case 2 (resistor over an air-filled cavity) and 2.7×10^3°C/W for the last case (resistor directly on the substrate). It is clear that the vacuum cavity improves the thermal isolation: θ for case 1 is 1.33 times that for case 2, and 9 times that for case 3. Exact values of thermal resistance as well as ratios of θ among three cases depend on sizes of the cavity diaphragms and the geometry resistors.

Biasing of sensors

In determining the biasing power to the sensors, there is a maximum power consumption. Above this limit, either the diaphragm will fracture due to thermal heating or the resistor/metal interconnect will experience an electrical breakdown. In our experiments, the bias for the resistors is always set below 15 mW to ensure long-term reliable operations.

Further more, the resistance over-heat ratio, α_R, is set to be less than 0.5. This measure prevents the temperature of the sensor to become so high that natural heat-convection will influence the flow field. The α_R is also set to be lower than 0.25

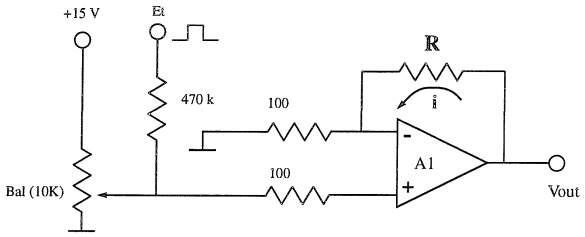

Figure 2-18: Constant-current mode driving circuit.

(corresponding to a maximum sensor temperature of approximately 250°C) so that re-crystallization of polysilicon will not occur during operation.

Since the resistance of a micromachined hot-film sensor ($> 1k\Omega$) is generally higher than the value of a traditional hot-wire sensor (approximately 50 Ω), conventional driving circuits for anemometers need to be modified for present use. Three different types of circuits have been developed for our experiments [52]: constant current (CC), constant voltage (CV) and constant temperature (CT). The CV circuit has a simplest configuration and the CT circuit is the most complex. The CT circuit also provides the fastest time response among all three.

In both CC and CT circuits, terminal Et is where pulsed signal is fed into the circuits for time-constant measurements. The constant-current circuit is shown in Fig. 2-18, in which R represents the sensor resistor and E_{out} is the output terminal. The CT circuit (Fig. 2-19) contains a feedback loop that keeps the voltage across the sensor resistor R constant. Resistors R4, R6, R and Ra form a bridge. Before a circuit is used to drive a sensor, selecting an over-heat ratio and balancing the bridge are crucial. When the switch S1 is connected to the calibration terminals, the combination of R16 and R11 determines the overheat ratio. For example, when R16 is 27 kΩ and R11 is 220 kΩ, the overheat ratio is 0.1. The Ra resistor is first adjusted so that the output voltage is at a desired value. After calibration, S1 is switched back to the terminals for normal operation. More details about the operation of the CT circuit can be found in [10]

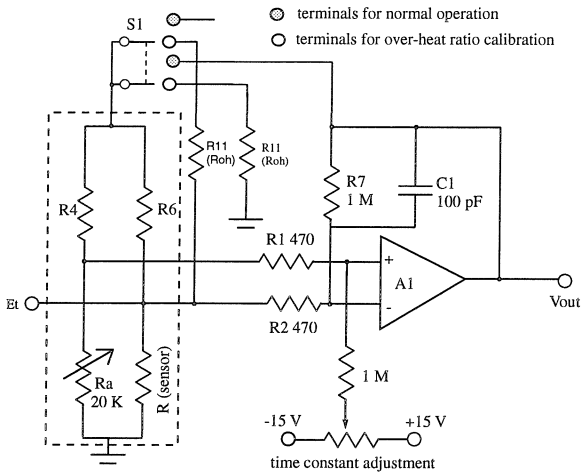

Figure 2-19: Constant-temperature mode driving circuits.

Ambient temperature and pressure sensitivity

The resistance of the sensor element is dependant on the ambient flow temperature and the pressure. Since the temperature of the test wind-tunnel is monitored but not controlled in a closed-loop manner, a reference sensor is used to monitor the temperature alone. The reference resistor thus sits directly on top of the silicon substrate and provides information on the ambient temperature of the flow.

Pressure variations will cause the diaphragm to change its profile and therefore induce piezoresistive effects in the sensing element. The fluid-mechanics aspects of pressure variation is beyond the scope of current studies. However, from the simulation data provided in [75], a typical 1 psi pressure variation will create a voltage shift of approximately 0.25 mV for a sensor biased by a 2.5 V DC voltage. This drift voltage is small compared with the signal produced by shear-stress variation (refer to Fig. 2-20).

Time response

Time constants of sensors are analyzed using equivalent circuit models and also measured experimentally. Experimentally, since suitable velocity fluctuations are not

readily available, one usually relies on electronic test signals. According to both theoretical analysis [42] and experimental confirmation [85], the frequency response or time constant can be obtained by feeding an electronic sine wave or square wave into the E_t terminal of both CC and CT circuits. Most commonly, when a step current (square wave) passes through the resistor, the transient voltage response is used to deduce the time constant.

We compare the effect of the vacuum cavity on the time constant of a shear-stress sensor; the reference resistor is identical to the sensor resistor but located directly on the substrate. The square-wave responses of the sensor and the reference resistor are measured under an over-heat ratio of 5.5%. Using CC mode, the frequency response of the sensor (with cavity) is several hundred Hz (time constant is on the order of 1 ms). Using CT circuitry with feed-back control, the time constant is decreased and the frequency response increased drastically. The measured time constants are 72 μs and 5.2 μs for the former and the latter, respectively. These time constants are consistent with the results indicated by theoretical models [53]. According to the approximate relation between time constant t_c and cut-off frequency f_c for CT operation, $f_c = 1/(1.5t_c)$; the cut-off frequency is estimated as 9 kHz and 128 kHz for the sensor and the reference resistor.

2.3.3 Sensor Calibration

Wind-tunnel calibration of the micromachined shear-stress sensors is conducted under CC, CV and CT driving modes. The steady-state sensor voltage output (time averaged over a two-minute period) with respect to the mean-stream velocity is measured at various flow velocities ranging between 5 to 25 m/s.

In order to correlate the output voltage with the wall shear stress (τ_w), two methods [55] are used here. In the first method, τ_w in a fully developed channel flow is

related to the stream-wise pressure gradient by

$$\frac{dP_x}{dx} = -\frac{\tau_w}{h} \tag{2.22}$$

where P_x is the local pressure, x is the stream-wise coordinate, and h is the half height of the wind tunnel. In the second method, an empirical relationship between the Reynolds number and the wall shear stress in a fully developed channel flow is obtained, by using

$$\frac{u_\tau}{u_\infty} = 0.1079 Re^{-0.089} \tag{2.23}$$

and

$$\tau_w = {u_\tau}^2 \rho, \tag{2.24}$$

The τ_w given by Eq. 2.22 is precise but the pressure measurements are not always experimentally available; on the other hand, Eqs. 2.23 and 2.24 link shear-stress directly with flow velocity measurement. We first measure the stream-wise pressure gradient with the help of pressure taps along the side wall of the wind-tunnel. τ_w is calculated by using Eq. 2.22. Afterwards, we use the second method given by Eqs. 2.23 and 2.24 to calculate the wall shear stress again. Good agreement is found between shear-stress values calculated by using both methods. For example, at free stream velocities of 9.96 m/s, 14 m/s, and 20 m/s, the first method gives τ_w's of 0.2388 Pa, 0.5384 Pa and 0.945 Pa, while the second method gives τ_w's of 0.2813Pa, 0.5232 Pa, and 1.029 Pa. This agreement gives us confidence in directly estimating τ_w from the mean stream velocity.

The calibration results for one sensor unit ($R_0 \approx 2$ kΩ) at the same resistive over-heat ratio α_r of 0.2 but different operation modes are shown in Fig. 2-20. The top curve, for CT mode operation, has a higher sensitivity compared with that of the CC and CV mode operation. Data in Fig. 2-20, with the heating power $P = i^2 R$ divided by the temperature different $\triangle T$, is re-plotted as a function of the shear stress to the

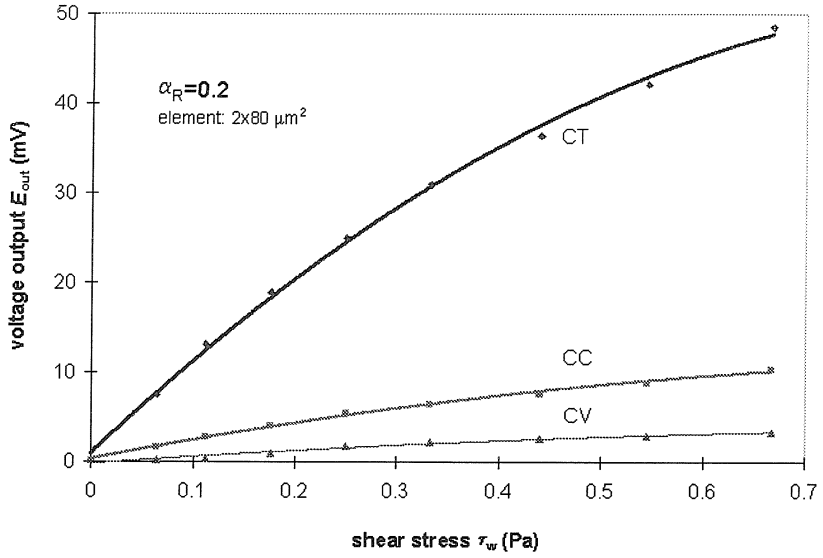

Figure 2-20: Output voltage vs. wall shear stress for CC, CV and CT operation modes.

mode	A $\rho^{1/3}$	B
constant voltage	0.0755	42.7432
constant current	0.10015	42.7409
constant temperature	0.5698	42.593

Table 2.2: Fitting parameters for sensor output using CV, CC and CT modes.

one thirds power - a linear relation is exhibited. According to Eq. 2.19, the slope of the curve corresponds to A and the intercept on the $P/\triangle T$ axis is B. The fitting parameters for the three modes are summarized in table 2.2.

2.3.4 System Implementation

The shear-stress sensors have been used in an active fluid drag control project for real-time detection of surface vortex structures. Also the sensors have been mounted on a rolling-rod located at the leading edge of a model delta-wing; the RMS signal output is used to determine the flow separation point at various positions along the

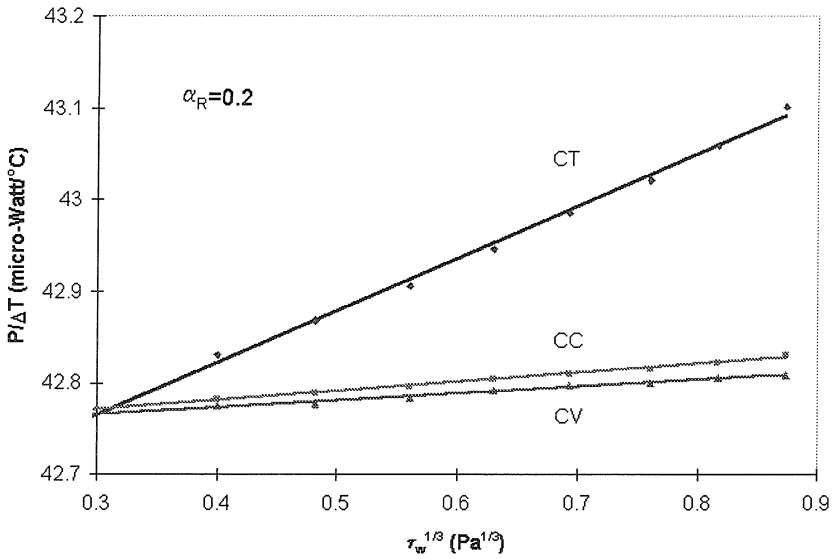

Figure 2-21: The ratio between input power and temperature variation versus the shear stress$^{1/3}$.

leading edges. More details on these fluid applicatios are in Chapter 5.

2.4 Summary

A micro-machined boundary-layer shear-stress sensor has been developed. The sensors operate on thermal-transfer principles; they are fabricated using surface micro-machining techniques. The heat generating and sensing element, a poly-crystalline silicon resistor, is located on top of a vacuum-sealed cavity; the heat loss from the resistor to the substrate is therefore reduced tremendously. Shear-stress calibration within a wind-tunnel, using three different driving modes- CC, CV and CT. The response curves agrees with theoretical analysis well. CT mode operations show the highest shear-stress sensitivity and the fastest frequency response. Applications of these sensors in fluid-mechanics applications will be demonstrated in Chapter 5.

Chapter 3

MICRO-MACHINED MAGNETIC ACTUATORS

3.1 Introduction

We intend to make micromachined actuators that can achieve large out-of-plane movement to perturb boundary-layer flow in a controllable manner. Since the actuators' rest position must be within the wafer surface plane to minimize unwanted flow disturbance, we have designed flexure-type actuators. An actuator consists of a plate supported by either cantilever or torsional beams; the plate is the main unit that generates magnetic forces and produces flow disturbance.

For our intended fluidic applications, the actuators must be able to meet the following requirements. First of all, to achieve effective flow control in a channel flow with the turbulent boundary layer being 30^+ thick (section 2.2), actuators must be able to gain vertical displacement of up to 1–2 mm (in a velocity range of 10–30 m/s). Secondly, within a designed flow velocity of 10–30 m/s, for example, the static wind load on a 1×1 mm^2 size actuator is in the range of 59 to 530 μN (estimated using Eq. 3.12). It is worth noting that the fluctuating part of the wind loading can be up to 100% of the DC wind load; it is capable of inducing strong vibration. Thirdly,

when these actuators are used for controlling wall structures discussed in Chapter 1, the mechanical resonant frequency should be , preferably above 1 kHz.

To design and fabricate micro machined actuators that suit the above-mentioned requirements is a challenging task for micromachining. In the next three sections we will show why electrostatic driving mechanism, a commonly used technique, does not fit the current requirements and magnetic actuation will provide large force and displacement.

3.1.1 Electrostatic Actuation

Until now, the most widely used driving mechanism for micromachined actuators were based on electrostatic forces [115, 8]. The basic operating principle is demonstrated using the following example of two conducting parallel plates separated by an insulating layer.

The two plates shown in Fig. 3-1 form a capacitor with a capacitance given by

$$C = \epsilon_0 \epsilon_s w \frac{l}{d} \tag{3.1}$$

where w and l are the width and length of the plates and d is the spacing between them. ϵ_0 and ϵ_s are the free-space and relative permeability. If a voltage V is applied across the two plates, the potential energy storage within this capacitor is

$$U = -\frac{1}{2}CV^2 = -\frac{\epsilon_0 \epsilon_s w l V^2}{2d} \tag{3.2}$$

The forces in x, y and z directions are given as the negative partial derivative of U in each direction.

$$F_x = -\frac{\partial}{\partial x}U = \frac{1}{2}\frac{\epsilon_0 \epsilon_s l V^2}{d} \tag{3.3}$$

$$F_y = -\frac{\partial}{\partial y}U = \frac{1}{2}\frac{\epsilon_0 \epsilon_s w V^2}{d} \tag{3.4}$$

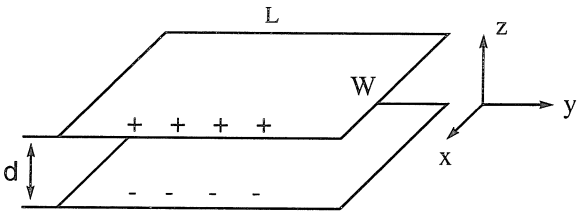

Figure 3-1: Electrostatic force between two capacitor plates.

$$F_z = -\frac{\partial}{\partial z}U = -\frac{1}{2}\frac{\epsilon_0 \epsilon_s w l V^2}{d^2} \tag{3.5}$$

Electrostatic driving suffers from two major disadvantages. First, large out-of-plane deflection is difficult to achieve because of the limited range of forces. The force and movement in the x and y directions are in-plane. Actuation in the z direction is typically a few micrometers perpendicular to the substrate plane because the magnitude of F_z decreases with a rate inversely proportional to that of increasing d^2 [1]. Secondly, only attractive forces are possible.

3.1.2 Magnetic Actuation vs. Electrostatic Actuation

Comparison of electrostatic driving and magnetic driving has several issues of focus [12, 8]: stored energy density, efficiency, compatibility with on-chip IC circuitry and, last but not least, functionality.

First of all, the order-of-magnitude of the stored energy densities for these two driving methods [2] are largely compatible at the micrometer scale. Secondly, in terms of efficiency, magnetic actuation is current-switching based while electrostatic driving is voltage switching based; when the frequency of the electric signal is low, the electrostatic actuator virtually consumes no power at all while the magnetic actuator must maintain a constant current flow (on the order of 10 mA) and power consumption.

[1] Bias voltage is typically tens or hundreds of volts

[2] Magnetic energy is proportional to $\mu_0 V_m M^2$ where V_m is the volume of the magnetic material and M is the magnetization.

Eddy current and hysteresis losses involved with magnetic actuation also contribute to potential energy loss. However, in cases where mechanical loss (e.g., friction) must be considered, it becomes predominant over other forms of loss previously mentioned and its effect on reducing the efficiencies in both driving methods are similar.

The electrostatic driving mechanisms are easily integratable with microelectronics circuits due to the surface micromachining technology. In recent years, thin film magnetic materials which have been pioneered in the magnetic recording-head industry are becoming more and more widely adopted into the micromachining field [18]. Electroplated soft magnetic materials, as one of the examples, has been used to make coil-wrapped electromagnets in several types of devices, including micro valves [11], micro electromagnets [17], magnetic micro motors [40] and micro inductor [3].

Therefore, as far as energy density, efficiency and IC compatibility are concerned, there is no blanket conclusion that favors one form of actuation over another. The functionality of each specific application must be taken into consideration.

When large out-of-plane displacement and large force actuators are required, magnetic actuation is a capable candidate while electrostatic actuation is not [12]. Several types of magnetic micro-actuators have been previously demonstrated. Wagner et. al. [128] performed post-processing manual attachments of permanent magnet pieces on micromachined plates and actuated the magnet with an external magnetic field generated by in-plane coils. The manual assembly is unsuitable for us because a large number of actuators are required. However, these flaps require a large current ($\sim$50 mA) to operate and have considerable actuator heating problems. Judy *et. al.*, on the other hand, demonstrated the in-plane motion of a suspended polysilicon structure with an electroplated Permalloy plate [60]. The plate was driven by an external magnetic field to a large deflection angle (over 180°), under an estimated torque of over 0.185 nNm. A micro mirror with torsional magnetic actuators has also be realized by Judy *et. al.* [61].

3.1.3 Overview of Current Magnetic Actuators

We have developed two different types of magnetic actuators. These actuators are both flexural types; they typically consist of a plate and support beams. The plate is responsible for generating magnetic force/torque and interacting with the flow field. The supports are either cantilever beams or torsion bars; these are made of silicon nitride or polysilicon material. The concept, design, fabrication and testings of both actuators are presented in this chapter.

The first type of actuator is discussed in section 3.2.1. Micro coils overlying the plate carries a biasing current, and produce a magnetic dipole moment. The moment interacts with an externally applied magnetic field to create a torque that causes the plate to move.

The second type of actuator is introduced in section 3.2.2. A piece of soft magnetic material, instead of coils, covers the plate. Inside an external magnetic field, the magnetic piece will be magnetized, and the internal magnetization interacts with the external field and creates plate movement. The operating principle has also been used by other researchers. Similar magnetic devices have been reported by Judy *el. al.* [60, 61]; however, our current devices are required to withstand larger flow loading forces.

3.2 Air-coil Magnetic Actuators

3.2.1 Actuator Design

Figure 3-2 shows the perspective and cross-sectional views of an air-coil magnetic actuator, which consists of a magnetic coil located on top of a square plate supported by two cantilever beams on its side. The biasing current path is from *bonding pad 1* to *contact 1*, through the polysilicon plate to *contact 2* and finally through the coil

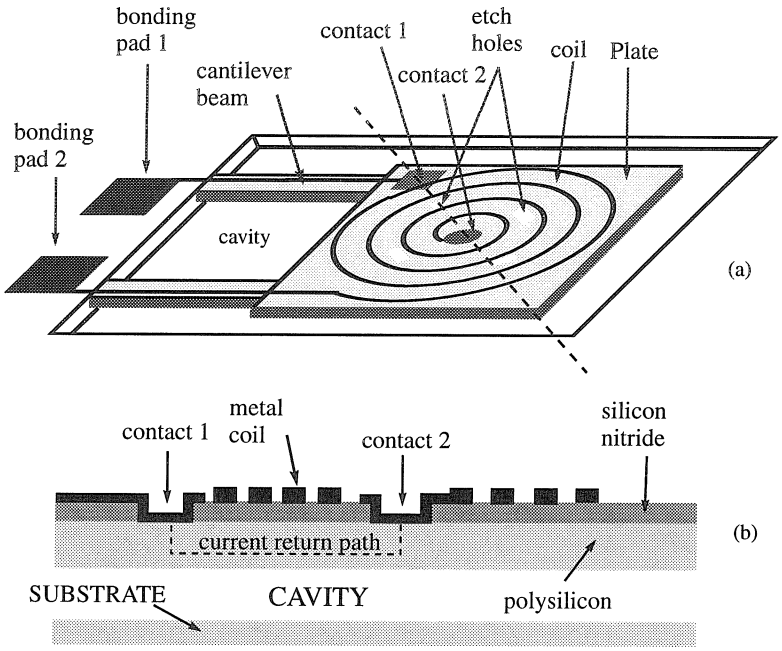

Figure 3-2: Perspective and cross-sectional views of the air-coil magnetic actuator. (a) Perspective view; (b) cross-sectional view of the plate cut across the dotted line in (a) showing the structural layers: polysilicon, silicon nitride and metal layers. Polysilicon forms the return path for the current loop.

to *bonding pad 2*.

There are several facets to the design issues: magnetic (magnetic torque), mechanical (support strength and intrinsic stress), fluidic (flow loading), thermal (thermal bending) and electrical (current-loop resistance and ohmic heating). These will be analyzed in the following sections.

Magnetic torque

A group of N current loops is placed within a magnetic field with a flux density $\bar{B}$. Each loop has a radius of $r_{j,j=1..N}$ and an enclosed surface area of $\bar{A}_{j,j=1..N}$, with

$$\mid A_j \mid = \pi {r_j}^2 \tag{3.6}$$

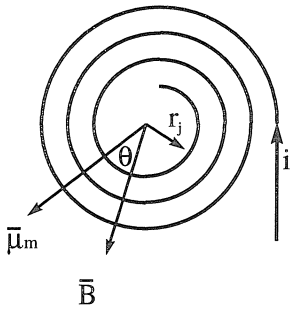

Figure 3-3: Sketch diagram of a current-carrying coils in a magnetic field, B.

Each coil carries a current i and produces a magnetic dipole moment given by

$$\bar{\mu_{mj}} = i\bar{A}_j \tag{3.7}$$

This dipole moment interacts with $\bar{B}$ to produce a magnetic torque [15]

$$\bar{\tau}_j = \mid \mu_m \mid\mid B \mid \sin\theta \tag{3.8}$$

Since the directions of all $\bar{A}_j$ are identical, the overall torque that these N coils experience is

$$\bar{\tau} = \sum_j^N \bar{\tau}_j = i \sum_j^N \mid \bar{A}_j \mid\mid B \mid \sin\theta \tag{3.9}$$

Fluid loading

In a free-stream flow field with an mean velocity of U_∞, a *dynamic pressure*, P_∞ is defined as

$$P_\infty = \frac{1}{2}\rho U_\infty^2 \tag{3.10}$$

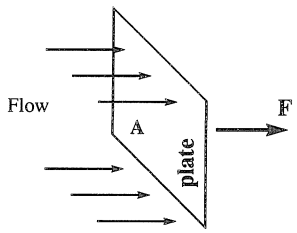

Figure 3-4: Flow loading on a plate with area A.

Let S be a reference area, [3] then a dimension-less drag coefficient C_D is defined as

$$C_D = \frac{D}{P_\infty S} \tag{3.11}$$

where D is the total drag force. As an example, in the case of a flat plate with an area $A \equiv S$ in a laminar flow field perpendicular to the area (Fig. 3-4), C_D is known to be 2.0 [5]. The total drag force is therefore $\rho U_\infty^2 A$. However, when the plate is completely inside a boundary layer, the over-all drag force is expected to be below this estimated value due to the somewhat reduced velocity. Overall, the following equation

$$F = P_\infty A = \frac{1}{2}\rho U_\infty^2 A \tag{3.12}$$

is a good estimate for the order-of-magnitude of the drag force. As an example, when $A = 1 \times 1$ mm^2 and U_∞= 10 m/s, the force is about 59 μN; at a velocity of 30 m/s, the loading force is 530 μN.

Support strength

The force constant of the flap can be obtained by using an approximate composite-layer model [135] or by a more precise finite element simulation.

The plate and the cantilever beams are composed of three layers of materials: LPCVD polysilicon, LPCVD silicon nitride and metallization (a gold layer and a

[3] S is chosen to pertain to a given geometric body shape. For a wing, it is the plane-form area; for a sphere, the cross-section area.

very thin chromium layer). A multi-layered beam can be reduced to a single-layered beam by combining two layers at a time to obtain an equivalent flexural rigidity EI. As shown in Fig. 3-5, we first combine poly-crystalline silicon (with E_1 and I_1) and metallization (with E_2 and I_2). The equivalent flexural rigidity EI is

$$EI = \frac{w{t_2}^3 t_1 E_2 E_1}{12(t_1 E_1 + t_2 E_2)} k_1 \tag{3.13}$$

with

$$k_1 = 4 + 6\frac{t_1}{t_2} + 4(\frac{t_1}{t_2})^2 + \frac{E_1}{E_2}(\frac{t_1}{t_2})^3 + \frac{E_2}{E_1}\frac{t_2}{t_1} \tag{3.14}$$

Since the moment-of-inertia of the polysilicon/metal composite layer is

$$I_3 = w(t_1 + t_2)^3/12 \tag{3.15}$$

the effective Young's modulus of this layer, denoted E_3, is therefore

$$E_3 = EI/I_3 \tag{3.16}$$

Now the polysilicon/metal composite layer (with E_3 and I_3) can then be combined with the silicon nitride layer (with E_4 and I_4) using the same method as described above.

Under the small deflection model, the linear displacement at the end of the beam, d_{max}, due to a bending moment M is

$$d_{max} = \frac{Ml^2}{EI} \tag{3.17}$$

where M is a torque acting at the end of the beam.

Mechanically, the choice of the flexural rigidity of the beams must be a compromise. On one hand, to achieve large displacements, a small EI is desirable. On the other

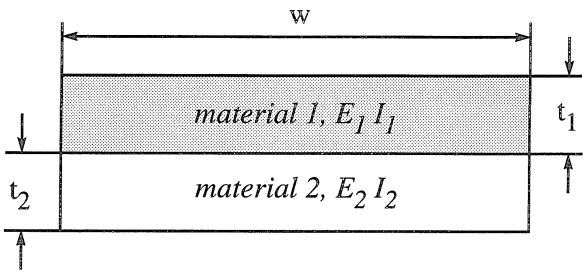

Figure 3-5: Schematic of a two-layer beam structure.

hand, the resonant frequency [4] of the actuator will increase with an increasing EI.

Bending due to intrinsic stress

Different levels of intrinsic stress associated with various structural layers contribute to a net bending moment acting on the cantilever beams and plates. Potentially this will result in the entire actuator having a curved, rather than flat, shape at rest. The magnitude of the curvature, ρ, of a two-layer plate can be calculated using [117]

$$\frac{Ph}{2} = \frac{E_1 I_1 + E_2 I_2}{\rho} \tag{3.18}$$

where P is the lateral force due to the intrinsic stress in one of the layers (see Fig. 3-6), h is the total height of the bi-material layer with

$$h = t_1 + t_2 \tag{3.19}$$

E_1 and I_1 are the Young's modulus and moment of inertia of the top layer, E_2 and I_2 are the Young's modulus and moment of inertia of the bottom layer, and ρ is the radius of curvature of the plate.

[4] In our design, ANSYS© finite element models are used to simulate the mechanical responses of the actuators.

Temperature-variation-induced bending

Thermally, as the temperature of the flap rises, the thermal mismatch of different materials in the composite layers will cause the flap to bend down, which is not desirable in our current project. Given the geometry and material composition, this bending can be calculated by using a model developed for a bi-metal strip thermostat [117]. The thermal-heating effect has been used to make micromachined thermal actuators [7, 95].

For simplicity, we consider the polysilicon and silicon nitride layers as a single layer because the thermal expansion coefficients and Young's moduli of these two materials are relatively close compared with those of gold.

For the metal and polysilicon/nitride composite layers, respectively (Fig. 3-6), a_1 and a_2 denote the coefficients of expansion, E_1 and E_2 denote their Young's moduli, I_1 and I_2 are the moments of inertia of the two cross-sections and d_1 and d_2 are their thickness. The total thickness of the strip, h, is

$$h = t_1 + t_2 \tag{3.20}$$

The magnitude of axial force is P as the temperature rises from t_0 to t. According to beam bending theory,

$$\frac{Ph}{2} = \frac{E_1 I_1 + E_2 I_2}{\rho} \tag{3.21}$$

At the interface of these two layers the unit elongation occurring in the longitudinal direction must be equal, therefore

$$a_1(t - t_0) + \frac{P}{E_1 a_1} + \frac{a_1}{2\rho} = a_2(t - t_0) - \frac{P}{E_2 a_2} - \frac{a_2}{2\rho} \tag{3.22}$$

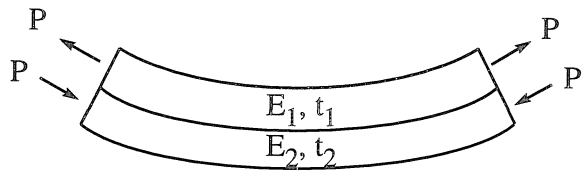

Figure 3-6: Sketch diagram of a two-layered composite beam curved due to longitudinal stress P.

Based on Eq. 3.21 and 3.22,

$$1/\rho = \frac{(a_2 - a_1)(t - t_0)}{\frac{h}{2} + \frac{2(E_1 I_1 + E_2 I_2)}{h}(\frac{1}{E_1 a_1} + \frac{1}{E_2 a_2})} \tag{3.23}$$

Summary of design parameters

A total of 15 test structures have been designed. Sizes of plates vary from 250 μm to 900 μm on the side while the lengths of the support beams are between 100 to 360 μm and the beam widths range from 14 to 50 μm.

Etch holes (typically 15x15 μm^2 in area) are strategically placed in the plate to allow plate release in a short amount time, therefore minimizing damage on structural layers to the sacrificial etchant (Fig. 3-2). On the other hand, the number of etch holes can not be overwhelmingly large so as to reduce the flap's air-pumping capability. At this moment, the effect of etch holes on the flow is not a major concern.

3.2.2 Actuator Fabrication

The fabrication process using surface micromachining is briefly described in Fig. 3-7. The complete process sequence is divided into six different stages, *a* through *f*. Details are discussed in the following.

Stage a

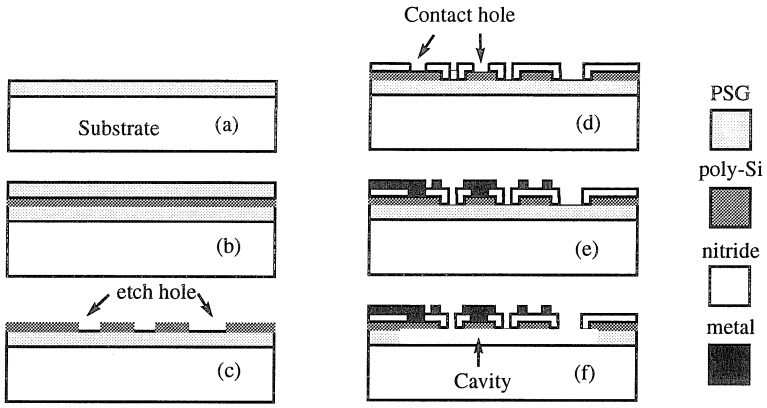

Figure 3-7: Fabrication process for air-coil magnetic air-coil actuators.

Processing starts with a wafer similar to the one used for the shear-stress sensor fabrication; the wafer has a four inch diameter and is polished on the front side. A 2.5-μm-thick LPCVD phosphosilicate glass (PSG) [5] sacrificial layer with a measured 6 wt % phosphorous content is first deposited on the wafer surface, followed by a 6000 Å thick LPCVD polysilicon deposition at 620 °C . At this deposition temperature, the polysilicon is known to have been completely crystallized [57].

Stage b

The wafer is deposited with another 5000 Å thick PSG. This layer facilitates the doping of the polysilicon layer from both sides to minimize polysilicon resistance and to avoid uneven stress distribution due to one-sided doping. Annealed of the wafer at 950°C for one hour releases the intrinsic stress [115]. During the annealing the polysilicon is doped by phosphorus diffusion and the resulting sheet resistivity is measured (with a four-point probe) as 50$\Omega/\Box$.

Stage c

The top PSG layer is subsequently removed using buffered HF solution. The polysilicon layer is patterned to form plates and beams; it is then etched using SF6 plasma.

[5] See Appendix A for fabrication details of underlined processes.

Stage d

A 3000Å -thick LPCVD low-stress silicon nitride layer is deposited at 820°C (with the SiH_2Cl_2/NH_3 ratio being 4) to provide electrical insulation. The silicon nitride is then patterned and plasma etched to create electrical contact holes in which the underlying polysilicon is exposed. The photoresist is stripped and the wafer is piranha cleaned.

Stage e

A total 4000 Å -thick chromium and gold composite layer is used as the metallization with the Cr (100 Å in thickness) serving as adhesion-enhancement layer between the gold and the silicon-nitride layer. Gold is used because of its chemical stability in concentrated HF solution, the sacrificial-layer remover.

Before using the Cr/Au metallization, aluminum was tested. Approximately 4000 Å aluminum layer was evaporated and patterned to form the coils (no Cr is needed to prompt adhesion). We used BHF and oxide *pad etchant* [88] to etch the sacrificial layer; this is because the conventional oxide sacrificial-layer etchant, 49% HF attacks aluminum quickly. Still, in order to completely under-cut a 200x200 μm^2 plate size, it took the pad etchant approximately 3 hours and BHF 30 minutes. The slow under-cut etch rate, together with the non-zero, albeit slow, etch rate of these etchant on the Al metallization, makes the yield of actuators unacceptable ($\sim$10 %) due to metallization failure.

Stage f

With Cr/Au metallization in use, it is found that 49% HF can be used to completely undercut the plate structure without damaging the metallization; the etching process takes about 2 minutes to complete. Etching of the plate materials (polysilicon and silicon nitride) is minimal.

Actuator release and associated stiction problems

The subsequent die-scale drying process is essential to obtain a high yield. During the liquid-drying process, surface micromachined suspension structures (typically with small spring constants) can be pulled down to the substrate by the liquid trapped beneath them when the liquid above them has been removed first. The contact between the plate and the underlying substrate frequently becomes a permanent bond due to surface chemistry. This stiction problem is especially important for the current process because the actuator plates all have large surface areas.

Several authors have reported on various drying techniques [4, 81, 86, 45]; these are reviewed in more detail in section 4.2. Our standardized process includes rinsing the wafer in de-ionized water for 20 minutes, and in acetone and then in alcohol for 1 minute each. The alcohol treatment modifies the surface chemistry [4] and reduces the tendency of bonding. The wafer is baked dry by an infrared lamp. The plate stiction to the substrate is almost negligible and a high yield, nearly 100%, is obtained right after the release/drying process. A finished actuator is shown in Fig. 3-8; it has a plate area of 300×300 μm^2; the length and width of the supporting beams are 200 μm and 24 μm, respectively. This particular actuator contains 6 turns of coils. Fig. 3-9 is a close-up view showing details of etch holes.

It has been observed that actuators can be pulled down and sticks to the substrate during device operation. For example, when a coil current is applied, the tendency for stiction becomes more pronounced. This is believed to be due to electrostatic forces acting between the plate and the substrate. Incidentally, the intrinsic bending phenomena also helps getting useful actuator data by counteracting the electrostatic forces.

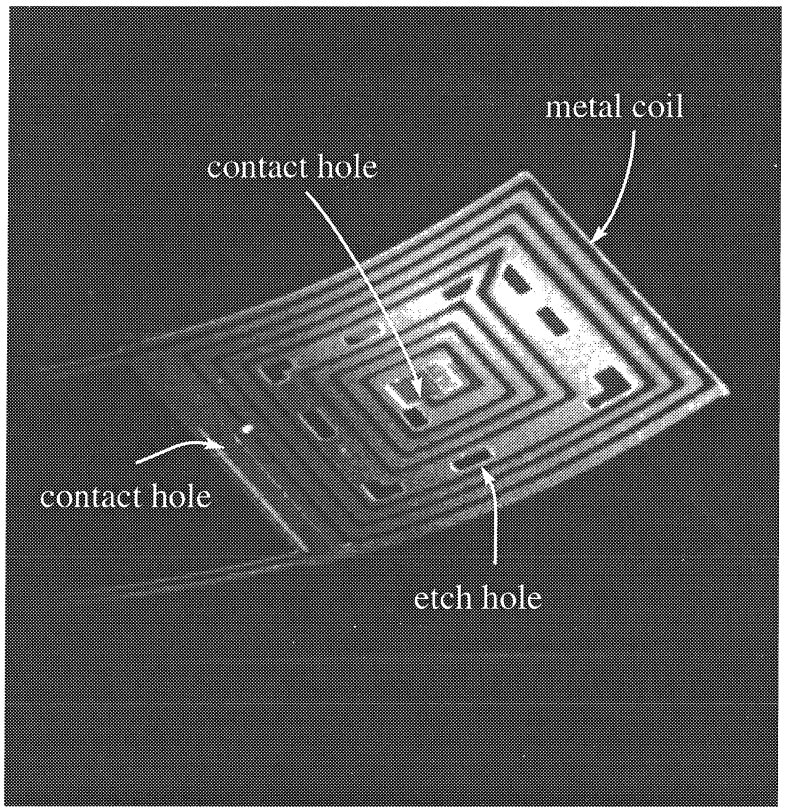

Figure 3-8: An air-coil magnetic actuator supported by two cantilever beams.

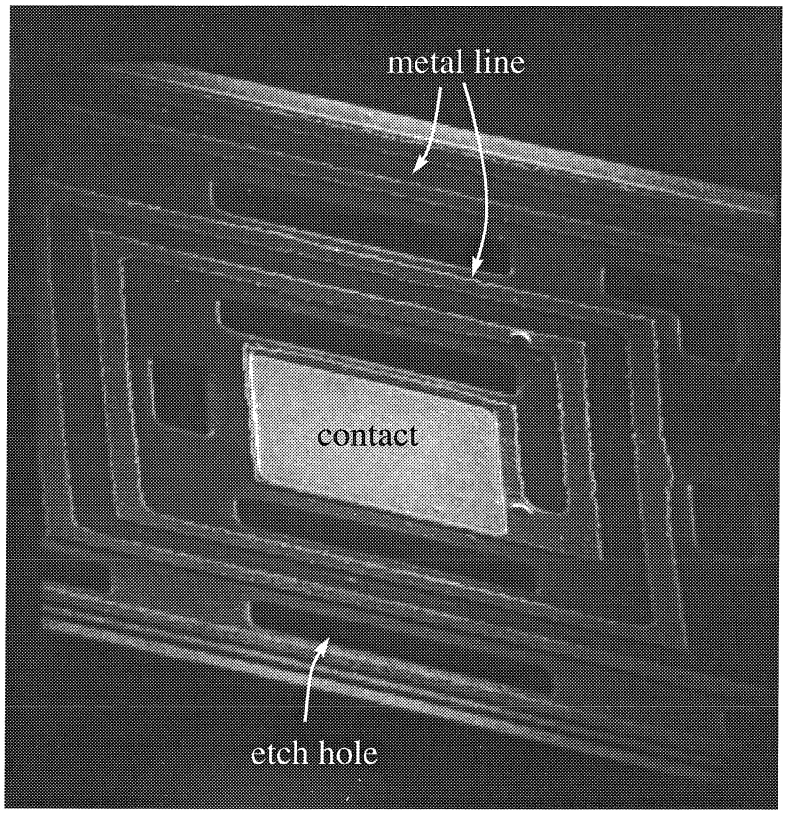

Figure 3-9: A close-up view of a air-coil magnetic actuator.

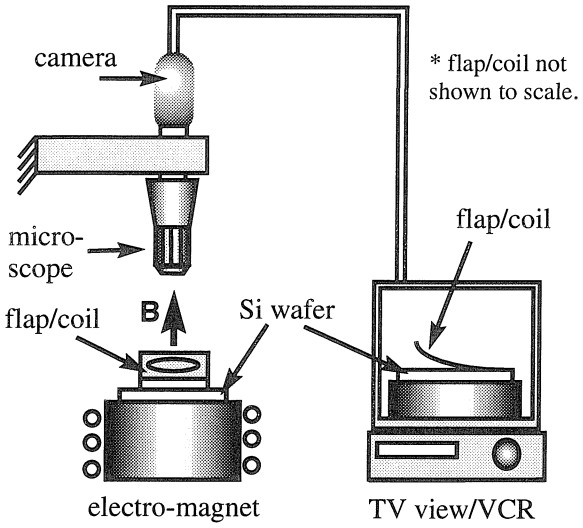

Figure 3-10: Video microscopy inspection setup for the air-coil magnetic actuator.

3.2.3 Actuator Testings

We have studied the actuator bending due to intrinsic stress and thermal effect, and the magnetic actuation using an externally applied magnetic field. The microscope/video setup shown in Fig. 3-10 and Fig. 3-11 is used for monitoring the side profile of an actuator. An electromagnet is used to provide the magnetic field from underneath the actuator that carries coil current ranging from 0 to 50 mA. The electromagnet can produce a variable magnetic flux density in the air ranging from 0 to 1.76 kGauss (1.4×10^5 A/m) on the surface of the magnet core. The $\vec{B}$ of the electromagnet is calibrated with respect to the vertical distance to the core; the result is shown in Fig. 3-12. Note that actuators are placed at least 0.5 mm away from the surface of the electromagnet due to the thickness of the silicon wafer. Within the actuation range, H is a linear function of the vertical distance d; their relationship is given by

$$H = 14 \times 10^4 - 2.8 \times 10^4 d \tag{3.24}$$

H has an unit of A/m whereas d is measured in mm.

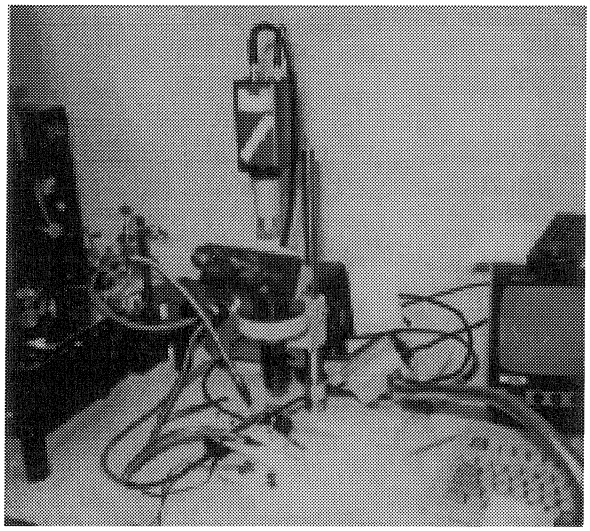

Figure 3-11: A picture of the complete system for observing micro actuation.

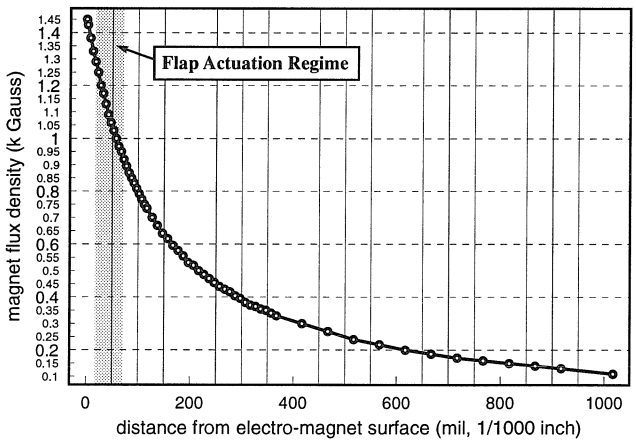

Figure 3-12: Measured magnetic flux density vs. the vertical distance from the surface of the magnetic core.

Actuator bending due to intrinsic stress

Upon release from the substrate, all actuators exhibit an out-of-plane bending. The bending varies from one device to another, being generally large for big plates and small for small ones. The magnitude of the bending is measured as the vertical displacement at the free end of the plate.; some typical values of bending magnitude for several different actuators are listed in Table 3.1. The intrinsic bending is significant compared with the length scale of these actuators.

To verify whether the intrinsic stress is contributed by the metal, post-release processing is conducted to remove the metallization using wet etchant. The intrinsic-bending magnitude of several flaps before and after metallization (both Al and Au) removal is compared: no difference is detected. This test therefore proves that the metallization does not contribute significantly to the intrinsic bending.

To calculate the radius of curvature of the plate due to intrinsic stress, we use a simple model of 3000 Å thick silicon nitride on top of 6000 Å thick polysilicon. Assuming that the plate bending is much larger than the beam bending, we can get a rough estimate of the bending due to intrinsic stress by Eq. 3.18. The low-stress nitride has a known tensile stress on the order of 150 MPa [102]. The stress of LPCVD polysilicon is much less predictable than that of the silicon nitride; it has been observed that the stress could change from tensile to compressive for different wafers in the same deposition batch. However, it has been found that polysilicon deposited under conditions similar to ours can have an average stress very close to zero [65]. Using the Young's modulus of 300 GPa for silicon nitride and 150 GPa for polysilicon, a ρ= 600 μm for a 860x430 μm^2 plate. is predicted. This agrees well with the measured radius of curvature for this plate, which is about 700 μm.

As a side note, when aluminum was used as metallization, we found that the intrinsic bending for a given device increased by about 25% when the devices are further annealed at 400 °C (in an effort to reduce the Al-polysilicon contact resistance). This

flap length (μm)	flap width (μm)	beam length (μm)	beam width (μm)	max. deflection (μm)
200	200	100	14	75
300	300	200	18	160
400	350	200	14	303
860	350	200	18	540

Table 3.1: Measured magnitude of intrinsic deflection for several magnetic actuators.

observation implies that annealing can significantly increase Al stress, a result which agrees well with previous studies on Al stresses [20]. Annealing released actuators with Au/Cr coils was not attempted.

Thermal motion

The resistance of the complete current loop, including the metal coils and the polysilicon return path, is typically 50 Ω. The polysilicon plate contributes a majority (60-70%) to the total resistance. Under a typical biasing current between 10–60 mA, the ohmic heating power ranges between 5 to 180 mW. Within this power input range, the temperature rise on the plate caused by the ohmic heating can contribute to a significant deflection of the flap. At the free ends of these plates, horizontal and vertical displacement of at least 100 μm have been observed at 60 mA bias in almost all devices. In one thermal actuation test for a flap 860x350 μm^2, the side profiles of the flap before and after applying coil current were captured by video and shown in Fig. 3-13. The magnitude of the thermal bending is comparable with previously published data [7].

If we consider our plate to essentially be a bi-layer thermostat composed of a gold layer and a composite nitride/poly layer, we can use Eq. 3.23 to obtain an estimate of the overall plate temperature (while neglecting the heat loss to the substrate and the air). Then, using thermal expansion coefficients of gold as $14.2 \times 10^{-6}/°C$ [131] and of silicon nitride/polysilicon as $2.8 \times 10^{-6}/°C$ [87], an overall plate temperature of roughly

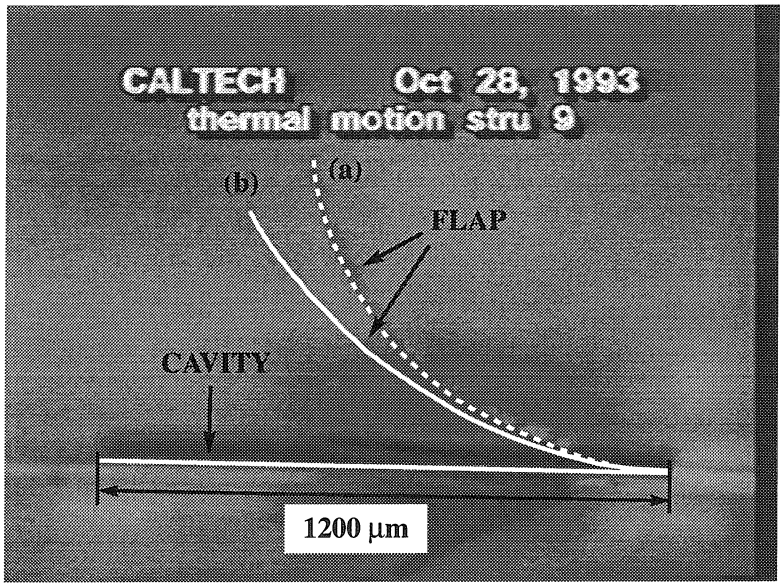

Figure 3-13: Thermal actuation under a 30 mA DC biasing. The area of this particular plate is 860×250 μm ^{2} and the supporting cantilever beams are each 280 μm long and 24 μm wide.

300 °C is obtained. Note that the heat from a plate at around this temperature could potentially alter flow pattern through natural convection; however, it is also noted that flow cooling will reduce the surface temperature at a given power.

The frequency response of the thermal actuation of our actuator (in still air) is obtained by driving it with a square wave of current (50mA 0-peak). The vibration amplitude is measured by illuminating the vibrating flap with a stroboscope, allowing accurate measurement at higher frequencies. A typical amplitude spectrum is plotted in Fig. 3-14 for an actuator with a plate size of 300x300 μm^2 and supported by two 200 μm long and 18 μm wide cantilever beams; it clearly shows a band-width of about 1 kHz. An ANSYS © simulation of the same structure used in testing also showed the first mode resonant frequency to be at about 1kHz.

At large current input (> 60 mA), electrical failure occurs. It has been observed that materials (Au, Cr and polysilicon) inside the contact hole region become fused together, possibly creating a alloy of Au, Cr and Si. The overall resistance of the

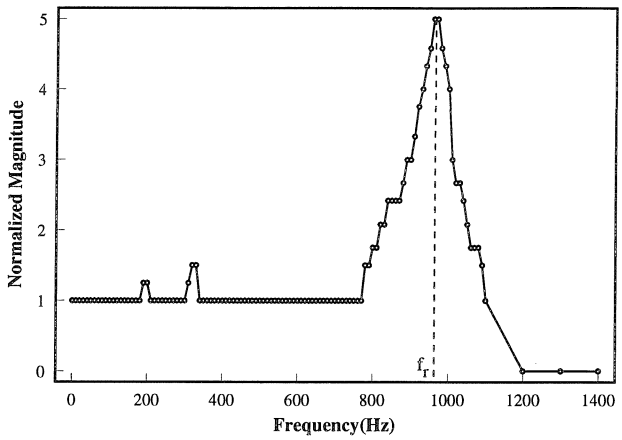

Figure 3-14: Frequency spectrum of thermal actuation.

current loop becomes approximately ten times larger after the alloying process.

Magnetic motion

In order to separate the thermal motion from the magnetic motion, we first apply a DC current to the actuator and observe the thermal motion of the flap. After the plate has reached thermal equilibrium and stays still, the magnetic actuation is achieved by turning on the electro-magnet to apply an external magnetic field. If the reverse strategy is used, i.e. the magnetic field is first applied and then the biasing current is turned on, it would be difficult to distinguish the thermal and magnetic induced movement.

Under a 1.4 kG magnetic flux density and a 30mA coil current (about 70mW) flowing through eight turns of coil, the same plate achieves approximately ± 100 μm DC vertical deflection. The grabbed video image of the magnetic motion side-profile is shown in Fig. 3-15 as an example.

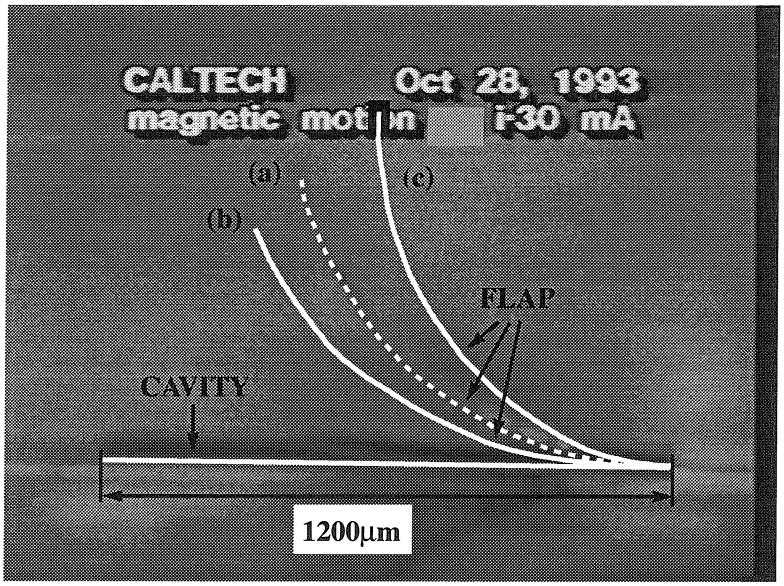

Figure 3-15: Magnetic actuation under external magnetic field perpendicular to the silicon substrate. (a) Profile of the actuator before applying magnetic field (under thermal equilibrium); (b) the profile after a downward movement; (c) the profile after an upward motion. The actuator is identical to the one in Fig. 3-13.

3.2.4 Summary and Future Work

Air-coil type magnetic actuators have been developed and large displacements in both directions magnetic actuation have been demonstrated inside an external magnetic field and under a biasing coil current of 0-60 mA. Actuators are fabricated using surface-micromachining techniques;special release/drying process is adopted to avoid surface stiction.

However, this type of magnetic actuator also have undesirable characteristics, including intrinsic-stress bending and thermal actuation. The *intrinsic bending* can be reduced by using possibly three methods. Most obviously, by reducing the thickness of the silicon nitride layer and the polysilicon layer, ρ can be made smaller. Secondly, the intrinsic stress of the silicon nitride can be further reduced by using different LPCVD recipes [102]. Further more, it is possible to use nitride/polysilicon/nitride sandwich layers which the top and bottom nitride-layer thickness being the same;

the net intrinsic effects should be cancelled. However, silicon nitride material traps electric charges easily and the bottom silicon nitride layer will potentially produce actuator/substrate bonding. The *thermal actuation* can be reduced by lowering the over-all current-loop resistance and the required current (i.e. increase number of turns). Currently the polysilicon current-return path contributes large portion of the over-all resistance. However, the resistivity is unlikely to be further reduced by increasing the impurity doping level. Using metal as the return path is certainly an option; however, micro-fabrication processes using over-flying metal bridges or underlying metal plates have been proved difficult.

3.3 Permalloy Magnetic Actuators

3.3.1 Introduction

The first type (air-coil) magnetic actuators have limitations to their performances due to the intrinsic and thermal bending. The actuator must have a flat surface profile and be able to produce large displacement and forces. For this aim, a second type of magnetic actuator is developed; it utilizes electroplated soft magnetic material called Permalloy with 80% Nickel and 20% Fe composition for generating magnetic torques. The torque-generating portion of the actuator is a square-shaped Permalloy plate with an area of $L \times W$ and a thickness of T. The plate is attached to a structural plate supported by cantilever beams or torsional bars. In its resting position, the actuator lies within the substrate plane. When an external magnetic field perpendicular to the plate is applied, the Permalloy plate will be magnetized along its easy axis[6]. An induced magnetization M is created along its easy axis and M interacts with the magnetic field to produce a moment. When the external field is removed, the magnetic domain essentially resume their original random positions and M is reduced to almost

[6]A plate is perpendicular to the magnetic field yet it is slightly tiled to favor out-of-plane motion.

zero.

3.3.2 Actuator Design

There are two types of plate supports. Schematic sketches of an actuator with cantilever-beam supports and with torsional beam supports are shown in Fig. 3-16 and Fig. 3-17, respectively. In both cases, l,w,t are their length, width, and thickness. Discussions of magnetic actuation in this section mainly focuses on bending-beam actuators, which are extensively used in calibration and wind-tunnel tests.

Actuator design has several facets, including mechanics (deflection and fracture strength), fluid dynamics (e.g., flow loading) and magnetism (magnetic force). A compromise among all four requirements must be sought, under the current flow and magnetic field parameters. For cantilever-beam actuators, the deflections due to gravitational and magnetic forces will be analyzed (sections 3.4.1 through 3.4.4). For the torsional bending actuators, which were fabricated but not as intensively tested as actuators with bending beams, only the moment balance equations are given for reference (section 3.4.5).

In discussing actuators with bending-beam supports, we consider the plate as a rigid body and concentrate on solving the beam bending. Because the thickness of the permalloy plate (T) is about 3–4 times the thickness (t) of the structural layer (t) and the combined width of the two parallel beams are smaller than the width of the plate, the moment of inertia I of the plate ($\propto W(T+t)^3$) is much larger than that of the beams ($\propto wt^3$).

Deflection due to gravitational force

The actuator's gravitational deflection should be small to ensure that it will not drop significantly out-of-plane if the chips are positioned downward. This minimizes the

chance of damaging the actuator or affecting the flow unintentionally. The static deflection caused by the weight of the combined polysilicon and permalloy plate is δ_max. It is defined as the vertical displacement at the end of the actuator plate (Fig. 3-18). Here, F is the gravitation force contributed by the structural layer and permalloy, acting at the center of the plate

$$F = LW(T \times \rho_{perm} + t \times \rho_{poly}) \tag{3.25}$$

Translating this F to the end of the support beams produces an identical force F and a moment

$$M = F\frac{L}{2} \tag{3.26}$$

Using the small-deflection assumption [135], the vertical displacement at the end of the cantilever beams (denoted point A in Fig. 3-18) is

$$y' = \overbrace{Fl^3/3EI}^{forcebending} + \overbrace{Ml^2/2EI}^{torquebending} \tag{3.27}$$

and the angle of deflection at the end of the beams is

$$\theta = \overbrace{Fl^2/2EI}^{forcebending} + \overbrace{Ml/EI}^{torquebending} \tag{3.28}$$

The vertical deflection at the end of the plate is therefore

$$\delta_{max} = y' + \theta \ \times L = \frac{Fl^3}{3EI} + \frac{3FLl^2}{4EI} + \frac{FL^2l}{EI} \tag{3.29}$$

The density of electroplated Permalloy and LPCVD polysilicon are $\rho_{perm} \sim 8.9 \times 10^3 kg/m^3$ and $\rho_{poly} \sim 2.3 \times \ 10^3 kg/m^3$, respectively. The Young's modulus of the polysilicon material is $E = 160 \times 10^9 N/m^2$, and the moment-of-inertia for the two

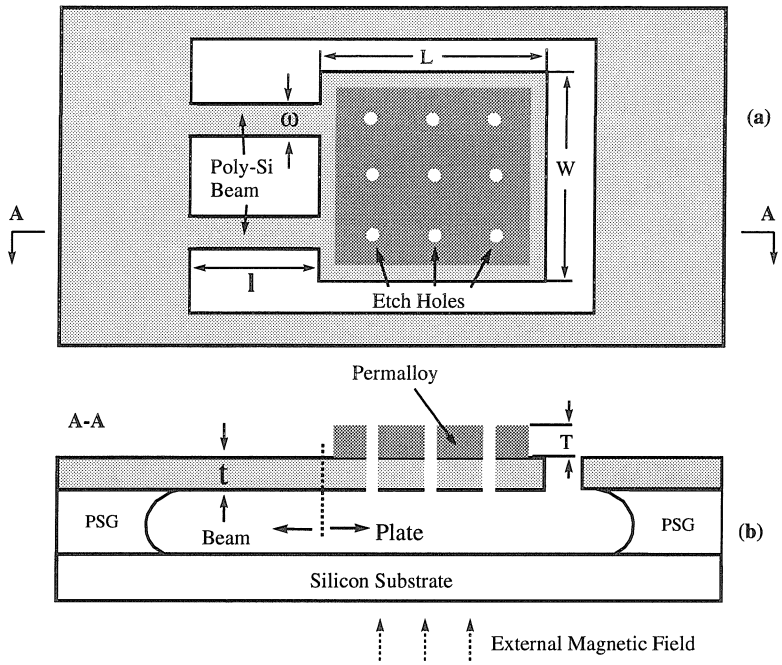

Figure 3-16: Schematic of an out-of-plane permalloy magnetic actuator (so called a micro flap). (a) Top view and (b) side view.

beams in parallel (with a width of $2w$) is

$$I = (2w)t^3/12 \tag{3.30}$$

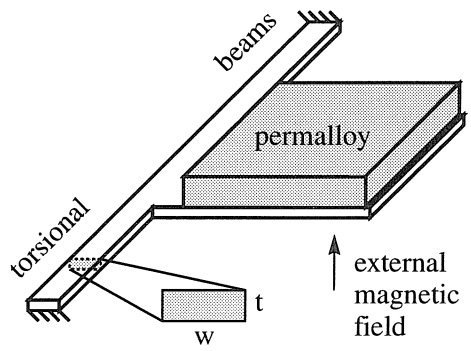

Figure 3-17: Schematic of a Permalloy actuator with torsional beam support.

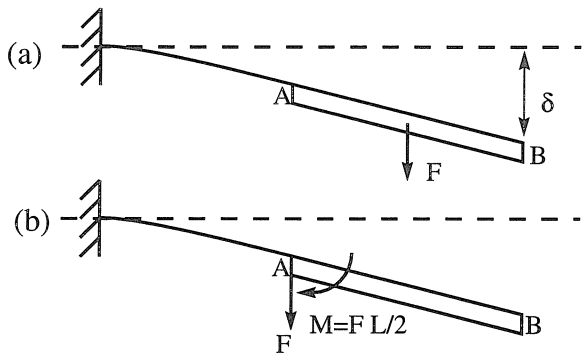

Figure 3-18: Schematic diagram of the relative profile of an actuator under gravitational force. (a) The gravitational force F acting at the center of the plate; (b) F is translated to the end points of the beams, denoted point A.

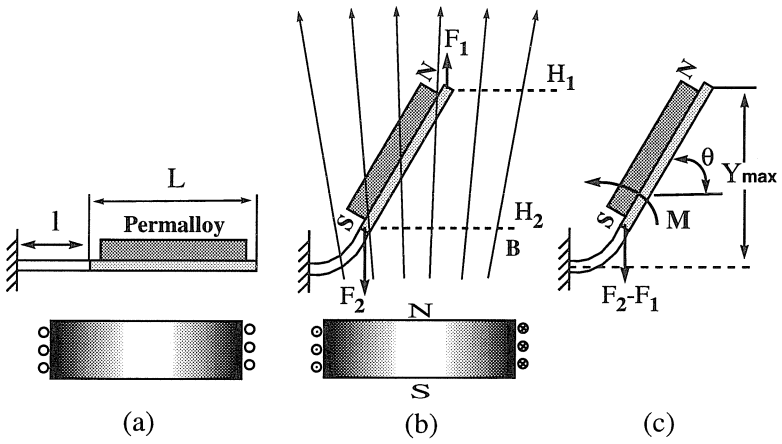

Figure 3-19: Magnetic actuation of an actuator using an external electromagnet. (a) Rest position when $H_{ext} = 0$; (b) out-of-plane actuation when $H_{ext} \neq 0$; F_1 and F_2 are the induced magnetic forces on the upper and lower edges of the plate; (c) a simplified analytical model of the flap.

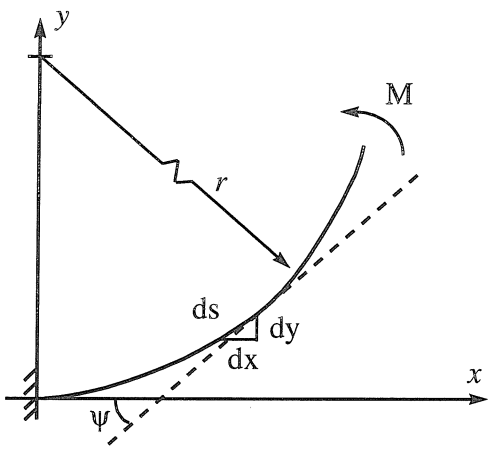

Figure 3-20: Non-linear torque bending of the beams.

Magnetic actuation

Inside a magnetic field, the Permalloy piece will be magnetized and establish a saturated magnetic flux density within its volume. The force acting on the Permalloy piece can be estimated by using an effective magnetic charge model, also used by [60]. Assuming that two magnetic charges of opposite polarities are fixed along the edges at the two ends of the permalloy plate, and the initial flap position is in favor of the out-of-plane (rather than down-to-the-substrate) motion, two point forces can be assumed to have developed on the two ends of the permalloy plate with their directions shown in Fig. 4-14 a, b.

$$F_1 = B_s(WT)H_1 \tag{3.31}$$

$$F_2 = B_s(WT)H_2 \tag{3.32}$$

B_s is the Permalloy saturation flux density, H_1 and H_2 are the magnetic field strengths near the top and bottom ends of the plate ($H_2 > H_1$ in our experimental setup); their values are linearly dependant on the distance away from the surface of the electromagnet core.

First, F_1 is translated to the free end of the beams, thereby simplifying the driving

forces to a counter-clockwise torque

$$M = F_1(L\cos\theta) \tag{3.33}$$

and a downward point force (Fig. 3-19c)

$$F = F_2 - F_1 \tag{3.34}$$

acting at the free ends of the beams.

The force and moment equations will be applied to solve the bending of the cantilever beams. The fundamental equation governing beam bending is

$$\frac{1}{r} = \frac{M}{EI} = \frac{d}{ds}\psi \tag{3.35}$$

In rectangular coordinates the curvature is

$$\frac{1}{r} = \frac{M}{EI} = -\frac{\frac{d^2}{d^2x}y}{\left(1 + \left(\frac{d}{dx}y\right)^2\right)^{\frac{3}{2}}} \tag{3.36}$$

Conventionally, when the curvature is small, the term $(\frac{d}{dx}y)^2$ is much smaller than 1 and is typically ignored, making Eq. 3.36 a linear second-order equation. However, in our current situation, the deflection is large and the complete non-linear second order equation needs to be solved [32].

Ideally, in order to obtain the beam-end angular and vertical deflections, Eq. 3.36 is solved simultaneously with combined torque and force. However, the force system in our studies add complexity to solving the equation. For simplicity, however, the angular/vertical deflections due to M and F are solved separately and the results are superimposed. This method is admissible here mostly because the force deflection predicted by the linear model is small (e.g., maximum angular deflection $< 10°$); the

deflection by F will be approximately 8 – 10 times smaller compared with the one caused by M. It is also known that the actual deflection will be even smaller than the linear-model based calculations because the profile change of the beams will further reduce the bending moment created by F. In all, we believe our method will provide a sound estimation of the over-all bending.

Bending due to torque M

The bending due to torque M is solved by assuming the relationship between the curvature and the torque (Fig. 3-20). At an arbitrary arc length of s,

$$M = EI\frac{d\psi}{ds} \tag{3.37}$$

where ψ is the slope at an arc length of s from (0,0). At the end of the beam, the x and y coordinates are simply

$$x = r\sin\psi \tag{3.38}$$

$$y = r(1 - \cos\psi) \tag{3.39}$$

Under the torque M, which is constant along the beam length, the cantilever beam assumes the shape of an arc, with the radius of curvature being r ($r = EI/M$). The maximum angular deflection at the free end of the beam is express as

$$\psi_{max} \equiv \theta_{torque} = l/r \tag{3.40}$$

where

$$\frac{1}{r} = M/EI. \tag{3.41}$$

Combining Eq. 3.38 and 3.39, the coordinates at the end of the beams are

$$x_{(s=l)} = r\sin(l/r) \tag{3.42}$$

$$y_{(s=l)} = r(1 - \cos(l/r)) \tag{3.43}$$

Numerical solution is obtained using the Mathematica© math solver.

Bending due to force F

The force bending can be solved by assuming F is applied at the free end of a pre-curved (circular-shaped) beam, in which case the maximum angular and vertical deflections are [135]

$$\theta_{force} = \frac{(\pi/2 - 1)FR^2}{EI} \tag{3.44}$$

$$y_{force} = \frac{(3\pi/4 - 2)FR^2}{EI} \tag{3.45}$$

The over-all angular deflection of the plate is then (Equation 3.40 and Eq. 3.44)

$$\theta = \theta_{torque} - \theta_{force} \tag{3.46}$$

The vertical displacement at the end of the beams is

$$y_{max} = y_{(s=l)} - y_{force} \tag{3.47}$$

and the maximum vertical deflection at the end of the plate is equal to (Eq. 3.43, Eq. 3.45, Eq. 3.46)

$$y_{max} = y_{(s=l)} - y_{force} + L \times \sin\theta \tag{3.48}$$

Fracture limit

The beams may be fractured by bending when the maximum longitudinal strain at their fixed end exceeds that of the beam material. The fracture strain for LPCVD polysilicon has been experimentally studied by Tai *et. al.* [111] as 0.93%. The fracture strain for silicon nitride thin-film is not directly available; a pseudo value of 3.6% is

Name	Notation	Value
plate length	L	1 mm
plate width	W	1 mm
beam length	l	0.4 mm
beam width	w	0.1 mm
Permalloy thickness	T	5 μm
beam thickness	t	1 μm

Table 3.2: Design parameters of Permalloy magnetic actuator.

derived as the ratio between yield strength (14 GPa) and the Young's modulus (385 GPa). The maximum strain can be estimated as follows

$$\varepsilon_{max} \sim \frac{Mt}{EI} \leq 0.93\% = \frac{\theta_{frac}}{l} t \tag{3.49}$$

θ_{frac} is defined as the theoretical maximum angular beam deflection before fracture takes place.

Summary of current design parameters

The design parameters of the cantilever-beam supported Permalloy magnetic actuator is listed in table 3.2. According to the current design, the deflection is μm.

From Eq. 3.49, it is predicted that polysilicon beams can be bent by a θ_{frac} of 118° before fracture occurs; and the silicon nitride beams will not fracture even after 180° bending. This implies that these actuators will never reach their fracture point in a uniform magnetic field with field lines perpendicular to the chip substrate because the maximum bending angle is limited to 90°. However, it is worth noting that once inside a flow field, flow-induced bending and vibration can create θ larger than θ_{frac}.

Actuators with torsional bars

In a flow field that contains velocity components in the span wise direction, actuator plates are subjected to torsional torque. Cantilever-beam supports allow for large twisting displacement that can damage the overall structure.

We have designed actuators with torsional beam supports, which limit the overall twisting motion (Fig. 3-17). For each torsional beam,

$$T = \frac{\theta}{l} KG \tag{3.50}$$

where T is the torque, θ is the angular displacement, l is the length of the beams, G is the modulus of rigidity (shear modulus) of the material, and finally, K is a factor that depends on the form and dimension of the cross-section. For a torsional beam with a rectangular cross-sectional area of $w \times t$ (Fig. 3-17), letting $w = 2a$ and $t = 2b$,

$$K = ab^3 \left[\frac{16}{3} - 3.36 \frac{b}{a} (1 - \frac{b^4}{12a^4}) \right] \tag{3.51}$$

The shear modulus G, Young's modulus E and Poisson's ratio υ are related by

$$G = \frac{E}{2(1+\upsilon)} \tag{3.52}$$

In one example, the torsional beam has an l of 100 μm, a w of 5 μm and a thickness t of 1.5 μm; in this case, assuming that $\upsilon = 0.3$

$$\theta = \frac{l}{KG} T = T \tag{3.53}$$

K is equal to 4.56×10^{-24} m^4, $G = 6.15 \times 10^{10}$ Pa. A torque of $T = 2.2\mu$Nm is required to produce a 90° bending.

3.3.3 Actuator Fabrication

Processing description

Fig. 3-21 illustrates major fabrication steps.

Stage a

A 3 μm -thick phosphosilicate glass [7] (PSG) sacrificial-layer is first deposited onto a 4-inch silicon wafer. The PSG layer is patterned and etched using BHF to form individual sacrificial-layer "islands" on which actuators will be located. These isolated "island" structures allows the sacrificial-layer etching process to be self-limiting; it is therefore possible to do 50 to 100% over-etch to account for etching non-uniformity on the wafer scale.

After removal of the photoresist, the wafer is annealed in nitrogen ambient at 1000°C for one hour. The purpose of the annealing is two-fold: first it activates the phosphorus content within the PSG, secondly, PSG is known to re-flow under 1000°C and the edges of the islands are made smoother. The structural layer is deposited to cover the whole wafer. In our studies, two structural materials have been used: LPCVD polysilicon and silicon nitride. In the case of using polysilicon as a structural material, the polysilicon is covered by a 0.5 μm -thick PSG layer, which serves as a complimentary phosphorous doping source. During a 1 hour, 950°C stress-relief anneal, the polysilicon is doped from both sides which reduces intrinsic bending due to unbalanced doping concentration. The top PSG layer is later removed by using buffered hydrofluoric acid (BHF).

Stage b

A 200 Å Cr and a 1800 Å Cu thin film are then evaporated over the structural layer as the conductive seed layer for electroplating. The Cr serves to enhance adhesion

[7] See Appendix A for processing details of underlined steps

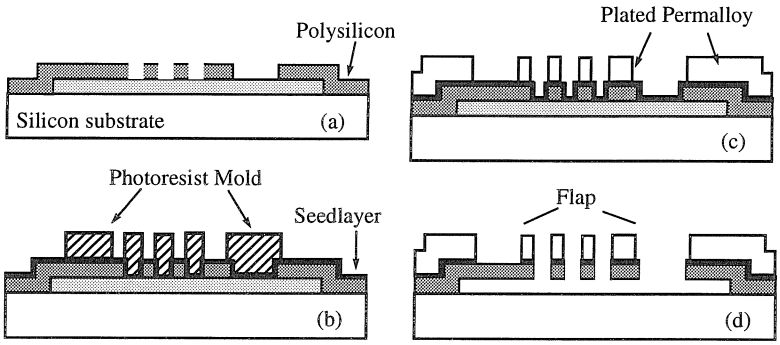

Figure 3-21: Major fabrication steps of a Permalloy magnetic actuator.

between the Cu layer and the substrate (i.e., the structural layer, either silicon nitride or polysilicon). Copper oxidizes easily and the copper oxide layer will complicate the electroplating and subsequent seed-layer removal. Therefore care must be exercised to ensure that the copper layer is exposed to air for as short as possible (this implies spining photoresist right after evaporation). Contact between copper and water need to be avoided, especially.

A 5 μm-thick photoresist (AZ 4400) is applied and patterned to form photoresist fences, inside which permalloy ($Ni_{80}Fe_{20}$) electroplating takes place. This photolithography is not followed by development because the photoresist is needed to prevent copper oxidation. The wafer is then UV exposed again using a specially ring-exposure set-up. Photoresist near the edge of the wafer is exposed. After this point, the photoresist is developed and the electroplating process takes place almost immediately.

The Permalloy electroplating technique was originally developed in the thin-film magnetic-head industry and is known to create high quality permalloy films [19, 6]. During the plating process, the wafer is affixed to the cathode and is oriented in such a way that an external biasing magnetic field ($\sim$ 450 Gauss, or 450 Oe, near the wafer area) is parallel to the supporting beams (Fig. 3-22). Electroplating takes place at 5 μm/hour under a bias-current density of 8–12 mA/cm^2. During the electroplating process, the plating bath is maintained at a pH value of 2.7.

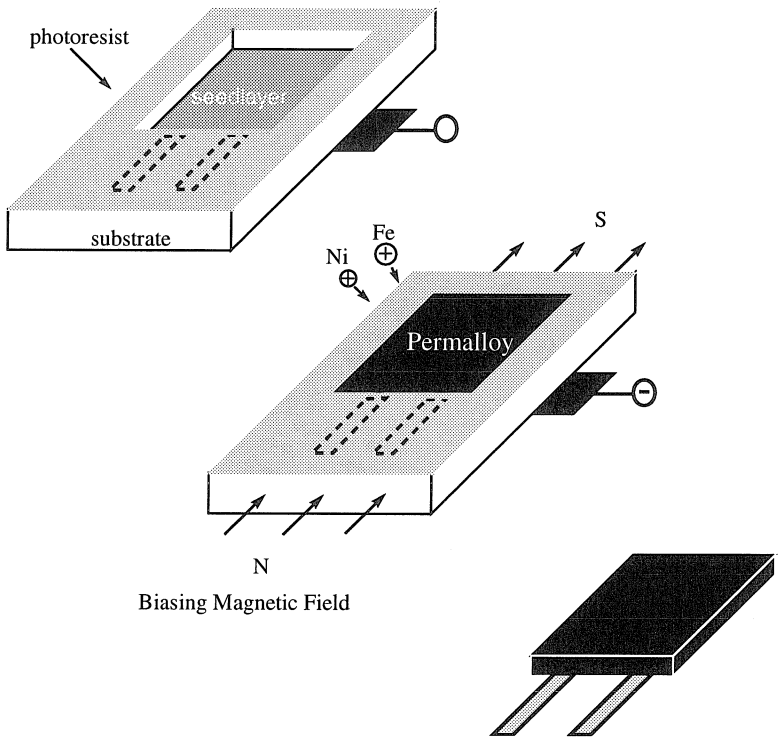

Figure 3-22: Sketch diagram illustrating the Permalloy electroplating procedure and setup.

Stage c

After electroplating, the wafer is flood-exposed with UV for one minute and the photoresist plating frame is removed with photoresist developer. This is again followed by Acetone/Alcohol photoresist removal.

Stage d

The seed layer is etched away by using Cu etchant [8] and then Cr mask etchant. For the current range of Cu thickness, etch is completely within one minute. The Cr-layer removal can be done using either commercial product—transene:pa or diluted HCl.[9]. Actuators are then released by 49% HF after 20 minutes. All permalloy plates stand well in HF, as well as in Cu and Cr etchant.

Shown in Fig. 3-23 and Fig. 3-24 are top and perspective views of fabricated actuators; no intrinsic bending was found for both types of flaps. To facilitate the sacrificial release process, etch holes (30 μm by 30 μm in size, and 250 μm apart) are opened on the plate.

Care must be taken to ensure that during the seed-layer etching, no air-bubbles stay within the etching holes and prevent seed-layer removal. In the current process, after the wafer is DI water rinsed following the photoresist development in Stage C, they are not dried but transferred directly into the Cu etchant. If the wafer is dried and then immersed in Cu etchant, the solution may not be able to replace air content in all the etching holes on the wafer.

Since the micro-flaps have large surface areas and the supporting beams are soft (spring constant $\sim$ 100 μN / 1 mm=0.1 N/m), they can be easily pulled down by surface tension to the substrate and form permanent bonds—guckel:rl, alley:rl if conventional drying techniques are used. To ensure high yield, a magnetic levitation

[8] Cu etchant: 100 water: 5 acetic acid: 5 hydrogen peroxide
[9] Cr etchant: 10 water: 1 HCL

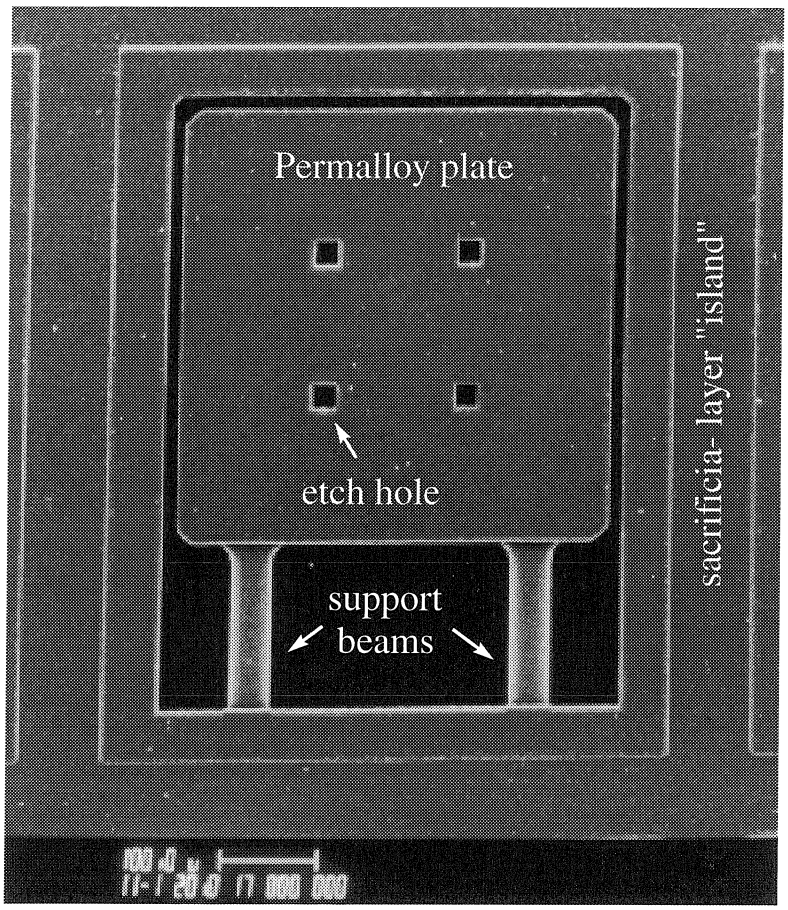

Figure 3-23: A top view of a completed Permalloy magnetic actuator.

technique has been developed. In this unique rinse/drying process, magnetic force counteracts the surface tension force to prevent the actuators from coming into contact with the substrate, therefore guaranteeing that almost 100% yield is routinely achieved. One advantage of using his technique is that it does not require any complicated equipment for pressure and temperature cycling. The detail about the release process can be found in Chapter 4.

Magnetic properties of Permalloy

The electroplated Permalloy has a composition of 80% Nickel and 20% Iron. Thin film Permalloy is a preferred soft magnetic material for two main reasons: the material

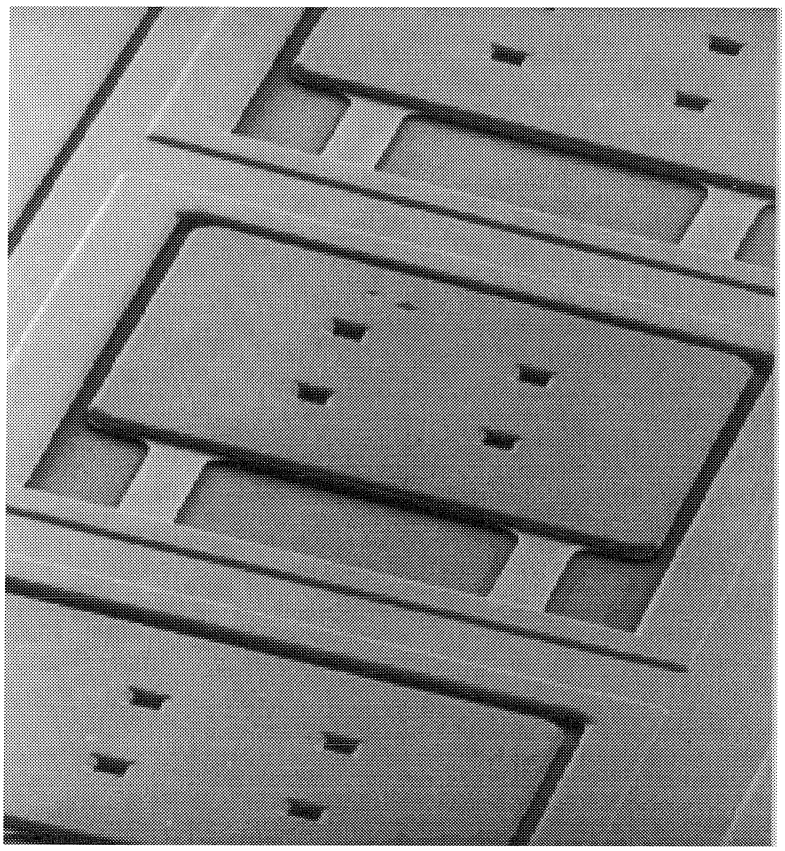

Figure 3-24: A perspective SEM micrograph of a Permalloy magnetic actuator within an array.

property	value
Saturation magnetic flux density B_s	1 - 1.5 Tesla
Coercive force H_c	0.6 Oe
Relative permeability μ_r	4500
Remanent magnetization B_r	1-10 Gauss

Table 3.3: Permalloy magnetic material properties.

has a very low or zero magnetostriction effect and stress-free films can be realized; the magnetic switching speed is fast (on the order of femto-second to micro-second), ideal for magnetic recording media.

The Permalloy material has a poly-crystalline structure containing a large number of magnetic domains. Each magnetic domain has 10^{10} to 10^{15} atoms and is spontaneously magnetized in one direction at room temperature. The directions of magnetization of different domains are randomly organized. Despite this, there are directions of easy and hard magnetization; this phenomena is called crystalline an-isotropy. In our experiments, the direction parallel with the external magnetic field during the plating process is the *easy axis* while the orthogonal in-plane direction is the *hard axis*. H_k is defined as the magnetic field intensity needed to saturate a soft magnetic material in a specific direction. In the direction of easy magnetization, the easy axis, $H_{k,easy}$ of the hysteresis is small. In the direction of difficult magnetization, the hard axis, $H_{k,hard}$ is much larger. During our electroplating, the direction of the biasing magnetic field dictates the easy axis—abel:pa. This phenomena has been studied by Takahashi—takahashi:pa and it has been found that an external field of $H \geq 30$ Oe is sufficient to induce the direction order. Establishment of the easy axis can also be achieved by critical cold working and annealing. When an external magnetic field density, H, is applied (in either easy axis as an example), the domain walls move in such a manner that domains favorably oriented with the magnetic field grow at the expense of unfavorably oriented domains.

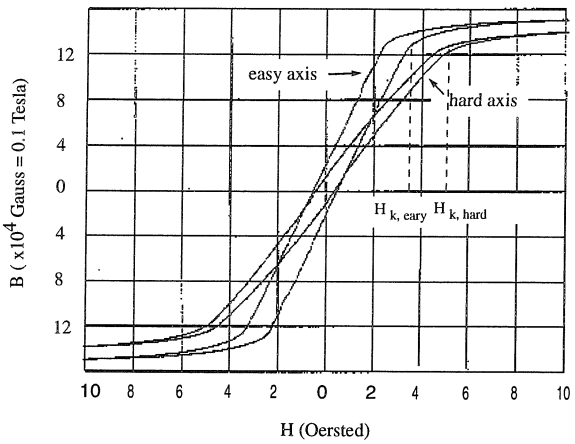

Figure 3-25: B-H hysteresis curves along the easy axis and a direction perpendicular to the easy axis (in plane).

The properties of the electroplated Permalloy is summarized in Table 3.3—temesvary:pa. It should be noted that the shape of the Permalloy plate also favors shape-anisotropy with the plate plane. Experimental B-H hysteresis curves along the easy axis and the hard axis are shown in Fig. 3-25. The magnetic anisotropy in Permalloy is shown to be low; this is a established characteristic for 80% Ni content—stanley:pa.

It is worth mentioning there are two plating techniques - mold plating and frame plating. These two techniques are illustrated in Fig. 3-26. In the frame plating technique, photoresist covers all area of the wafer except where Permalloy is intended (Fig. 3-26a.1). In the mold plating technique, on the other hand, plating occurs in a large portion of the wafer surface; only photoresist fences separate wanted (e.g. the actuator plate) and un-wanted Permalloy material. The un-wanted material is later on removed. Frame plating technique allows more uniform electroplating and the plating parameter is not varied when the geometry is changed.

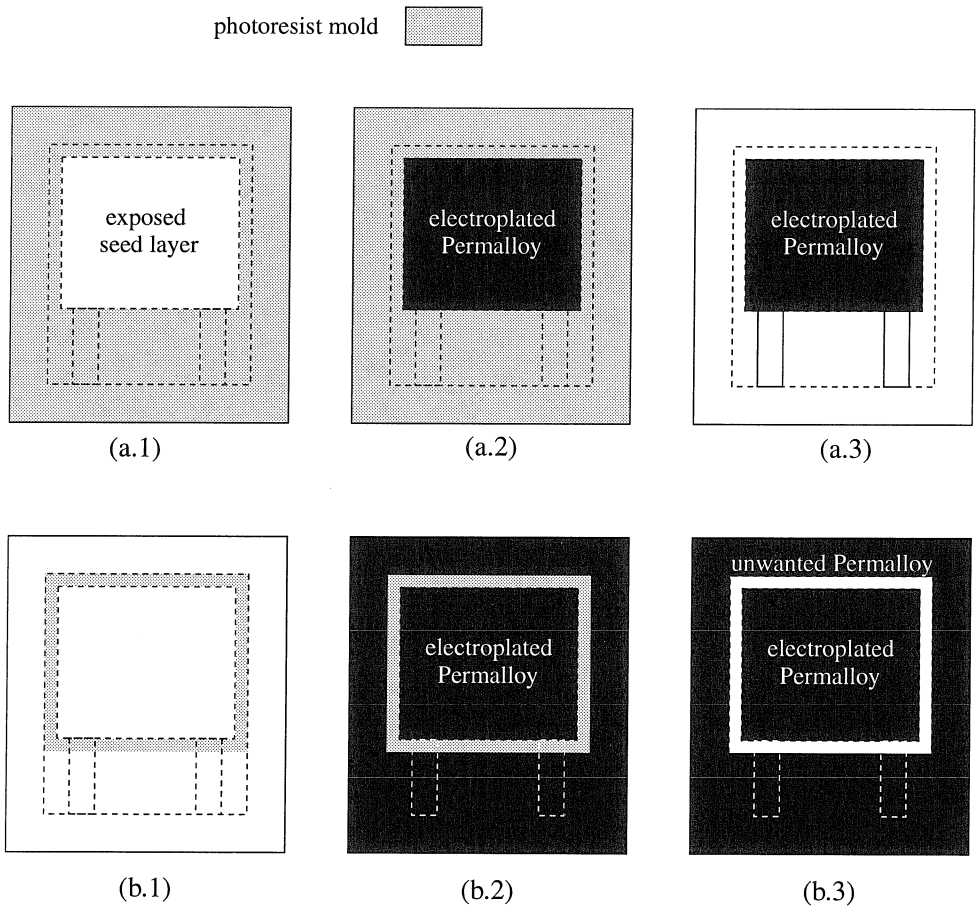

Figure 3-26: Schematic of two important plating techniques: (a) frame plating and (b) mold plating.

3.3.4 Actuation Testings

Actuator calibration in still air

For testing the characteristics of individual actuators in the still air, a strong industrial electro-magnet is used. Actuation is observed by using a microscope-monitoring system (Fig. 3-10). The magnetic field calibration with respect to the vertical height is shown in Fig. 3-12: the field strength around the flaps is linear and can be expressed as $H = 14 \times 10^4 - 2.8 \times 10^4$ d(in mm), where d is the distance from the measurement point to the surface of the magnetic core.

In their resting positions, actuators are separated from the electromagnet by a distance of 0.5 mm, which is the thickness of the silicon substrate. The angular and vertical deflection of the Type-1 actuator is directly measured from the monitor screen, with magnetic field intensity values of up to $6.4 \times 10^4 A/m$ at the chip surface (d=0.5mm). Fig. 3-28 shows the measured deflections, together with theoretical predictions using Eqs. 3.46 and 3.48. A good match between the bending theory and experimental θ and h is observed.

A large-deflection finite element analysis (FEA) model of the flaps is also built (Fig. 3-29) and is currently used as a first-order verification of our analytical calculations. As an example, applying $F_1 = 100\mu$N and $F_2 = 120\mu$N on an actuator, Y_{ma}, θ, and ε_{max} are found to agree with the result by analysis to within 15%.

Under current magnetic field and actuator-geometry parameters, the maximum vertical loading force has been found experimentally—cl:xducer. Using an array of 5×5 actuators to lift a stack of weight (silicon and glass chips) of 222 mg (or 2.2 mN) under the highest magnetic field intensity has been demonstrated. Each individual actuator is therefore capable of withstanding a vertical load of 87 μN.

The time response of the actuator system is not limited by the Permalloy material switch, which has a typically time constant on the order of one pico-second. The

maximum actuation cycling speed is restricted by the electromagnet and the electric-current switching circuitry. Currently the switching is performed using a mechanical switch. The time constant of magnetic-field rise and decay is experimentally measured using a secondary coil; it is within the range of 1 to 10 ms.

Durability tests

In static air, most devices with bending and torsional beams were able to bend by more than 180°C . These actuators can withstand upto 30 m/s air flow in the up-right position.

Inside a turbulent flow field, actuators are subjected to both constant and fluctuating flow loading. The fluctuating part of the flow load is very damaging to the actuators. Actuators are attached to the wide wall of a small sized wind-tunnel (at Caltech) with a maximum wind speed of 30 m/s. To increase flow fluctuation, we intentionally introduce an obstruction at the upper stream of the wind tunnel. Actuators are placed in various positions: the direction of the plate movement with respect to the mean flow velocity changes from 0° to 45°. At 45°, the shearing (twisting) force is the greatest.

The wind-loading capability of two types of Permalloy actuators is compared. For actuators with bending beam support, there are three types of beams: 2-μm thick silicon nitride, 1-μm thick silicon nitride and 1 μm thick polysilicon. These actuators are oriented 0° to the flow (i.e. the flow velocity is parallel to the plate movement) and zero flow fluctuation is introduced. All three types can survive 25 m/s flow speed. Actuators with 1-μm thick silicon nitride can survive 45 m/s. At 45 m/s flow velocity, the survival rate of actuators with 1 μm -thick polysilicon beams are the worst among three.

Actuators are then subjected to more severe flow conditions, the extreme case being that fluctuation is intentionally introduced up-stream and the actuators are placed

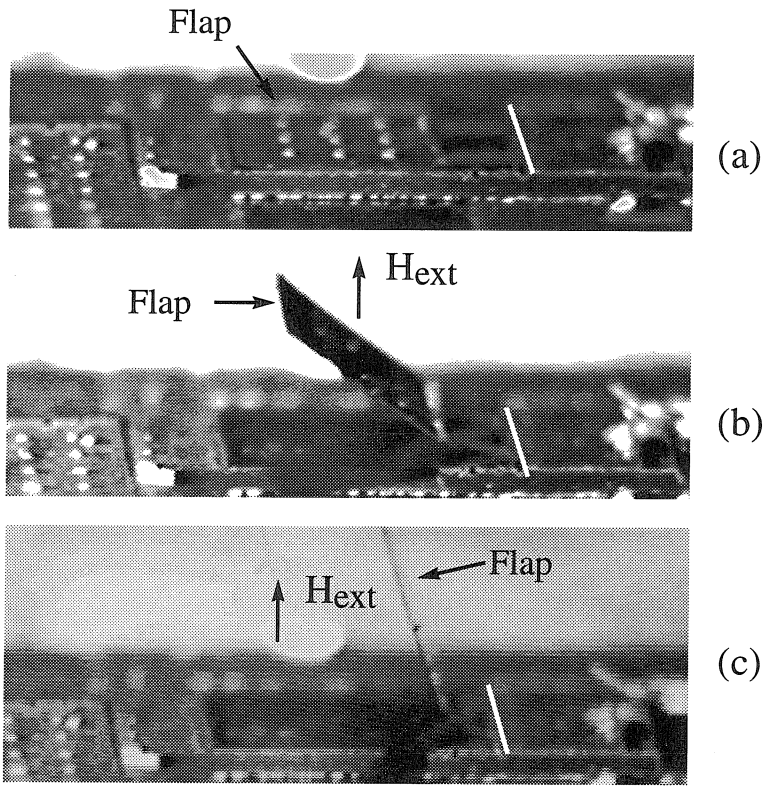

Figure 3-27: Sequential snapshots of the flap actuation (a) before applying the magnetic field; (b) when $H_{ext} = 3.34 \times 10^4 A/m$ ($B_{ext} = 420 Gauss$); (c) when $H_{ext} = 6.4 \times 10^4 A/m$ ($B_{ext} = 800 Gauss$).

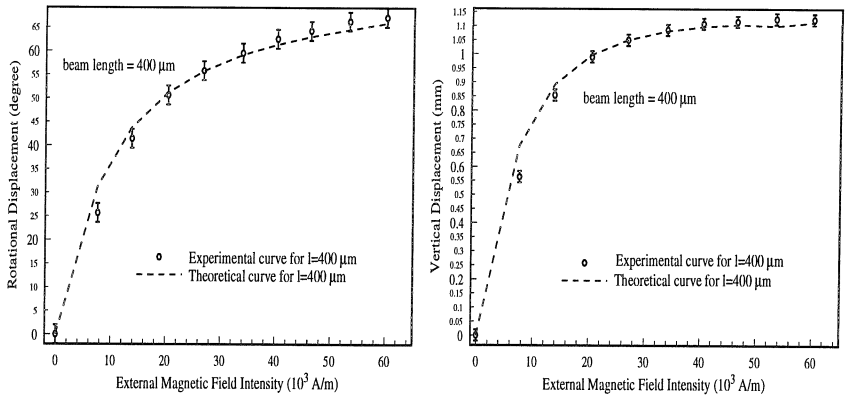

Figure 3-28: Theoretical and experimental rotation angle θ and maximum vertical deflection y_{max} vs. applied magnetic field intensity and flux density for a micro flap. The size of the plate is 1x1mm^2, the beam length and width are 400 and 100 μm and the beam thickness is 1 μm.

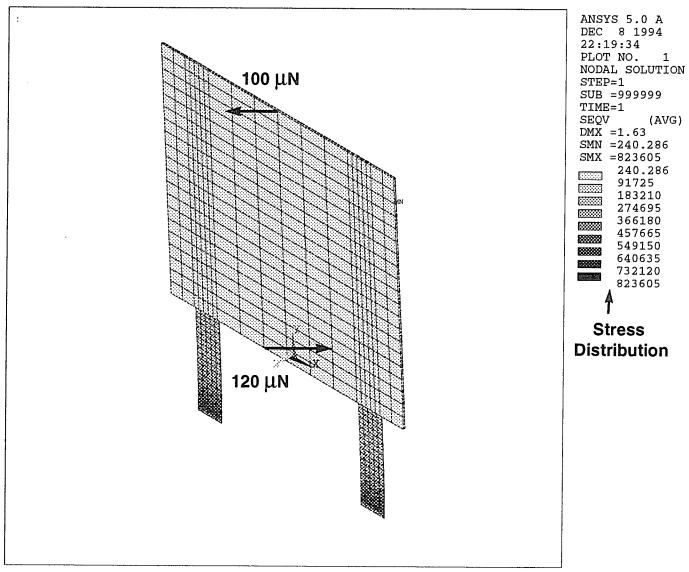

Figure 3-29: An ANSYS© finite element analysis model and simulation results.

45° with respect to the flow. All actuators with bending beams are broken. Actuators with torsional beams that are 5 μm wide and 100–200 μm long all survived the worst-case flow loading. However, actuators with torsional beams wider than 5 μm are also completely destroyed.

Wind-tunnel Testings

Permalloy micro actuators have been installed on a model delta-wing, which has been tested in a wind-tunnel to measure the rolling moment caused by micro actuator movement. The details can be found in Chapter 5.

3.3.5 Summary and Future Work

Magnetic actuators based on electroplated Permalloy material have been developed; large displacements and large forces are demonstrated. The displacements and forces are orders-of-magnitude larger than those for electrostatic driving actuators that are most commonly used. Applications of these actuators in fluid-mechanics projects are illustrated in Chapter 5. These Permalloy magnetic actuators can be used in many different applications. For example, these can serve as micro-mirror arrays for optics applications. An array of Permalloy magnetic actuators with the current geometric parameters has also been used as a micro robotics assembly system—cl:xducer for transportation and manipulation of small parts (e.g., IC chips).

Consider an array of air-coil and Permalloy magnetic actuators within an external magnetic field. Each air-coil actuator can be individually controlled by switching the coil current. A Permalloy actuator can not be turned on and off individually; it obviously can not be used in those applications where individual actuator control is required. Nonetheless, air-coil actuators at the current stage suffers from intrinsic-stress bending and thermal-actuation problems; these issues need to be addressed before these actuators can be successfully used in a wide-range of fluid applications.

Permalloy actuators have exhibited larger work range and force magnitude compared with air-coil ones; the power consumption is also reduced.

An air-coil actuator with individual Permalloy magnetic core will be demonstrated in the future. This hybrid-type actuator will inherit the advantages of both original types.

Chapter 4

MICRO FABRICATION ISSUES

In this chapter, two specific micro fabrication issues related to micromachining are discussed. One is the sealing of surface micromachined cavities using LPCVD materials. This process is encountered in the fabrication process of shear stress sensors. A second one is magnetic levitation-assisted release of surface micro structures after wet sacrificial layer etching. In both cases, large arrays of test structures have been specially made to facilitate systematic studies.

4.1 LPCVD Sealing of Surface Micromachined Cavities

4.1.1 Introduction

Sealing of surface micromachined cavities is commonly used but is rarely systematically observed and studied. In most cases, cavities are sealed under vacuum for different purposes, for example to reduce air damping for electro-mechanical resonators [68], to establish pressure measurement references [73, 37], and to make vacuum electronics [14, 44]. Sealing is achieved by depositing thin film materials on

two neighboring surfaces until two growth fronts meet. Thin film growth is done through Chemical Vapor Deposition (CVD) under either low pressure or atmosphere pressure [68, 73, 37, 38, 21, 104], thermal oxidation growth [38], electron beam evaporation [82, 14], sputtering [137], wafer-wafer bonding [30, 44, 90], and solder glass fritting [66]. In fabricating the shear stress sensor, the thin film sealing deposition must satisfy the following requirement (Fig. ===seal-closeup): first the overall thickness of the deposition must be minimized since the thicker the film, the more heat it will conduct to the substrate; secondly, deposition inside the cavity itself must be small so that the cavity depth will be retained.

In a typical LPCVD deposition environment, the mean-free-path (λ) of gas molecules is given by

$$\lambda = \frac{kT}{\sqrt{2}\pi d^2 P} \tag{4.1}$$

where d si the radius of rigid molecule spheres, P and T are the pressure and temperature of the system, respectively, and k is the Boltzman constant. The λ in a typical LPCVD and PECVD environment becomes comparable with the dimension of micro structures. As an example, take d for air molecules as 3.5 Å , at T=300 K and P=300 mTorr = 40 N/m^2, λ is equal to 190 μm; at a deposition temperature of T=900 K, the λ is 570 μm.

Geometric shadowing due to over-hanging diaphragms reduces the deposition thickness inside the etching channels and the cavity itself. Step coverage of thin films deposited in trenches or cavities are governed by three additional physical processes: direct deposition, surface re-emission and surface diffusion (Fig. 4-1). These processes are distinguished by associated *surface sticking coefficients*, Sc, which is the probability of chemisorption on the surface. For direct deposition, $Sc = 1$; for surface re-emission, $Sc < 1$. The overall sticking coefficient is feature and flux dependant. In conventional IC processes, good step coverage is desired for reliable electrical isolation; a small Sc generally helps to improve step coverage. To this end, slower

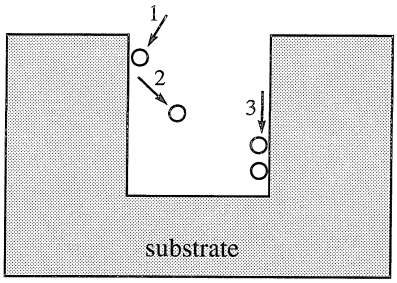

Figure 4-1: Molecule transport and deposition mechanisms: (1) direct deposition, (2) re-emission and (3) surface diffusion (3).

deposition and high flow rate is generally beneficial. Deposition profile within a simple trench configuration has been studied using computational simulation (e.g. Monte Carlo methods). However, simulation becomes difficult when $Sc \ll$ unity. The three-dimensional profile of the etching channel also makes simulation hard.

4.1.2 Approach of Studies

Despite the wide use of cavity sealing, the behavior and mechanism of this process are not systematically studied. In this study, four different thin film materials are used to seal specially designed surface micro structures. Those structures have different cavity opening configuration, different cavity height and different membrane materials. The four sealing materials are Low Pressure Chemical Vapor Deposition (LPCVD) silicon nitride, poly-crystalline silicon and low temperature oxide. Studies by others have found that the deposition conditions (total flux and temperature) will have influence on the step coverage. However, in our studies we only use standardized recipes. The sealing success rate at various deposition thickness are statistically analyzed and the sealing behavior with respect to the membrane materials, gap heights and cavity geometric parameters are revealed for the first time.

4.1.3 Design and Fabrication of Test Structures

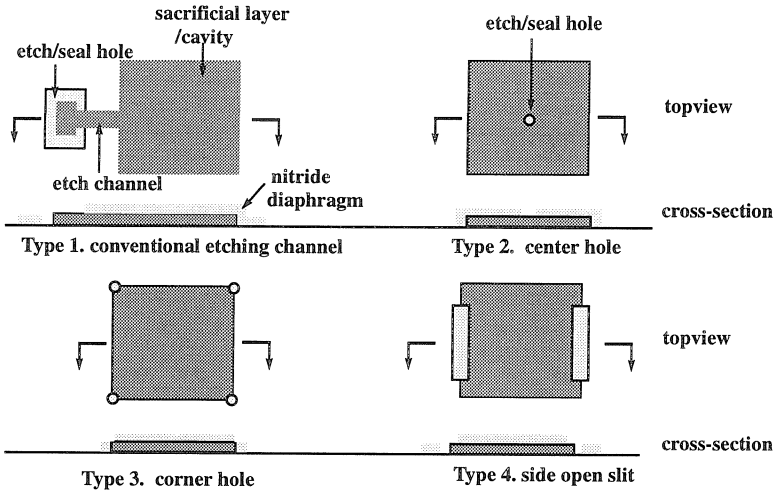

Figure 4-2: Schematic configurations for four different types of test structures.

Shown in Fig. 4-2 are four types of test structures (named type–1 to 4, respectively) which are designed around a square diaphragm with different etch channel features added to it. All diaphragms are square in shape, 200 μm on a side. Since our current study is based on statistical data, a large number of samples is desirable. In our design, each die ($1 \times 1cm^2$) has 126 different cavities (72, 36, 3 and 15 for types 1, 2, 3 and 4 respectively). A four-inch diameter wafer has 48 dies and therefore each individual cavity has a sample space of 48.

Type-1 structures have different numbers (4–6) of etching channels with varying channel widths (2 to 16 μm) and lengths (8 to 38 μm). The feature of type-1 structures is that these channels may have little effect on the mechanical integrity of the diaphragms. Besides, undesirable film deposition inside the cavity is reduced because of the length of the etch channels.

Type 2 and 3 structures have center [104] and corner etching holes on the diaphragm, respectively. A range of hole sizes (2–16 μm) and numbers (1,2,6) have been included in our design. Such etching hole structures do not occupy extra space in addition to the diaphragm. However, deposition inside cavities will be much more pronounced compared with type–1 structures.

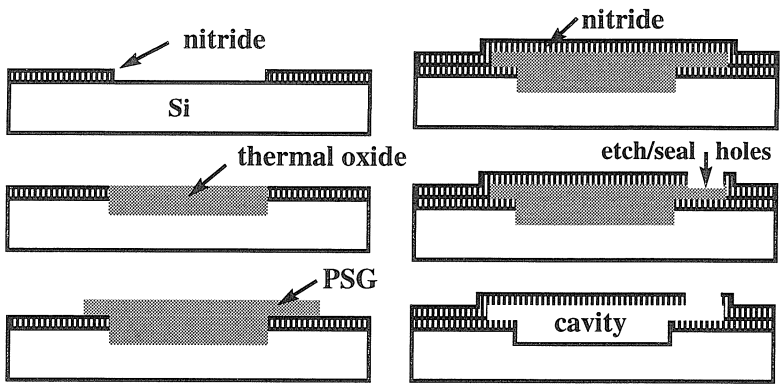

Figure 4-3: Major fabrication steps for micro cavity structures.

Type-4 structures have one to four side openings, 120 or 180 μm long; they are studied here because the side opening can facilitate chemicals' (or gas products') access to the cavity during sacrificial layer or silicon etching; the cavity etch speed can be drastically increased.

All the test structures are fabricated in one process shown in Fig. 4-17, which is similar to the process steps 1 through 5 used for making shear stress sensors (section 2.2.2).

4.1.4 Experiments and Results

Definition of terms

Many sequential depositions with an incremental thickness (30–60 nm) of CVD materials, including LPCVD silicon nitride, LPCVD polysilicon, LPCVD PSG, and PECVD silicon nitride, are performed to seal the cavities (deposition parameters listed in Table 4.1). The way to characterize the sealing performance is to exam each and every test structure under an optical microscope after interval depositions. Since the diaphragm over a sealed cavity will be deformed by the differential pressure between the atmosphere and the cavity interior, interference patterns (Newton ring) can be observed on the diaphragm. The presence of the Newton Ring is thus used as an

Material	flow ratio	pressure(mTorr)	temp.(°C)/power(W)
LPCVD nitride	NH_3/DCS~3/1	330	820/ N.A.
LPCVD Polysilicon	Silane(SiH4)	220	620/N.A.
LPCVD PSG	$O_2/SiH_4/PH_3$ ~6:1:2	150	450/N.A.
PECVD nitride	NH_3/SiH_4~7:3	400	300/50

Table 4.1: CVD processing parameters for various sealing materials.

indication of complete sealing. Pictures of sealed and unsealed structures are shown in Fig. 4-4. After each sealing deposition, the quantity of successfully sealed cavities is counted and used to statistically evaluate the degree of sealing completeness. These data points are then compared between sealing materials, deposition thickness, cavity geometry and channel heights.

To quantify the sealing results of a specific structure at a cumulative deposition thickness, the *sealing factor*, *SF*, is defined as the ratio between the number of sealed cavities and the total number of the cavities of its kind (48, in our case); an *SF* of 1 means that all 48 cavities are sealed.

Also defined is an unit-less thickness t_n the cumulative deposition thickness normalized by the original gap height. The $t_{n,min}$ then is the minimum t_n that is required to seal a cavity with a wafer-level *SF* larger than 0.95. Experimentally, it is only possible to deposit sealing materials at selective finite thickness increment (30–60 nm) and study sealing performance after the wafer is extracted from the deposition chamber. There is an inherent degree of uncertainly associated with $t_{n,min}$ measurement.

Focus of studies – Type-1 structures

Experimental results show that type 1 structures have been successfully sealed by all the deposition materials at certain t_n's, whereas some structures of types 2, 3 and 4 can not be sealed by certain materials within reasonable deposition thickness range. As type-1 structures provide a larger and more complete data base compared with other types they are thus the emphasis of our sealing data analysis.

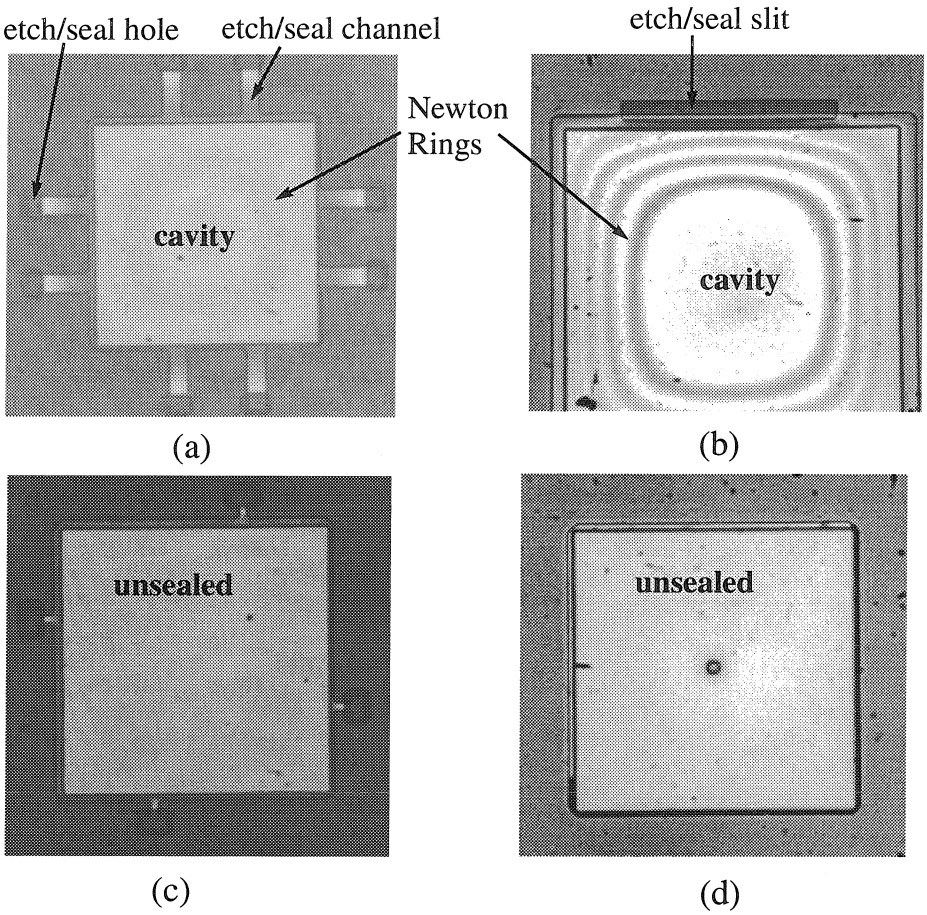

Figure 4-4: Optical photographs of some test structures: (a) A sealed type-1 structure; (b) a sealed type-4 structure; (c) an unsealed type-1 structure; (d) an unsealed type-2 structure.

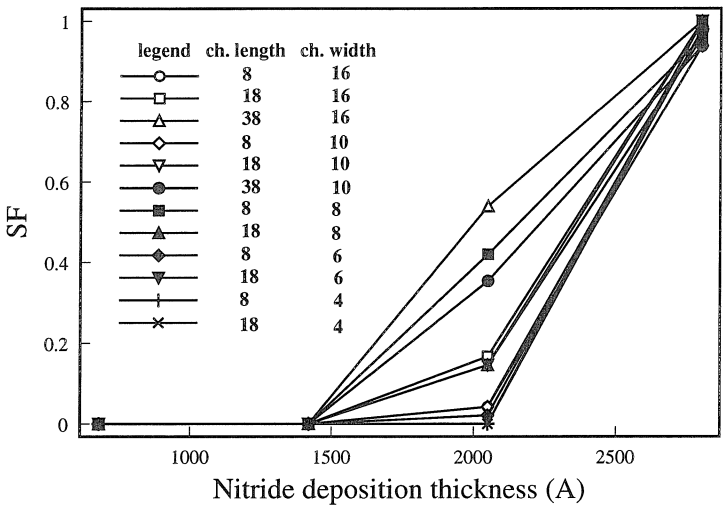

Figure 4-5: Sealing Factor (*SF*) as a function of the deposition thickness of LPCVD silicon nitride.

Material effects

Deposited materials greatly influence the sealing results. The material effects are studied by concentrating on data analysis of type-1 structures. For example, Fig. 4-5, Fig. 4-6 and Fig. 4-7 show the *SF* vs. deposition thickness for LPCVD silicon nitride, polysilicon and PSG, respectively. Each figure provides information for 12 type-1 cavities, all having 8 channels with the same 420 nm gap height but different lengths and widths. One can clearly see that for each LPCVD material, there is a t_n value (0.338 for nitride, 0.173 for polysilicon, and 1.86 for PSG) that any smaller t_n will not seal the structures at all. On the other hand, there is another value (0.67 for nitride, 0.62 for polysilicon, and 4.52 for PSG) that any larger t_n will seal the structures completely. Any t_n between these two values will have partial seal of the structures.

Due to geometric variations, *SF* data points scatter; therefore, we compare sealing data obtained from a fixed structure to study material effects. In our case, all data points are obtained for a structure with 8 channels, each 18 μm long and 4 μm wide. Fig. 4-8 is partly extracted from Figs. 4-5, 4-6, 4-7 and, with the addition of PECVD sealing data points, shows comparison of sealing results using four different CVD

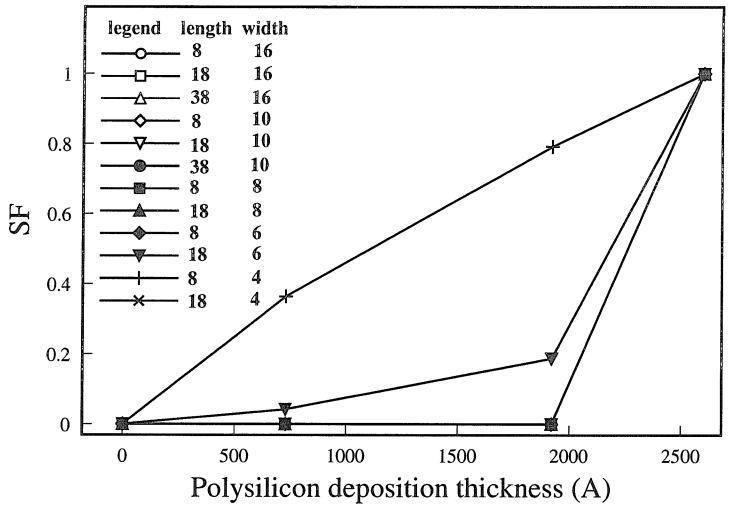

Figure 4-6: Sealing Factor (*SF*) as a function of the deposition thickness of LPCVD poly-crystalline silicon.

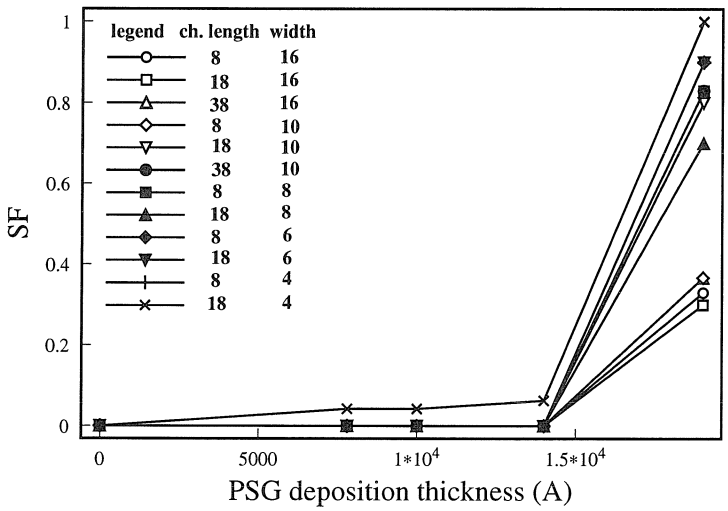

Figure 4-7: Sealing Factor (*SF*) as a function of the deposition thickness of LPCVD PSG.

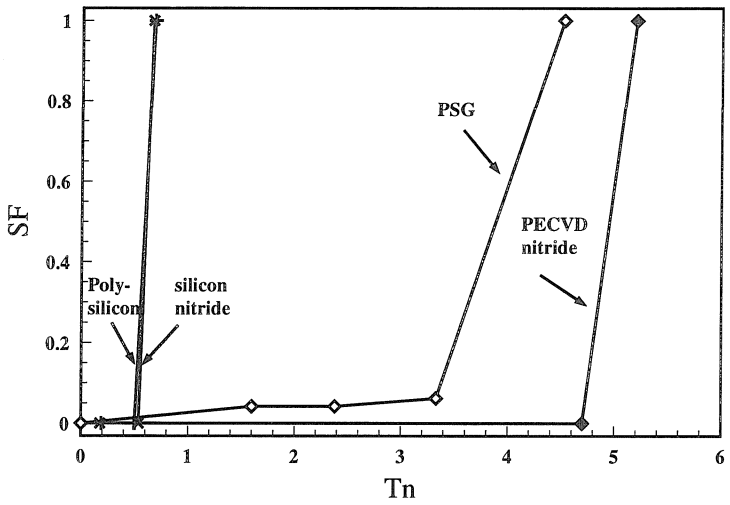

Figure 4-8: *SF* vs. *Tn* plots for different sealing materials: LPCVD silicon nitride, LPCVD Polysilicon, LPCVD PSG and PECVD nitride. Type-1 test structures with eight etching channels, each 18 μm long and 4 μm wide, are studied. The etching channel height is 420 nm.

materials. It is found that $t_{n,min}$ is about 5.2 for PECVD nitride, 4.5 for LPCVD PSG, 0.67 for LPCVD nitride and 0.62 for LPCVD polysilicon. Clearly, LPCVD polysilicon and nitride require the thinnest deposition to seal the structure; these are the most efficient sealing materials. On the other hand, although thicker deposition is required, PECVD methods have the advantage of sealing at a much lower temperature about 300°C.

Gap-height effects

For each sealing material, it is important to find out whether $t_{n,min}$ obtained at one gap height can be applied to various other heights. Extra wafers with different gap heights (520 nm, 743 nm, and 1.01 μm) are prepared, and sealing tests are performed on those wafers by incremental LPCVD silicon-nitride deposition. Fig. 4-9 shows the results of $t_{n,min}$ vs. gap heights; $t_{n,min}$'s are 0.57±0.08, 0.347±0.03, 0.449±0.04 and 0.44±0.03 for the four gap heights studied. Taken into account of experimental errors, the trend shows that $t_{n,min}$ converges to a constant value of approximately 0.44 for

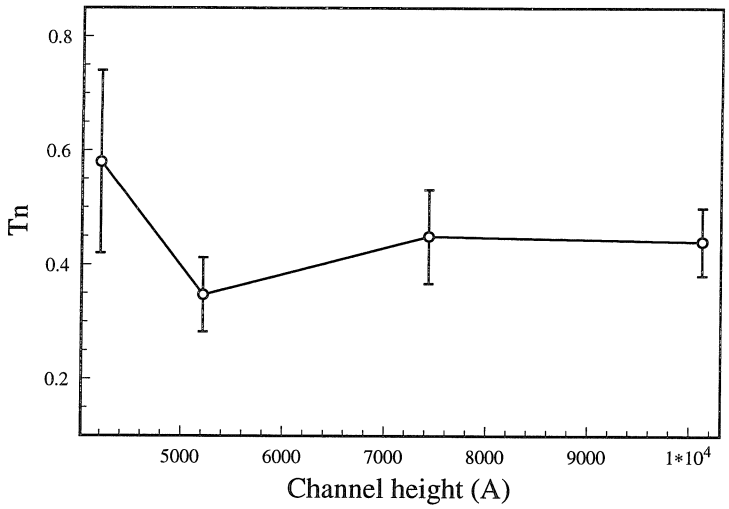

Figure 4-9: Values of $t_{n,min}$ at various channel heights (420nm, 520 nm, 743 nm and 1.01 μm) using LPCVD silicon nitride sealing.

larger gaps. Since the incremental deposition thickness is finite, the error in $t_{n,min}$ is thus large for small gap height and small for large gap heights.

Currently, gap height effects for other materials are not available for various reasons. For example, in the case of LPCVD PSG, thick PSG tends to fracture when the film is over 4 μm. In another case, LPCVD polysilicon becomes opaque when its thickness exceeds 300 nm and making identification of sealed structures by Newton rings impossible.

Geometric effects

For type-1 structures, it is also found through our experiments that geometry could affect the sealing significantly. In fact, different materials have totally different effects. To study geometric effects, we compared sealing data of various sized type-1 structures at a fixed material deposition thickness. Fig. 4-12, 4-10 and 4-11 plots *SF* vs. channel length with widths ranging from 4–16 μm using thickness of LPCVD silicon nitride, polysilicon and PSG, respectively. For LPCVD silicon nitride (t_n = 0.49), Fig. 4-12 shows the trend that longer and wider channels can be sealed with higher

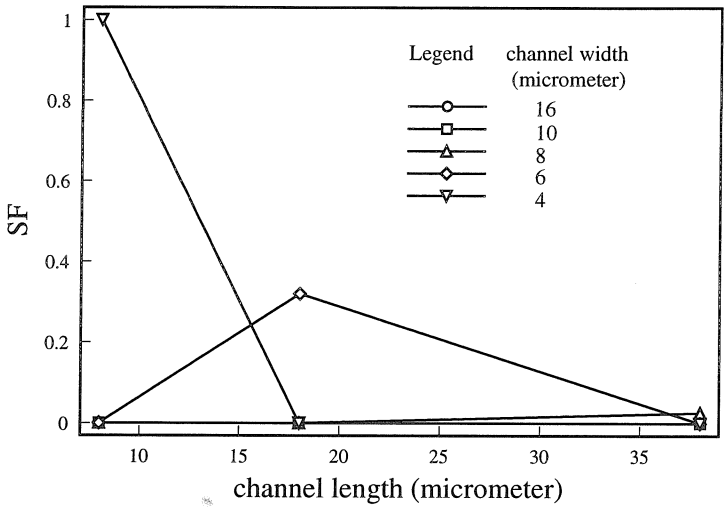

Figure 4-10: *SF* as a function of channel heights and widths for LPCVD polycrystalline silicon.

material	length	width	SF
LPCVD Nitride	↑	↑	↑
LPCVD Polysilicon	↓	↓	↑
LPCVD PSG	—	↓	↑

Table 4.2: For type-1 sealing structures, trends of geometries toward good sealing result.

sealing percentage. For LPCVD polysilicon($t_n = 0.45$), however, Fig. 4-10 suggests that shorter and narrower channels have a higher *SF* although this trend is not as conclusive as in the silicon nitride case because of limited data points. As for LPCVD PSG ($t_n = 4.5$), the narrower the channels, the better *SF* (Fig. 4-11). Channel length has little effect. As a whole, the trends of the geometric effects of sealing type-1 structures are summarized in Table 4.2.

Sealing of Types 2, 3 and 4 Structures

In our work, geometric effects on sealing types 2, 3 and 4 structures were also studied using samples of a fixed height. Conceptually, type-2 cavities require much thicker deposition to seal than structures of other types because of the large gap height, which

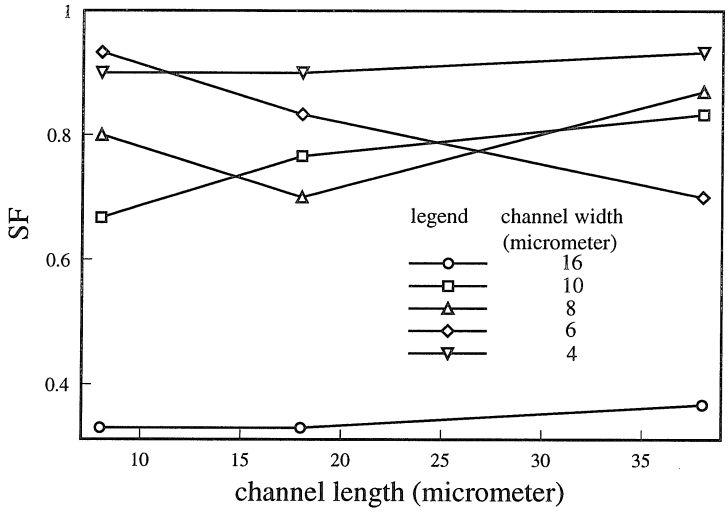

Figure 4-11: *SF* as a function of channel heights and widths for LPCVD PSG.

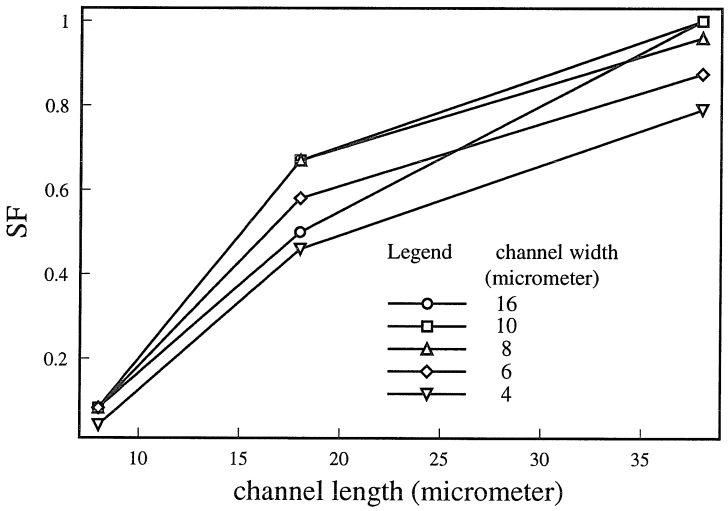

Figure 4-12: *SF* as a function of channel heights and widths for LPCVD silicon nitride.

	TYPE 2	TYPE 3	TYPE 4
LPCVD nitride	poor	good	good
LPCVD polysilicon	poor	good	good
LPCVD PSG	na	good	na

Table 4.3: For types 2, 3 and 4 sealing test structures, general sealing performance by the three LPCVD materials. *na* indicates that conclusive experimental results have not been found.

is 1.3 μm thick thermal oxide plus PSG thickness. This has been confirmed using nitride and polysilicon. Type-3 structures show excellent sealing quality using all three LPCVD sealing materials. Compared with type-1 structures, type-3 structures have identical gap heights and thus comparable sealing performance; *SF*'s for all type-3 structures exceed 0.95 at t_n's of 0.67 (for silicon nitride), 0.62 (for polysilicon) and 4.5 (for PSG). As for type-4 structures, only cavities with one side opened survive the fabrication process for sealing analysis; cavities with more side openings tend to stick to the bottom. For a type-4 structure with one side opening 120 μm long (60 % of the cavity side length), *SF*'s of greater than 0.95 are achieved at a t_n of 0.67 for nitride and a t_n of 0.62 for polysilicon deposition. The general trends of sealing types 2, 3 and 4 structures are summarized in Table 4.3.

Sealing profile

Sealing qualities of cavities should be related to the step coverage of the CVD materials. Various studies on step coverage, both experimentally [130, 22] and theoretically [51], have been done in the past. It has been concluded that step coverage depends on three major mechanisms: direct transport, re-emission, and surface diffusion [22].

Conceptually, knowledge on the step coverage of various materials in an etch hole or etch channel [130, 22, 51] should help to understand the material and geometric effects of sealing. In order to study the sealing mechanisms, a scanning electron microscope

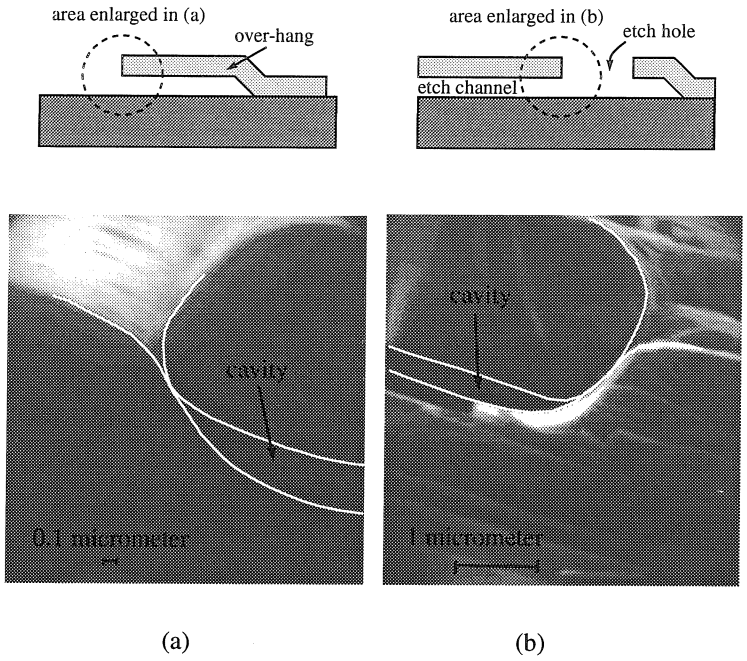

Figure 4-13: SEM photographs of the sealing profile after approximately 1.9 μm of PSG deposition. (a) A specially designed over-hanging test structure; (b) an etch/seal hole of a type-1 structure. The gap height is 4200 Å.

is used to view the cross-section at cleaved sealing holes. The profiles of the deposited material is shown in Fig. 4-13: (a) shows the profile near a test structure while (b) is at a etch hole. These photos confirm that, for PSG sealing, deposition inside the cavity is minimal compared to the deposition on the front of the wafer; it agrees with the conclusion of Cheng *et. al.* [22] that surface diffusion is not a strong factor in LPCVD PSG step coverage. Currently, study on sealing profiles of nitride-sealed and polysilicon-sealed samples is underway.

4.1.5 Summary and Future Work

The sealing of micromachined cavities using chemical vapor deposition techniques is systematically studied for the first time. Results from this study are fundamentally important addition to surface-micromachining knowledge; these are used here to guide

shear-stress sensor design and fabrication.

We have fabricated test structures and studied the sealing of four types of surface-micromachined cavities using LPCVD nitride, polysilicon, PSG, and PECVD nitride. Among all tested materials, LPCVD nitride and polysilicon provide the most effective sealing. LPCVD PSG and PECVD nitride require higher $t_{n,min}$ to seal but offer the advantage of low temperature processing. Using LPCVD nitride as the sealing material, $t_{n,min}$ almost remains constant (0.44) for different gap heights. Qualitative geometric effects have also been studied for type-1 structures; the results point out geometric trends for designing cavity structures that are easy to seal. Sealing results for types 2, 3 and 4 structures are briefly discussed; cavity structures and materials that could produce good sealing results are identified.

4.2 Magnetic-Levitation Assisted Drying of Surface Micromachined Structures

4.2.1 Introduction

Surface micromachined polysilicon or silicon nitride cantilever-type micro structures (e.g., comb drives, micro flaps) are widely used with either LTO or PSG as the sacrificial layer. Usually the distance between these micro structures and the substrate (most commonly silicon) is small (several μm) and the structures are compliant (spring constant < 1 N/m); they can be easily damaged during the drying of liquid after a wet sacrificial etch. During the drying process, when the liquid over the top of a micro structure is removed, the structure will be drawn close to, and sometimes into contact with, the substrate by a surface-tension force exerted from the liquid trapped underneath. Micro structures and the substrate can permanently bond together (*stiction*) and this damage is not reversible. The stiction mechanism

has been studied [39, 80, 67, 4, 1] and solutions have been explored in several major fronts. First, certain chemical treatments of the structures can alter the surface-layer composition [4, 50] and minimize the chance of forming chemical bonds. Secondly, liquid-vapor phase transformation, which is the cause of the surface-tension force, can be replaced by a solid-vapor phase transformation (sublimation) after freezing the liquid [39, 86, 114, 50]. Third, micro structures can be kept away from the substrate by solid organic polymer columns which can be dry-removed (e.g., using plasma etching) after the drying process [81, 89]. Other novel techniques include using special anti-stiction geometry [1], applying pulsed magnetic forces to relieve stuck structures [33] and reducing surface contact area by roughening the substrate surface [134].

In the above-mentioned approaches, surface micro structures remain parallel to the substrate during drying. In our new process, however, these structures are lifted away from the substrate level by magnetic forces before drying starts; the same magnetic force holds micro structures away from the substrate against surface tension forces (Fig. 4-14) throughout the drying procedure. Stiction is not possible simply because the micro structures and the substrate never touch. To realize this, a strip of magnetic material (e.g. electroplated Permalloy, Fig. 4-14a) is located on top of each individual micro structure and activated with an external magnetic field; the interaction between the magnetic moment developed within the strip and the field cause a micro structure (current one-side clamped cantilever type) to bend out of plane. As will be shown, this high-yield drying method is not sensitive to the release chemistry and does not require any complicated drying apparatus (e.g., a pressure/temperature cycling chamber used in sublimation drying).

4.2.2 Theory

To calculate the exact surface-tension force on the test structure would require complex analysis; however, a reasonable upper-bound estimate can be derived. Assuming

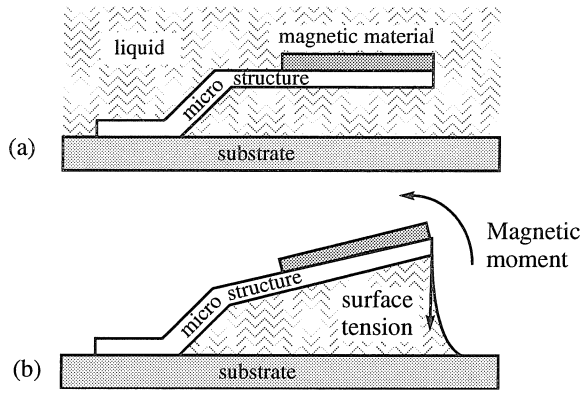

Figure 4-14: Schematic diagram of the magnetic-levitation-assisted drying process. (a) A test structure is immersed in liquid; (b) the structure is lifted by a magnetic moment.

the test structure is parallel to the substrate, the overall torque due to the surface tension (M_{st}) at the free ends of the cantilever beams is

$$M_{st} = (WL + \frac{1}{2}L^2)\gamma \tag{4.2}$$

where $W = L$=1 mm and γ is the surface-tension of a specific liquid. M_{st} will be reduced when the micro structure is raised to an angle. The torque produced by the magnetic force, M_m, can be expressed as [69]

$$M_m = M_s WLtH = M_s VH \tag{4.3}$$

where M_s (=1.35 T) is the saturation magnetization of the magnetic material and V is the volume of the magnetic plate. For the drying process to be successful, $\underline{M_s > M_{st}}$. For a given micro structure geometry, both V and H can be pre-determined to meet this condition.

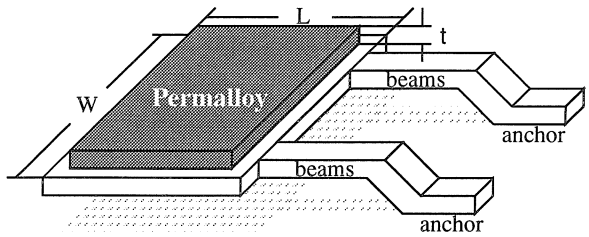

Figure 4-15: Schematic perspective view of a test structure. A magnetic thin film lies over a structural plate which is connected to two cantilever beams. The structural layer is either LPCVD polysilicon or silicon nitride.

4.2.3 Test Structures

A schematic view of our test structure is shown in Fig. 4-15. The structure contains two one-side clamped cantilever beams (400 μm long, 100 μm wide, 2100 nm to 1.5 μm thick) and a 1×1 mm^2 plate attached to the ends of the two beams for lifting them; the large surface area enhances the adverse surface tension effect so the advantages of using magnetic levitation will be clearly demonstrated. A 5 μm -thick electroplated permalloy thin film overlays the plate. Each test die has 256 test structures with different orientations. A fabricated sample is shown in Fig. 3-23. The fabrication process, similar to that used in the permalloy magnetic actuator, is briefly shown in Fig. 4-17. Surface roughness of the substrate and the flap are measured (using an Alphastep 200 machine) as 5 nm.

4.2.4 Experiments

Test structures after the wet release are subjected to four different drying procedures, A, B, A' and B'. All test dies are transferred to de-ionized (DI) water and immersed for 5 minutes. Dies for procedures A and A' are then dipped in various organic chemicals (isopropyl and methyl alcohol, acetone) for 10 minutes while dies for procedures B and B' stay in DI water for an additional 5 minutes.

Fig. 4-18a shows the experimental setup for procedures A and B - dies immersed

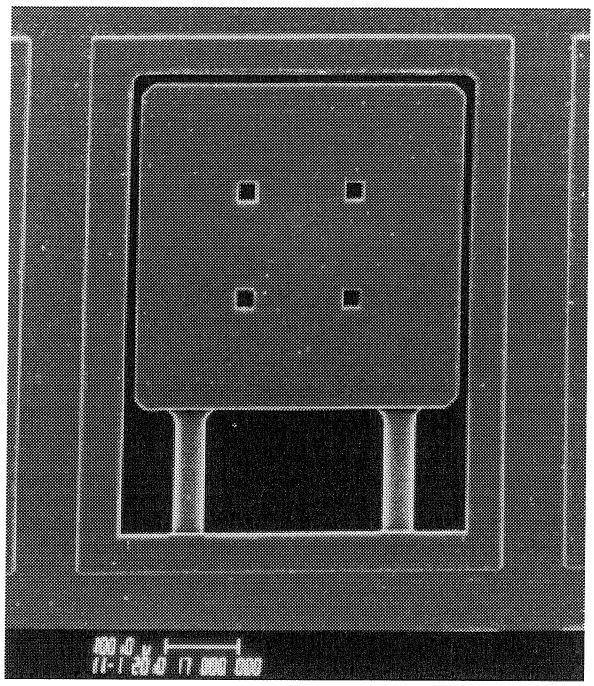

Figure 4-16: An SEM micrograph of the fabricated test structure.

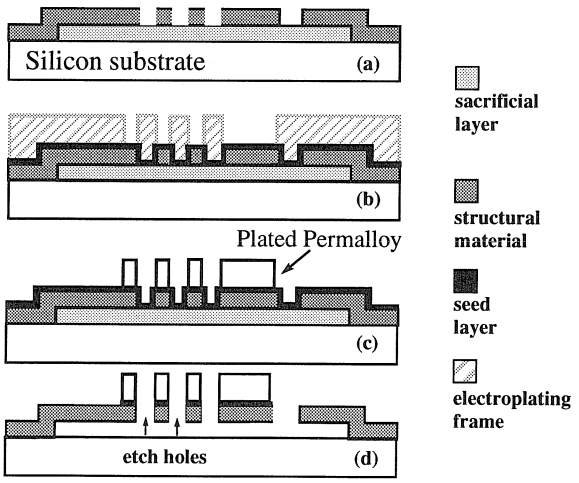

Figure 4-17: Fabrication processes for the test structures. (a) a structural thin-film material (polysilicon or low-stress silicon nitride) is deposited over a 2 μm -thick phosphosilicate glass (PSG) sacrificial layer, patterned and etched; (b) a Cr-Cu composite seed layer is evaporated and a 5 μm -thick photoresist mold is applied and patterned; (c) inside a plating tank, permalloy ($Ni_{80}Fe_{20}$) is electroplated at a rate of 5 μm/hour where the seed layer is exposed; (d) the photoresist and the seed layer are removed and the sacrificial layer is etched with 49 % HF solution.

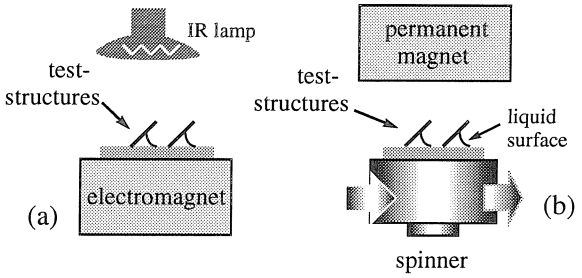

Figure 4-18: The experimental drying sequence (a) in drying procedures A and B, the liquid is vaporized with the heat from an IR lamp; (b) in procedures A' and B', the liquid is spun off the chip while test structures are lifted by an over-hanging magnet.

in liquid are put over an electromagnet and dried with an infra-red lamp under room temperature and pressure. Dies for procedures A' and B', on the other hand, are spin-dried (a time saving method, Fig. 4-18b) - the liquid is spun off the dies (at 500 rpm) while an over-hanging permanent magnet holds up test structures. Drying sessions are video taped; Figure 4-19 is a typical sequence of images showing the side profile of the test structure (lifted by 60°) and the liquid (in diminishing amount from Fig. 4-19a to Fig. 4-19c).

At the room temperature, γ (in N/m) is 0.073, 0.024, 0.0237 and 0.0217 for DI water, methyl and isopropyl alcohol, and acetone, respectively. For procedures A and B, the minimum required external field H_{min} can be determined as a function of γ. Experimentally we determine H_{min} by lowering the electromagnet biasing until a lifted test structure is pulled down by the surface tension force. Theoretical and experimental H_{min} vs. *gamma* data agree well and are shown in Fig. 4-20.

We examine individual micro structures under an optical microscope to determine whether stiction occurs. In evaluating the structural yields of different drying method, four dies (1024 structures) are examined after each drying process and each organic liquid. The yields are 100% for all four procedure and all organic chemical with the magnetic levitation. In comparison, when the magnetic field is not present during drying, 0–10% yield is obtained for procedures A and B, and 0% for procedures A' and B' (consistent with results from other researchers). Polysilicon or silicon nitride

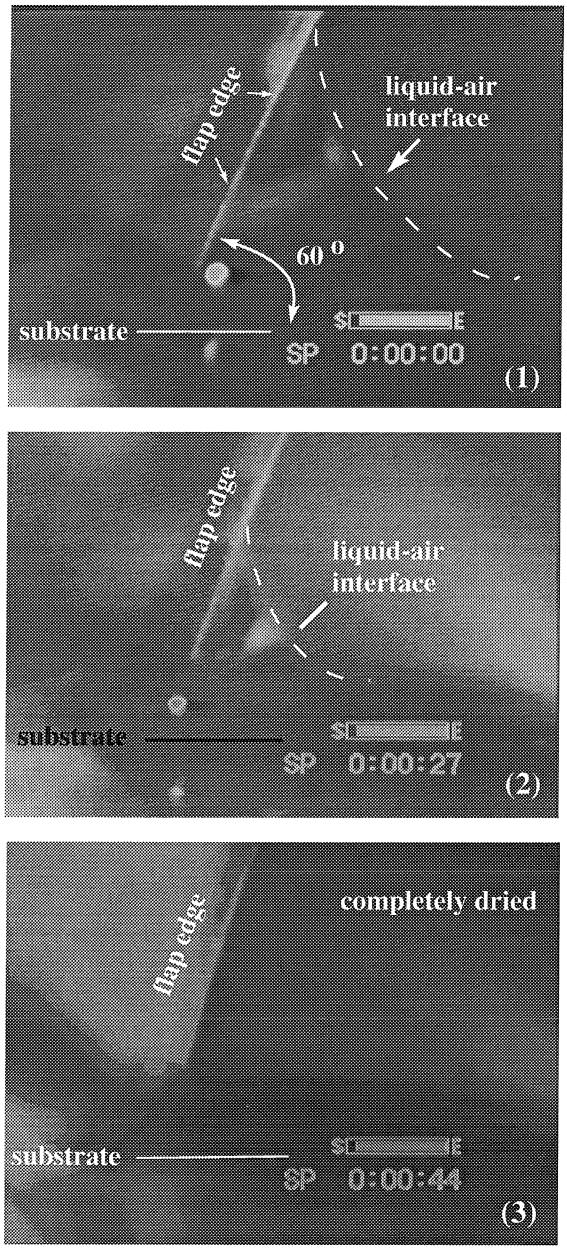

Figure 4-19: A sequence of video images showing the side view of a test structure and the liquid-air interface. The flap was initially lying in the substrate plane, immersed with isopropyl alcohol (not shown). (1) The flap is then lifted with magnetic forces; (2) the dotted line indicate the liquid-air interface. With the IR lamp heating, alcohol gradually vaporized and the amount of liquid trapped under the flap is reduced; (3) alcohol is completely removed.

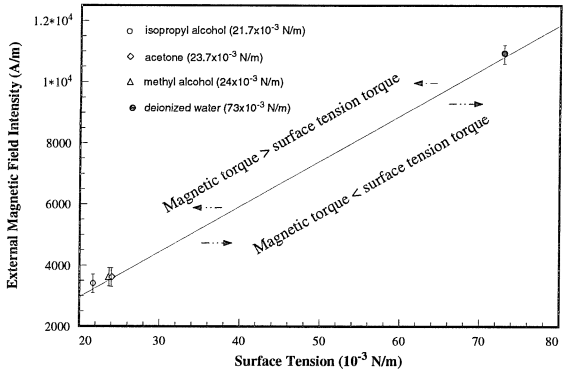

Figure 4-20: Theoretical curve and experiment data points of H_{min} vs. γ for four kinds of liquid (isopropyl and methyl alcohol, acetone and water) used in procedures A and B. For a certain γ, magnetic levitation will occur when $H > H_{min}$.

structures behave almost the same. Test structure thickness does not seem to affect the drying behavior.

4.2.5 Summary and future work

Inspired by the Permalloy magnetic actuator fabrication process (section 3.3.3), this magnetic-levitation-assisted drying process has been proven to produce 100% yield for our test structures with a large surface area. The liquid removal can be completed using IR lamp heating and even spin drying. More systematic experiments with an extended collection of test structures are underway to directly compare our drying result with previously published ones. The possibility of using this method to release many other types of structures (e.g., bridges, diaphragms) is being explored.

Chapter 5

MEMS SYSTEMS FOR FLUID MECHANICS STUDIES

In this chapter, we review two fluid mechanics applications that utilize micromachined sensors and actuators are discussed in Chapters 2 and 3.

5.1 Distributed MEMS for Active Drag Reduction

5.1.1 Motivation

Drag reduction is a subject of great difficulty and reward. Many living species in the natural world (e.g., sharks, dolphins, shells at the bottom of the ocean, cactus in the high-wind desert) have developed structures, organisms and instincts to reduce drag forces [13]. As an example, dolphins, in addition to their stream-lined body shape, relies on compliant skin to damp turbulent motions around its body and therefore reduce skin-friction drag. Drag reduction has always been a subject of active research. Reducing drag results in saving energy and increasing speed. For example, if the drag on airplanes is reduced by a few percent on average, the annual world savings on fuels

would amount to several billion dollars.

5.1.2 Passive Drag Reduction

In an incompressible flow field, drag usually consists of two components: pressure drag and skin friction drag. The pressure drag is created by the flow separation and the skin-friction drag is related to shear-stress over the surface. For a common streamlined body shape, the magnitude of these two drag components are approximately equal. While the pressure drag can be reduced through further streamlining the shape of a body, the skin friction drag is much more difficult to control and minimize.

Previous studies have indicated that there is a strong relation between turbulent skin friction on a wall and stream-wise vortices associated with it. Studies by Kravchenko [64], based on averaged statistics of skin friction and vortices, has further indicated that high skin friction footprints can be attributed to stream-wise vortices, so called quasi deterministic wall structures. However, controlling these stream-wise vortices in an active manner is a difficult subject. The most widely observed coherent vortex structures happen randomly in time and space. According to the analysis in Section 1.2, such wall structures are typically 1000 y^+ long, 100 y^+ apart from each other, 30 y^+ in diameter, and last about several tens of ms.

Most turbulence and drag-reduction control schemes are passive. For example, placing stationary riblets in the boundary layer serves to suppress the formation or interaction of organized flow structures. These devices play only a passive role because there is no feedback loop to sense, and then manipulate, flow structures to maximize the drag reduction benefit. These approaches have severe limitations; for example, the riblets mentioned before would work only for a fixed flow speed [13].

5.1.3 Active Drag Reduction using MEMS

In the past, closed-loop control of the flow structures in a fully turbulent boundary layer was not possible for two reasons. First, the length scale of sensors need to be sub-millimeter to provide the required spatial resolution. Secondly, a large number of the distributed sensors are necessary to capture the spatially and temporally random events.

Studies by analytical modeling and computational analysis have suggested that there is a tremendous potential for reducing skin friction by actively controlling wall structures within the turbulent boundary layer. According to Choi [23], in a fully developed turbulent flow field, control of boundary layers by placing appropriate sensors at the wall and by using effective drag reduction mechanisms can yield a maximum 6% drag reduction. Reduce skin friction drag would require controlling individual wall structures using the information provided by the sensor array. However, these studies do not suggest the physical approach of interacting with the vortex structures.

The emerging MEMS technology offers the opportunity to reduce drag through interactive control of individual flow structures [47]. An ongoing University Research Initiative(URI) project targets drag reduction using a real time micro system which is capable of performing sensing, actuation and real-time computing. Figure 5-1 shows the schematic of the proposed system, which contains integrated micro sensors, micro actuators and micro electronics neural network circuits (M^3 technology). The boundary-layer flow field is monitored by using a large number of distributed sensors; the output signals will be fed to the integrated neural networks which can recognize the sub-layer streaks responsible for most of the drag production. Based on total drag sensor output, the neural networks will use on-chip learning algorithms to drive responsible actuators which, in turn, manipulate the local streaks in an effort to reduce the viscous drag. It is note-worthy that the energy-saving goal also dictates that power consumption to the large arrays of sensors must be minimized.

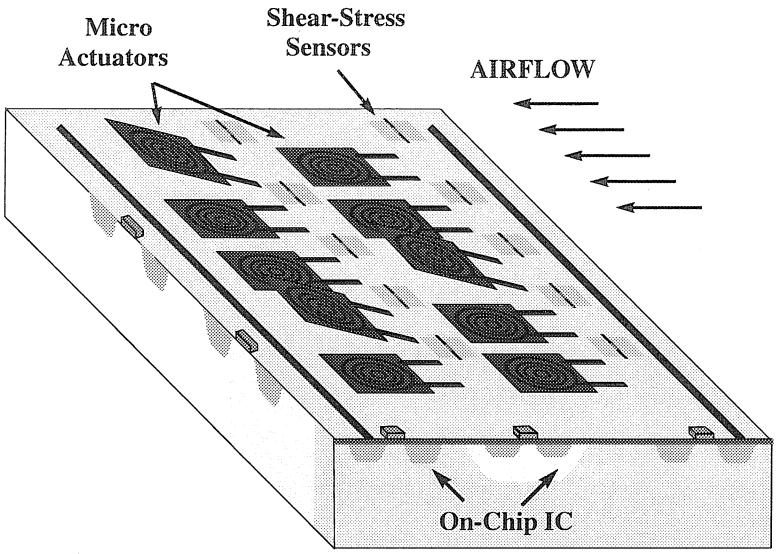

Figure 5-1: Sketch diagram of an M^3 system for active fluid control.

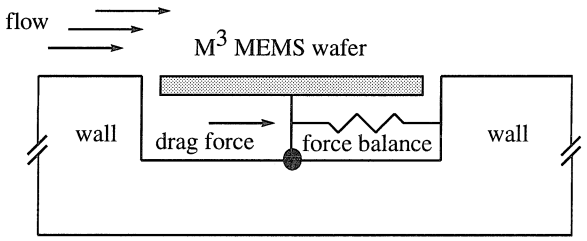

Figure 5-2: Schematic of the system to be used to demonstrate drag reduction using a wafer-level M^3 system.

The goal of the initial active drag reduction studies is to demonstrate a silicon wafer (four-inch diameter for example) that carries an M^3 system on its surface. The wafer, when mounted flush with the bounding wall of a flow field, is connected to a force balance that measures the total drag force (Fig. 5-2). The wafer will experience reduced drag when the wafer-level micro system is powered. The technological approach for integration is to build half-completed CMOS circuitry through a commercial foundry service and then build sensors and actuators at our micromachining facility onto the same wafers.

5.1.4 Overview of Recent Progress

The test wind-tunnel is identical to the one used for shear-stress sensor calibration (section 2.3.1). Sensor and actuator packages are located in the downstream portion of the wind-tunnel where fully developed turbulent flow is assumed.

Mechanical actuators

The interactions between steady stream-wise vortices and a mechanical actuator in a 2-D channel flow have been investigated [124, 125] using a mechanical actuator.

In a two-dimensional channel flow facility, hot-wire wind speed measurement at Re=8583 indicates that the channel consists of a laminar entrance flow and a fully developed turbulent down-stream region which covers about 2/3 of the total length of the wind-tunnel. The flow field associated with a micro-actuator is investigated through a scaled-up model consisting of a vortex generator (VG) and a mechanical actuator.

The VG is 0.05" high, and covers an area of 3.75" $\times$ 1.75". The mechanical actuator oscillates at 12 Hz and travels from the wall to a height of 0.052". Controlled stream-wise vortex is artificially generated by a VG and the flow velocities on planes normal to the mean flow are recorded at successive stream-wise locations downstream.

The velocities are either time- or ensemble- averaged by using the driving signal of the actuator as the phase reference. The result is used to analyze the phase-locked velocity and shear-stress distribution at different phases of the actuator cycle. It has been shown that the oscillatory motion of the mechanical actuator can reduce surface shear-stress.

When an actuator falls from the activated position to the resting position, it also influence the flow field. It has been speculated that the speeds of the rise and fall of the actuator plate will determine the over-all drag-reducing effect of one actuation

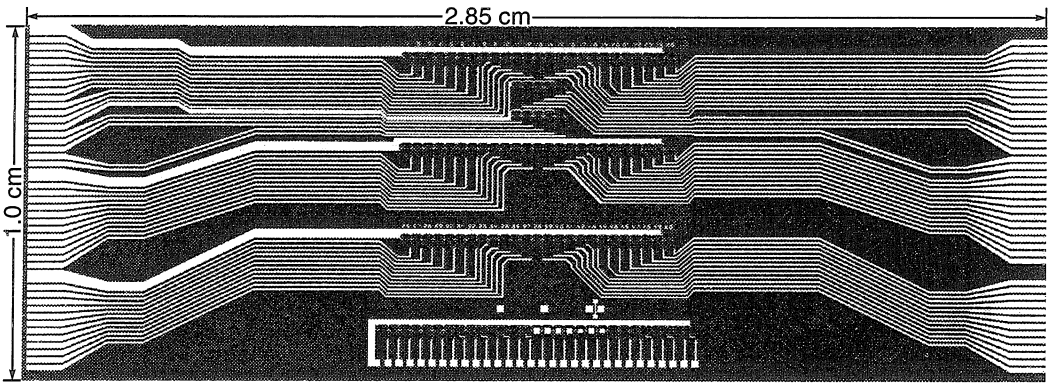

Figure 5-3: Picture of a shear-stress sensing array. Courtesy of Fukang Jiang, Micromachining Laboratory, Caltech.

cycle. This aspect of flow control has been studied using mechanical actuators as well.

Shear-stress sensor array

An array of shear stress sensors have been developed (Fig. 5-3). Sensors are spaced apart by 300 μm in the span-wise direction. The sensor-array chip captures the quasi-two-dimensional shear-stress distribution over a silicon substrate.

As a precursor to full system integration, we have assembled hybrid systems consisting of sensor array, sensor driving circuitry, actuator driving circuitry and a linear array of five air-coil magnetic actuators. The information of two-dimensional shear-stress distribution has been successfully utilized to control individual actuators.

5.2 Delta-wing motion control

5.2.1 Subsonic Aerodynamics of Delta-wing Airfoils

Except for a few aircraft models[1], aircrafts with delta-wing airfoils spend the majority of their flight time at subsonic speeds and use their supersonic capability for short dashes. The subsonic aerodynamics of a delta-wing aircraft has been a subject of research interest [5].

The subsonic flow pattern over the top of a delta wing has prominent features. When laminar flow hits the two leading edges of the wing at a certain angle-of-attack (Fig. 5-4a,b), two counter-rotating leading-edge vortices occur in the vicinity of the highly swept leading edges. These vortex patterns are created by the following mechanism. The pressure on the bottom surface of the wing at the angle of attack is higher than the pressure on the top surface. Thus, the flow on the bottom surface in the vicinity of the leading edge tries to curl around the leading edge from the bottom to the top. This will cause the flow separate from the wing along its entire length (see Chapter 1 for details on flow separation). Two vortex structures formed over the top of the delta-wing are shown in Fig. 5-4c and Fig. 5-5. These vortices are strong and stable. Being a source of high energy and relatively high-vorticity flow, the local static pressure in the vicinity of the vortices is small. The leading edge vortices create strong "suction" forces on the top surface near the leading edges. The total vortex lifting forces on the two sides of the wing contributes ~40 % of the total lifting forces [2]. The strength and position of these two vortices are dependant on the exact separation point of the flow along the perimeter of the leading edge.

[1] Concord supersonic jet, space shuttle, X-31

[2] At an 30° angle-of-attack for 60° swept angle

5.2.2 MEMS Delta-wing Control: Scheme

There were many studies on modifying a delta-wing's control mechanism to achieve aircraft stability at high angle of attack. Leading edge air blowing and suction [36] has been used to substantially retard the onset of wake formation. Vortex flaps and plates [96] try to modify the leading-edge vortices to increase vortex lift while reducing the lift/drag ratio.

Micromachined actuators have traditionally been used to control objects that are also small in scale. We intend to demonstrate that a collection of micro-machined actuators can control a macro object, provided that a proper controlling mechanism exists. In our case, the macro object is a model delta-wing airfoil and micro actuation is provided by a linear array of Permalloy magnetic actuators discussed in Chapter 3. A known aerodynamic effect allows micro-scale actuation to have a macro effect. Delta-wings are one of the fundamental configurations for generating lift forces and its aerodynamic control in the subsonic regime is of great importance to aeronautics applications [36, 96]. Results of our studies can possibly lead to new delta-wing designs featuring greatly enhanced maneuverability.

Two linear arrays of surface micro-machined, out-of-plane actuators (micro-flaps) are placed along two leading edges on the bottom of the wing (Fig. 5-4 d). Actuators are required to achieve a vertical deflection similar to the boundary layer thickness to gain maximum benefit. When un-deflected, flap arrays remain at the bottom of the boundary layer, having no effect on the flow and vortices; when one array is deflected downward, however, it interacts with the boundary layer and changes the separation point of the corresponding leading-edge vortex. The span-wise vortex structures over the top of the wing become unbalanced, and an overall rolling moment can be created.

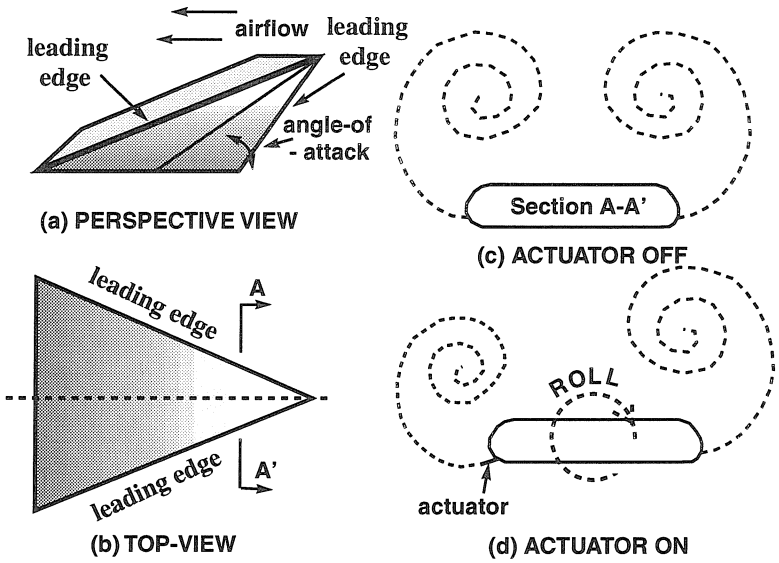

Figure 5-4: Fluid mechanism for delta-wing rolling-motion control. (a) perspective view of a delta-wing in a flow field; (b) top view of the delta-wing; (c) cross-sectional view of the wing and vortex structures when the micro-flaps are off; (d) vortex structures change when the micro-flaps along one leading edge are turned on.

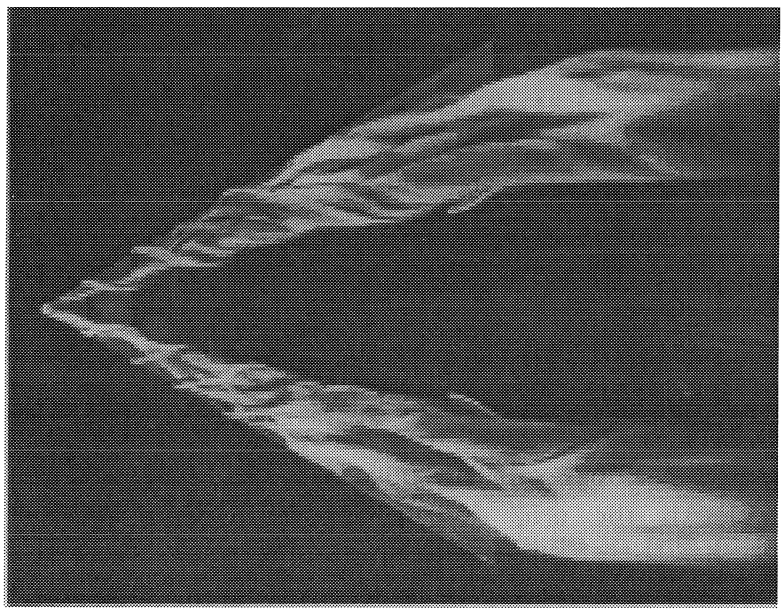

Figure 5-5: Flow visualization of vortex pairs along two leading edges. Courtesy of H. Werlè, ONERA.

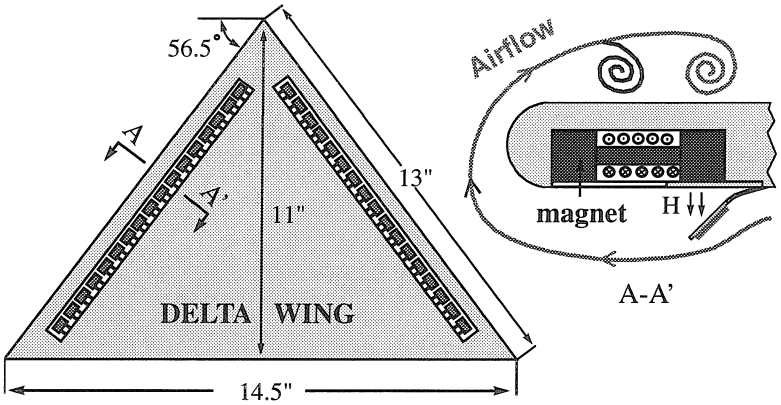

Figure 5-6: A schematic diagram of micromachined actuators installed on a model delta-wing.

5.2.3 Wind-tunnel Tests

Delta-wing/actuator assembly

A scale model of a delta-wing is made of aluminum; it has a span of 38 cm, and a swept angle of 56.5° (Fig. 5-6a). The model has rounded edges with a radius of curvature of approximately 0.5". Two grooves, parallel to the leading edges, are opened on the backside of the delta-wing (Fig. 5-6b). Each groove is approximately 250 mm × 4mm in size, 5 mm away from the leading edge; it holds three groups with a total of 54 electromagnets. Two linear arrays of $\sim$ 100 Permalloy actuators are mounted on top of the electromagnets, flush with the delta-wing surface. A maximum current of 1 A was applied to the buried electromagnets to produce a maximum $H_{ext} = 2.1 \times 10^4$ A/m on the actuator plane.

Flow-separation line detection

One of the leading edges is replaced by a rolling rod. Shear stress sensors fixed on the surface of this rod can be rotated to different angles θ (Fig. 5-7). By rotating the rod and putting the sensor at different locations along the rod, the shear stress (both real-time and time-averaged) at different locations can be obtained. Two methods can be

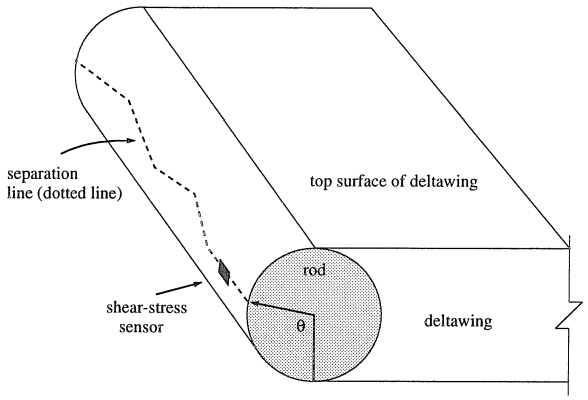

Figure 5-7: Diagram showing the rotation rod on which shear stress sensors are installed along the delta-wing leading edge. The separation line is illustrated (not to scale).

used to detect the separation point. The first method is based on the magnitude of the shear-stress being absolutely zero at the point of separation. A minimum D.C. output of the sensor should correspond to this location. Unfortunately, there is one difficulty in applying this method. Because the flow along the leading edge is three-dimensional instead of two-dimensional, the fundamental assumption that shear stress value is the lowest at the separation point is challenged.

The second separation-detection scheme is based on the fact that the flow fluctuation increases drastically *right after* the separation point. Therefore it is reasonable to measure the root-mean-square value of the shear stress sensor and find the point of sudden change. Experiments indicates that the *rms* value stays low on the lower surface of the wing and jumps to a higher value at a specific θ location. This position is different for different positions along the leading edge; therefore the mapped separation line is not straight, but rather, zig-zagged (Fig. 5-7). At a wind velocity of 15 m/s, the separation points center near 75°; at 20 m/s, flow separation happens near $\theta = 60°$.

Rolling moment control

The wind-tunnel used here is 60 ft long with a cross-sectional area of 3 ft by 3 ft (0.9×0.9 m^2). The test section of the wind-tunnel, together with the installed delta-wing model, is shown in Fig. 5-8. The wing's angle-of-attack is fixed at 30°. The characteristic length, l, used for Reynolds number calculations is the chord length [3] of the delta-wing; l is therefore 11 inch, or 28 cm, in the current situation. At a flow velocity of 10 m/s, for example, Re is equal to approximately 1.8×10^5.

The model delta-wing is mounted on a six-component force balance (AMTI Co.) that records rolling moments and forces in three axis (Fig. 5-9). Initially, time-averaged (four minute) measurements of the rolling moment (M_{roll}) were taken with the actuator plates deflected. The resulting M_{roll} at different wind-tunnel flow speeds is normalized with respect to the vortex lift moment, M_{vl}. Here, M_{vl} is the product of the vortex-lift force on one of the leading edges multiplied by the distance between the point-of-action and the delta-wing's central axis. To ensure that the measured M_{roll} is indeed generated by the actuation action and is not an artifact of signal drift, we then monitored the real-time M_{roll} changes by turning on and off one actuator array at approximately 1 Hz. The force-balance rolling-moment signals are shown in Fig. 5-10, for the two cases when the actuators are at rest position and when they are deflected; a clear difference of signal levels is observed. Very repeatable data of the M_{roll}/M_{vl} at various flow speeds are obtained (Fig. 5-11); the maximum is 1.2% at mean flow speed of 16 m/s. Note that the locations of actuators are not according to the separation-line positions; rather, two linear arrays of actuators are on the bottom surface immediately before the leading-edge curvature.

Further, it is confirmed experimentally that as the actuators are positioned on the leading-edge curvature and before the separation line, more significant rolling moment can be created. In one test, as much as 10% time-averaged M_{roll}/M_{vl} is achieved (flow

[3] The distance from the apex to the middle of the trailing edge.

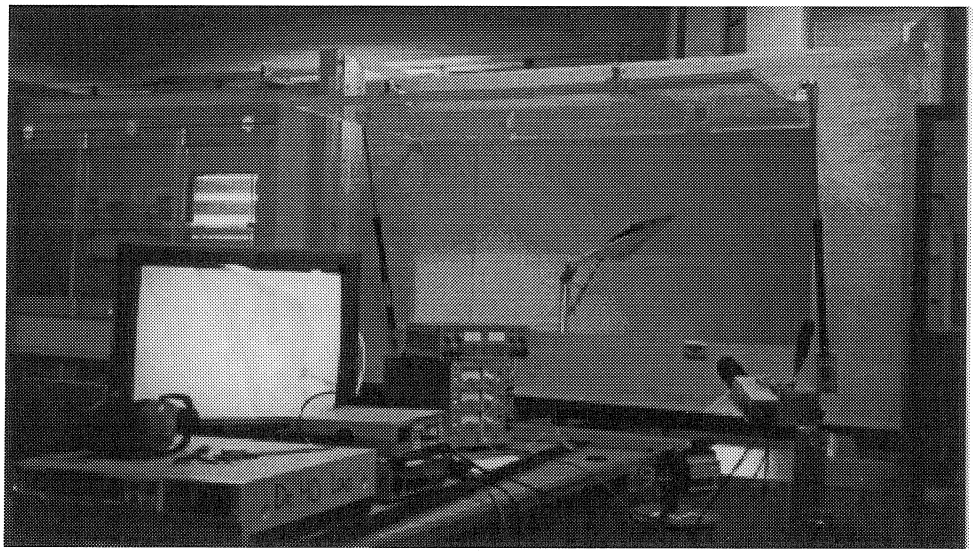

Figure 5-8: A view of the wind-tunnel used for delta-wing testings and supplementary equipment.

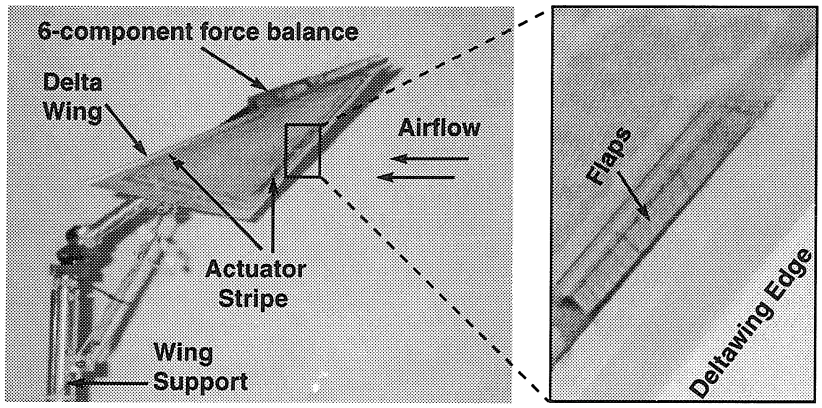

Figure 5-9: A delta-wing model mounted on a six-degree-of-freedom force gauge inside a wind-tunnel.

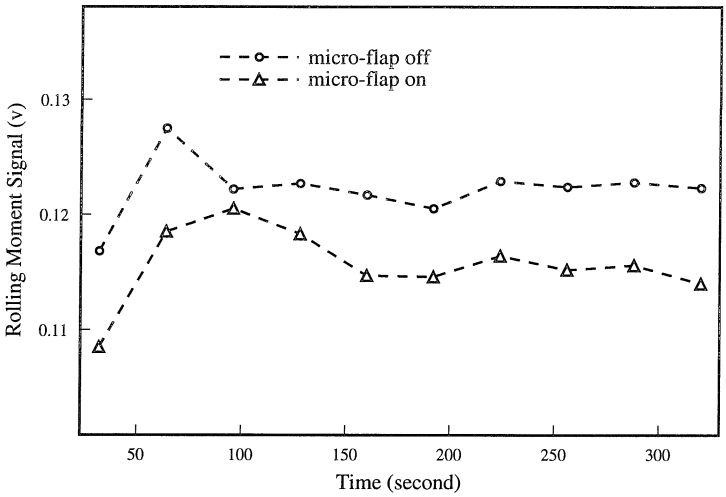

Figure 5-10: Real-time force-balance rolling-moment output signal comparisons when the actuators are on and off.

speed=16 m/s). If the same percentage controlling capability is applied to a delta-wing F-15 fighter, a M_{roll} of 4×10^4 N-m could be generated, enough to turn the fighter 360 ° in $\sim$ 1 second. It is also expected that as the flow speed increases, the rolling moment could become more significant.

However, as the actuators are positioned closer to the separation lines, flow conditions become more violent. In addition, local flow velocities are not exactly perpendicular to the leading edges. It has been found that a large portion (approximately 60%) of actuators are damaged; they fail not due to excessive bending, but due to twisting moments.

5.3 Summary and Future Work

The developed shear-stress sensors have been used in a MEMS system for active drag reduction; they have also been successfully implemented on the leading edges of a model delta-wing to determine the flow separation points. The Permalloy magnetic actuators have been applied for delta-wing control; control theory is proven by

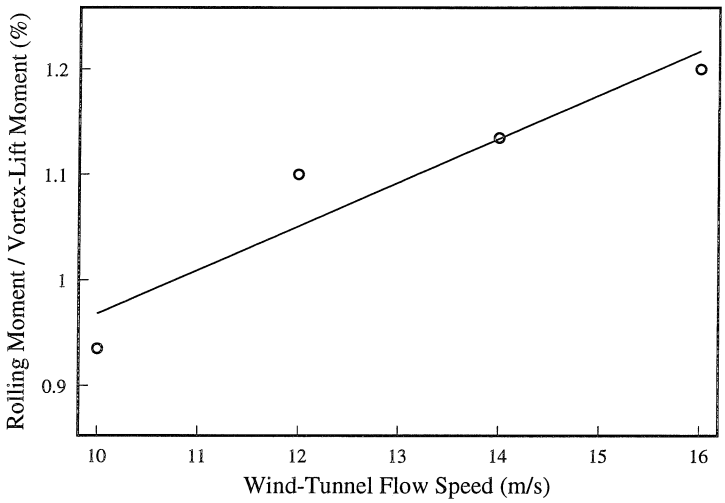

Figure 5-11: M_r/M_{vl} generated by the actuation of one linear actuator array as a function of the average wind tunnel flow speed. $H_{ext} = 2.1 \times 10^4$ A/m.

experimental results.

In terms of the delta-wing control project, research focus in the near future include developing more robust micro actuators. Besides, air flow around the leading edge is strong and more adverse to the micromachined actuators than when these actuators are placed on the side wall of a wind-tunnel. We have also discovered that operating the existing micro actuators directly on the leading edge is difficult, because the flow is faster and more turbulent than the flow on the bottom of the delta-wing. The wind loading prevents actuators from deflecting out-of-plane and the turbulent flow field damages a large percentage of these actuators. Second-generation flaps are currently being designed and fabricated; the new actuators will be more flexible yet more robust, and allows for even-stronger permalloy/magnetic field interaction.

Chapter 6

CONCLUSION

The focus of this thesis is the development of silicon micromachined sensor and actuator arrays, and system studies on micro fabrication methods used for fabricating these devices. These micromachined devices are used in fluid-mechanics applications with success. Major achievements of the thesis studies are summarized in the following.

We have successfully developed a flow shear-stress sensor with a unique vacuum-cavity thermal isolation micro structure (Chapter2); improved thermal-isolation effects have been experimentally proven. Shear-stress sensitivity that is much higher than previously developed sensors (micromachined or conventional) has been demonstrated. We have conducted sensor calibration in a two-dimensional channel flow. This sensory device has been used in two applications, one for detecting coherent wall (flow) structures and another for determining flow separation points.

Two types of magnetic actuators are explored. The air-coil actuator is our first effort (Section 3.2). Magnetic actuation has been demonstrated; however, the performance of this actuator is limited by the bending created by intrinsic stress and thermal-induced stress. Our second magnetic actuator utilizes the interaction between Permalloy material and the external magnetic field (Section 3.3). The magnetic actuation has been characterized; this actuator has achieved stronger force and larger displacement compared to the air-coil type. Air-coil magnetic actuators have been

successfully applied in the project for active drag reduction. The Permalloy magnetic actuators, on the other hand, have been implemented to achieve delta-wing control.

The whole micromachining field can benefit from studies of fundamental micro fabrication issues. In this thesis work, two issues are explored and new findings are revealed. First, the behavior of micro cavity sealing using LPCVD materials is studied systematically for the first time(Section 4.1). We have gained understanding on how sealing efficiency is affected by the sealing material, cavity geometry and deposition thickness; these knowledge will facilitate the micromachining design and processes in the future. The second micro-fabrication issue involves devising a new surface-structure release/drying method (Section 4.2). Magnetic levitation is utilizes to counteract the surface tension forces that tend to pull down surface structures to the substrate.

Most recent progress on the two fluid-mechanics projects are discussed in this thesis (Chapter 5). In the project for realizing active drag reduction, individual components including sensors, actuators and circuit have been successfully tested individually. The next step involves assembling these tested components into a hybrid and then integrated systems and demonstrate their functionality. In the project for delta-wing control, flow separation-line detection has been achieved with shear-stress sensors and up to several percent of rolling-moment control has been realized with micromachined actuators. Actuators that are more robust to turbulent flow conditions are being developed; these can further enhance the wing control.

A

Description of Selected Micro Fabrication Steps

The detailed fabrication processes are described in this appendix.

1. **Standard wafer cleaning - remove organic residue**

   Starts with Piranha (H_2O_2 and concentrated H_2SO_4 mixture);

   Add 400 ml of fresh H_2O_2 into Piranha solution;

   Pre-heat to 120 °C;

   Immerse wafers into Piranha for 10 minutes (or longer if necessary);

   Rinse wafers in DI water bath 1 ("dirtiest");

   Remove native oxide using 5 % HF solution if necessary;

   Rinse wafers in DI water bath 2;

   Deep rinse wafers in DI water bath 3 ("cleanest") while monitoring resistivity;

   Dry wafers after the resistivity is higher than 10 MΩ-cm ;

   Spin dry wafers.

2. **Standard photolithography**

   wafer clean; convection over bake;

   HMDS (Hexamethyl Disilanzane) vapor priming 2 minutes for adhesion promotion between the spin-on photoresist layer and the substrate (priming for too long a time will not further enhance adhesion);

Spin-on photoresist (four types depending the thickness and step coverage requirements):

type 1: KTI photoresist 105 CS, spin at 3 krpm, $\Rightarrow$ 2.7 μm ;

type 2: KTI photoresist 27 CS, spin at 3 krpm, $\Rightarrow$ 2 μm ;

type 3: AZ photoresist 4400, spin at 4 krpm, $\Rightarrow$ 4 μm ;

type 4: AZ photoresist 4620 CS, spin at 4 krpm, $\Rightarrow$ 6.2 μm ;

Soft-bake photoresist in a convection oven at 100°C for 15 - 25 minutes;

Expose wafer using GCA stepper (10:1 reduction);

Develop wafer in corresponding photoresist developer; rinse;

Hard back photoresist at 110 – 120°C.

3. **LPCVD low-stress silicon nitride**

chemical reaction: $3SiCl_2H_2 + 4\ NH_4 \longrightarrow Si_3N_4 + 6\ HCl + 6\ H_2$ (stoichiometric).

flow rates: $SiCl_2H_2$ / NH_3 = 67.2 sccm / 15.6 sccm $\approx$ 4:1

base pressure: 58 mtorr

deposition pressure: 245 mtorr

deposition temperature: 825°C

deposition rate: 60 Å /minute

4. **LPCVD polycrystalline silicon**

chemical reaction: SiH_4 (vapor) $\longrightarrow$ Si (solid) + 2 H_2 (gas)

flow rates: SiH_4=80 sccm

base pressure: 10 mtorr

deposition pressure: 200 mtorr

deposition temperature: 560–580 °C : amorphous; above 600 °C :crystallized

deposition rate: 40–160 Å /minute (depending on deposition temperature)

5. **LPCVD phosposilicate glass**

chemical reaction: $SiH_4+O_2 \longrightarrow SiO_2 + 2\ H_2$

flow rates: Oxygen 130 sccm, SiH_4 65 sccm, PH_3 between 5 to 10 sccm.

base pressure: 20 mtorr

deposition pressure: 150 mtorr

deposition temperature: 450 °C

deposition rate: 100 Å /minute

6. **Wet thermal oxidation**

chemical reaction: $Si + O_2 \longrightarrow SiO_2$

oxygen flow rates: less than 0.5 sccm (only serves to transport water vapor)

water input rate: 1 drop of water/5 seconds

reaction temperature: 900 - 1100 °C

oxidation rates:

1050 °C , at (35 min., 120 min. and 300 min.) intervals, thickness are (4200 Å , 9450 Å and 14400 Å), respectively.

950 °C , deposition rate is linear up to at least 90 min. – 50 Å /min.

7. **Ion implantation and annealing**

Phosphorus doping with a dose of $1 \times 10^{16}/cm^2$ at 40 keV energy;

Annealed in annealing furnace, nitrogen ambient, 1000 °C for 1 hour.

8. **Plasma etch**

gas source: SF6, SF6+O2, O2 (for photoresist de-scum)

typical pressure: 200-300 mtorr

typical power: 300 W

9. **Reactive Ion etch**

flow rates: oxygen: SF6 = 3 sccm: 17 sccm

power input: 600 W

etch rate on LPCVD silicon nitride: 700 Å /min.

B

Glossary

Symbol	Name	Definition	Units
Fluid Mechanics			
Re	Reynolds Number	$Re = ul\rho/\mu$	
M	Mach number	flow velocity/ sound velocity	
ρ	Mass density		kg/m^3
μ	Dynamic viscosity		
U_τ	Wall friction velocity		m/s
Y^+	Length scale	$y^+ = \nu/U_\tau$	
t^*	Wall time scale	$t^* = y^+/U_\tau$	s
αT	Over heat ratio	$\alpha T = (T - T_0)/T_0$	
C_f	Specific heat (unit mass)	$C = \frac{d}{dT}Q$	J / kg K
K_T	Thermal conductivity	$K_t = H/A\frac{\partial}{\partial x}T$	$watt/cmK$
k_d	Thermal diffusivity	$K_d = K_T/\rho C_f$	$m^2/second$
L, l	Length scale		m
δ	Boundary layer thickness		y^+

Magnetism

B	Magnetic flux density	$B = \mu H$	1 tesla=10^4 Gauss
B_s	Saturation magnetic flux density		same as above
H	Magnetic field intensity		A/m, oersted
μ_m	Magnetic dipole moment	$\mu_m = iA$	Am^2
ϕ	Magnetic Flux	$\phi = \oint_S B$	Wb, V s, Maxwell
M	Magnetization		A/M
μ	Permeability		Henry/M

References

[1] T. Abe, W.C. Messner and M.L. Reed, "Effective Methods to Prevent Stiction During Post-Release-Etch Processing," *Proceedings, IEEE Micro Electro Mechanical Systems Workshop, MEMS'95*, pp. 94–99, 1995.

[2] S. Abel, H. Freimuth, H. Lehr and H. Mensinger, "Defined Crystal Orientation of Nickel by Controlled Microelectroplating," J. Micromechanics and Microengineering, Vol. 4, pp. 47–54, 1994.

[3] C.H. Ahn and M.G. Allen, "A Fully Integrated Surface Micromachined Magnetic Microactuator with a Multilevel Meander Magnetic Core," *IEEE J. Micro Electro Mechanical Systems*, Vol. 2(1), pp. 15–22, 1993.

[4] R.L. Alley, G.J. Cuan, R.T. Howe and K. Komvopoulos, "The Effect of Release-Etch Processing on Surface Microstructure Stiction," *IEEE Solid-State Sensor and Actuator Workshop*, Hilton Head Island, SC, pp. 202-207, 1992.

[5] J.D. Anderson, Jr., Fundamentals of Aerodynamics, McGraw-Hill, Inc., 1991.

[6] N.C. Anderson and C.R. Grove Jr., U.S. Patent 4,279,707, 1981.

[7] M. Ataka, A. Omodaka and H. Fujita, "A biomimetic micro motion system - a ciliary motion system," *Technical Digest of Transducers '93*, pp. 38–41. 1993.

[8] S. Bart, T.A. Lober, R.T. Howe, J.H. Lang and M.F. Schlecht," Design Considerations for Micromachined Electrostatic Actuators," *Sensors and Actuators*, 14, pp. 269-292, 1988.

[9] I. Barycka and I. Zubel, "Silicon Anisotropic Etching in KOH-isopropanol Etchant," *Sensors and Actuators*, A 48, pp. 229-238, 1995.

[10] B. Gupta, R. Goodman, F. Jiang and Y.C. Tai, "Analog VLSI System for Active Drag Reduction," 1995.

[11] D. Bosch, et. al., "A silicon microvalve with combined electromagnetic/electrostatic actuation," *Sensors and Actuators*, A37–38, pp. 684-692, 1993.

[12] I.J. Busch-Vishniac, "The Case for Magnetically Driven Microactuators," *Sensors and Actuators*, A 33, pp. 207-220, 1992.

[13] D.M. Bushnell and K.J. Moore, "Drag reduction in nature," *Annu. Review Fluid Mechanics*, 23, pp. 65–79, 1991.

[14] -8. H. Busta, "Review-Vacuum Electronics –1992," *J. Micromech. Microeng.*, Vol. 2, pp. 43-74, 1992.

[15] P. Campbell, Permanent Magnet Materials and Their Applications, Cambridge Univ. Press, 1994.

[16] B.J. Cantwell, "Organized Motion in Turbulent Flow," *Annual Review of Fluid Mechanics*, 1981.

[17] F. Cardot, et. al., "Microfabrication of high-density arrays of microelectromagnets with on-chip electronics," *The 7th International Conference on Solid-State Sensors and Actuators, Transducer'91*, pp.32–35, 1993.

[18] F. Cardot, F. Perret and H. Tannenberger, "Alloy electrodeposition of magnetic microstructures," *42nd Meeting of International Society of Electrochemistry*, Montreux, Switzerland, 1991.

[19] E.E. Castellani, J.V. Powers and L.T. Romankiw, U.S. Patent 4,102,756, 1978.

[20] P.L. Castro and J.F.Campbell, "Stresses in thin films of aluminum," Ohmic Contacts to Semiconductors, Electrochemical Society, Inc., 1968.

[21] K.H.-L. Chau, C.D. Fung, P.R. Harris and J.G. Panagou, "High-Stress and Overrange Behavior of Sealed-Cavity Polysilicon Pressure Sensors", *Tech. Digest., Solid-State Sensor and Actuator Workshop*, Hilton Head, SC, p. 181, 1990.

[22] L.Y. Cheng, J.P. McVittie and K.C. Saraswat, "New Test Structure to Identify Step Coverage Mechanisms in Chemical Vapor Deposition of Silicon Dioxide," *Appl. Phys. Lett.*, 58(19), 1991.

[23] H. Choi, P. Moin and J. Kim, "Active turbulence control for drag reduction in wall-bounded flows," *J. Fluid Mech.*, Vol. 262, pp. 75-110, 1994.

[24] CRC Handbook of Tables for Applied Engineering Science, the Chemical Rubber Co., 1970.

[25] J.S. Danel and G. Delapierre, "Quartz: a Material for Microdevices," *Journal of Micromechanics and Microengineering*, v1, pp. 187-198, 1991.

[26] S. Dhawan, "Direct Measurements of Skin Friction," *NACA TN 2567*, 1953.

[27] S. Dushman, *Scientific Foundations of Vacuum Technique,* 2nd ed. (Wiley, New York, 1962), Chap. 1, p. 39.

[28] K.E. Drexler, Nanosystems, Wiley Interscience Publication, 1992.

[29] L.F. East, "Measurement of Skin Friction at Low Subsonic Speeds by the Raxor-Blade Technique," *R & M 3525*, Aero. Res. Counc. London, 1966.

[30] M. Esashi, N. Ura and Y. Matsumoto, "Anodic Bonding for Integrated Capacitive Sensors", *Proc. IEEE Workshop on Micro Electro-Mechanical Systems, MEMS'92*, Travemunde, Germany, February, 1992, pp. 43–48.

[31] S. Abel, H. Freimuth, H. Lehr and H. Mensinger, "Definied Crystal Orientation of Nickel by Controlling Microelectroplating," *Journal of Micromechanics and Microengineering,* 4, pp. 47-54, 1994.

[32] R. Frisch-Fay, Flexible Bars, Butterworth, 1962.

[33] B.P. Gogoi and C.H. Mastrangelo, "Post-processing Release of Microstructures By Electromagnetic Pulses," *1995 International Conference on Solid-State Sensors and Actuators*, Vol. I, pp. 214–217.

[34] H.D. Goldberg, K.S. Breuer and M.A. Schmidt, "A Silicon Wafer-Bonding Technology for Microfabricated Shear-Stress Sensors with Backside Contacts," *Technical Digest, Solid State Sensor and Actuator Workship,* Hilton Head Island, South Carolina, pp. 111-115.

[35] R.J. Goldstein, Fluid Mechanics Measurements, Hemisphere Publishing Co., p. 61, 1983.

[36] W. Gu, O. Robinson and D. Rockwell, "Control of Vortices on a Deltawing by leading edge injection," *AIAA Journal*, Vol. 31, No. 7, pp. 1177-1186, 1993.

[37] H. Guckel, "Surface Micromachined Pressure Transducers", *Sensors and Actuators*, A(28), pp. 133-146, 1991.

[38] H. Guckel, C. Rypstat, M. Nesnidal, J.D. Zook, D.W Burns, D.K. Arch, "Polysilicon Resonant Microbeam Technology for High Performance Sensor Applications", *Tech. Digest., Solid-State Sensor and Actuator Workshop*, Hilton Head, SC, p. 153, 1992.

[39] H. Guckel, J.J. Sniegowski, T.R. Christenson, S. Mohney, T.F. Kelly, "The Application of Fine-Grained, Tensile Polysilicon to Mechanically Resonant Transducers," *Sensors and Actuators*, A21, pp. 346-351, 1990.

[40] H. Guckel, T.R. Christenson, K.J. Skrobis, T.S. Jung, J. Klein, K.V. Hartojo and I. Widjaja, "A First Functional Current Excited Planar Rotational Magnetic Micromotor," *1993 IEEE Workshop on Micro Electro Mechanical-Systems*, pp. 7–11, 1993.

[41] H. Guckel, K.J. Skrobis, et. al., "Fabrication and testing of the planar magnetic micromotor", *Journal of Micromechanics and Microengineering*, Vol. 1, no. 4, pp. 135–138, 1991.

[42] T.J. Hanratty and J.A. Cambell, "Measurement of Wall Shear Stress," Fluid Mechanics Measurements, R.J. Goldstein, Ed. New York: Hemisphere, pp. 559-615, 1983.

[43] J.H. Haritonidis, "The Measurement of Wall Shear Stress," *Advances in Fluid Mechanics Measurements*, Springer-Verlag, pp. 229–261, 1989.

[44] H. Henmi, S. Shoji, Y. Shoji, K. Yosimi, M. Esashi, "Vacuum Packaging for Microsensors by Glass-Silicon Anodic Bonding", *Digest of Tech. Papers, 7th Int. Conf. on Solid State Sensors and Actuators*, Transducer '93, p. 584, Japan.

[45] T. Hirano, T. Furuhata and H.Fujita, "Dry releasing of electroplated rotational and overhanging structures," *IEEE Micro Electro Mechanical Systems Workshop*, Fort Lauderdale, Florida, USA, pp. 278–283, 1992.

[46] K. Hjort, J. Soverkvist and J.A. Schweitz, "Gallium Arsenide as a Mechanical Material," *J. Micromechanics and Microengineering,* v4, pp. 1–13, 1994.

[47] C.M. Ho and Y.C. Tai, "MEMS - Science and Technology," American Society of Mechanical Engineers Winter Annual Meeting, Chicago, Ill., pp. 39–49, 1994.

[48] J.P. Holman, Heat Transfer, McGraw-Hill Book Company, 1963.

[49] J.H. Hool, "Measurement of Skin Friction Using Surface Tubes," *Aircr. Eng.*, Vol. 28, p. 52, 1956.

[50] M.R. Houston, R. Maboudian and R.T. Howe, "Ammonium Fluoride Antistiction Treatments for Polysilicon Microstructures," *Proceedings, 1995 International Conference on Solid State Sensors and Actuators*, Stockholm, Sweden, 1995, Vol. I, pp. 210–213.

[51] J.J. Hsieh, "Influence of Surface-activated Reaction Kinetics on Low Pressure Chemical Vapor Deposition Conformality Over Micro Features", *J. Vac. Sci. Tech.*, A11(1), p. 78, 1993.

[52] J.B. Huang, C. Liu, F.K. Jiang, S. Tung, Y.C. Tai and C.M. Ho, "Fluidic Shear-Stress Measurement Using Surface-Micromachined Sensors," *IEEE 1995 Region 10 Conference on Microelectronics and VLSI*, Hong Kong, November 1995.

[53] J.B. Huang, C.M. Ho, S. Tung, C. Liu, Y.C. Tai, "Micro Thermal Shear Stress Sensor with and without Cavity Underneath," *IEEE Instrumentation/Measurement Tech. Conf., IMTC'95*, Waltham, MA, pp. 171–174, April 1995.

[54] T.J. Hubbard and E.K. Antonsson, "Emergent Faces in Crystal Etching," *Journal of Microelectromechanical Systems,* Vol. 3, No. 1, pp. 19–28, March 1994.

[55] A.K. Hussain and W.C. Reynolds, "The Mechanics of a Perturbation Wave in Turbulent Shear Flow," *AFOSR Scientific Report*, AFOSR 177SR-1655TR.

[56] J.D. Hunn and C.P. Christensen, "Ion Beam and Laser Assisted Micromachining of Single Crystal Diamond," *Solid State Technology*, v37 (12), pp. 57-62, 1994.

[57] E. Ibok and S. Garg, "A Characterization of the Effect of Deposition Temperature on Polysilicon Properties," Journal of Electro Chemical Society, Vol. 140, No. 10, pp. 2927–2937, Oct 1993.

[58] K. Ikuta, K. Hirowatari and T. Ogata, "Three-dimensional Micro Integrated Fluid Systems (MIFS) Fabricated by Stereo Lithography," *Proceedings, IEEE Micro Electro Mechanical Systems, 1994,* Oisa, Japan, pp. 1–6, 1995.

[59] M.C.Jeong and I.Busch-Vishniac, "A submicron accuracy magnetic levitation micromachine with endpoint detection," *Sensors and Actuators*, A29, pp. 225–234, 1991.

[60] J.W. Judy, R.S. Muller and H.H. Zappe, "Magnetic Micro-actuation of Polysilicon Flexure Structures," *1994 IEEE Solid-State Sensor and Actuator Workshop*, Hilton Head Island, SC, USA, pp. 43–48, 1994.

[61] J.W. Judy and R.S. Muller, "Magnetic Microactuation of Torsional Polysilicon Structures," *Proceedings, the 8th International Conference on Solid-State Sensors and Actuators,* Stockholm, Sweden, Vol. 1, pp. 332-335, 1995.

[62] H.T. Kim, S.J. Kline and W.C. Reynolds, "The Production of Turbulence near a Smooth Wall in a Turbulent Boundary," Vol. 22, pp. 473–537, 1990.

[63] S.J. Kline, "The Role of Visualization in the Study of the Structure of the Turbulent Boundary Layer," Lehigh Workshop on Coherent Structure of Turbulent Boundary Layers," Ed. C.R. Smith, D.E. Abbott, pp. 1–26, 1978.

[64] A.G. Kravchenko, H. Choi and P. Moin, "On the relation of streamwise vortices to wall skin friction in turbulent boundary layers," *Phys. Fluids*, A 5 (12), pp. 3307–3309, December 1993.

[65] P. Krulevitch, R.T. Howe, G.C. Johnson and J. Huang, "Stress in undoped LPCVD polycrystalline silicon," *6th International Conference on Sensors and Actuators, Transducer '91"*, p. 949, 1991.

[66] W. Ko, Q. Wang and Q.H. Wu, "Long Term Stable Capacitive Pressure Sensor for Medical Implant," *Digest of Tech. Papers, 7th Int. Conf. on Solid State Sensors and Actuators, Transducer '93*, p. 592, Japan.

[67] R. Legtenberg, J. Elders and M. Elwenspoek, "Stiction of Surface Micromachined Structures After Rinsing and Drying: Model and Investigation of Adhesion Mechanism," *Proceedings, 1993 International Conference on Solid-State Sensors and Actuators*, pp. 198-201, 1993.

[68] L. Lin, K.M. McNair, R.T. Howe and A.P. Pisano, "Vacuum Encapsulated Lateral Micro-resonators," *Digest of Tech. Papers, 7th Int. Conf. on Solid State Sensors and Actuators, Transducer '93*, p. 270, 1993.

[69] C. Liu, T. Tsao, Y.C. Tai and C.M. Ho, "Surface Micromachined Magnetic Actuators", *Proceedings, IEEE Micro Electro Mechanical Systems Workshop, MEMS'94*, Oiso, Japan, pp. 57–62, 1994.

[70] C. Liu and Y.C. Tai, "Studies on the Sealing of Micromachined Cavities using Chemical Vapor Deposition Materials," Technical Digest, *Solid-State Sensor and Actuator Workshop*, Hilton Head Island, South Carolina, pp. 103–106, 1994.

[71] C. Liu, T. Tsao, Y.C. Tai, W.H. Liu, P. Will and C.M. Ho, "A Micromachined Permalloy Magnetic Actuator Array for Micro Robotics Assembly Systems," *Proceedings, 8th International Conferene on Solid State Sensors and Actuators, Transducer 95"*, Stockholm, Sweden, Vol. 1, pp. 328–331 , 1995.

[72] C. Liu, Y.C. Tai and R. Gamble, "All Silicon Micromachined Atomic Force Microscope Probes," *Abstract, International Conference on Scanning Tunneling Microscope, STM'93*, Beijing, China, 1993.

[73] J. Liu, Y.C. Tai, K.C. Pong, Y. Zohar and C.M. Ho, "Micromachined Channel/Pressure Sensor Systems for Micro Flow Studies," *Digest of Tech. Papers, 7th Int. Conf. on Solid State Sensors and Actuators, Transducer '93*, Japan, p. 995, 1993.

[74] J. Liu and Y.C. Tai, J. Lee, K.C. Pong, Y. Zohar and C.M. Ho, "*In Situ* Monitoring and Universal Modelling of Sacrificial PSG Etching Using Hydrofluoric Acid," *Proc. IEEE Workshop on Micro Electro Mechanical Systems, MEMS'93*, Fort Lauderdale, FL, 1993, p. 71.

[75] J.Liu, Ph.D. Thesis, California Institute of Technology, 1995.

[76] L. Lofdahl, G. Stemme, and B. Johansson, "A Sensor based on Silicon Technology for Turbulence Measurements," *J. Physics E: Sci. Instrument*, Vol. 22, pp. 391–393, 1989.

[77] D.G. Mabey, L. Gaudet, "Some Performance of Small Skin Friction Balances at Supersonic Speeds," *J. Aircr.*, Vol. 12, pp. 819–825, 1975.

[78] R.D. MacInnis and K.V. Gow, "Tensile Strength and Hardness of Electrodeposited Nickel-Iron Alloy Foil," *Plating*, pp. 135-136, February 1971.

[79] C. H. Mastrangelo, Master Thesis, University of California at Berkeley, Berkeley, CA, 1987.

[80] C.H. Mastrangelo and C.H. Hsu, "A Simple Experimental Technique for the Measurement of the Work of Adhesion of Microstructures," *IEEE Solid-State Sensor and Actuator Workshop*, Hilton Head Island, SC, pp. 208-212, 1992.

[81] C.H. Mastrangelo and G.S. Saloka, "A Dry-Release Method Based on Polymer Columns for Microstructure Fabrication," *Proceeding, IEEE Micro Electro Mechanical Systems Workshop, MEMS'93*, pp. 77-81, 1993.

[82] Q. Mei, T. Tamagawa, C. Ye, Y. Lin, S. Zurn, D.L. Polla, "Planar-processed Tungsten and Polysilicon Vacuum Microelectronic Devices with Integral Cavity Sealing", *Journal of Vacuum Science and Technology*, B11(2), p. 493, 1993.

[83] J.E. Mitchell, "Investigation of Wall Turbulence Using a Diffusion Controlled Electrode," Ph.D. thesis in Chemical Engineering, University of Illinois at Urbana-Champaign, 1965

[84] J.E. Mitchell and T.J. Hanratty, "A Study of Turbulence at a wall using an Electrochemical Wall Shear Stress Sensor," Journal of Fluid Mechanics, Vol. 26, part. 1, pp. 199-221, 1966.

[85] M.J. Moen and S.P. Schneider, "The Effect of Sensor Size and Substrate Properties on the Performance of Flush-Mounted Hot-film Sensors," Thermal Anemometry -1993, D.E. Stock, S.A. Sherif, A.J. Smits and J. Davidson, Eds., ASME, pp. 249–261, 1993.

[86] G.T. Mulhern, D.S. Soane and R.T. Howe, "Supercritical Carbon Dioxide Drying of Microstructures," *Proceedings, 1993 International Conference on Solid-State Sensors and Actuators*, p. 296, 1993.

[87] R.S. Muller and T.I. Kamins,
Device Electronics for Integrated Circuits, Wiley, 1977.

[88] Olin Hunt Specialty Products, Inc., Pad Etchant type 777.

[89] M. Orpana and A.O. Korhonen, "Control of Residual Stress of Polysilicon Thin Films by Heavy Doping in Surface Micromachining," *1991 International Conference on Solid State Sensors and Actuators*, pp. 957-960, 1991.

[90] L. Parameswaran, V. M. McNeil, M. A. Huff, M.A. Schmidt, "Sealed-Cavity Microstructure Using Wafer Bonding Technology," *Digest of Tech. Papers, 7th Int. Conf. on Solid State Sensors and Actuators, Transducer '93*, p. 274, Japan.

[91] K.E. Petersen, "Silicon as a Mechanical Material," *Proceedings of the IEEE*, Vol. 70, No. 5, pp. 420–457, May 1982.

[92] K.E. Petersen, "MEMS: What Lies Ahead", *1995 International Conf. on Solid-State Sensors and Actuators, Transducer'95*, Stockholm, Sweden, pp. 894–897, 1995.

[93] K. Petersen, J. Brown and R. Legtenberg, "High-Precision, High-Performance Mass Flow Sensor with Integrated Laminar Flow Micro-Channels," Proceedings, *1985 Int. Conf. on Solid-State Sensors and Actuators*, pp. 361–363, 1985.

[94] J.H. Preston, "The Determination of Turbulent Skin Friction by Means of Pitot Tubes," *J. R. Aero. Soc.*, Vol. 58, pp. 109–121, 1953.

[95] W. Riethmuller and W. Benecke, "Thermally Excited Silicon Microstructures," *IEEE Transaction on Electron Devices*, Vol. 35, No. 6, pp. 758-763, 1988.

[96] K. Rinoie, "Experiments on a 60-degree Delta Wing with Vortex Flaps and Vortex Plates," *Aeronautical Journal*, Vol. 97 (961), pp. 33-38, 1993.

[97] M.W. Rubesin, A.F. Okuno, G.G. Mateer and A. Brosh, "A Hot-Wire Surface Gage for Skin Friction and Separation Detection Measurements," *NASA TM X-62*, p. 465, 1975.

[98] J.B. Sampsell, "The Digital Micro-mirror Device and Its Application on Projection Display," *Technical Digest, 1993 International Conference on Soild-State Sensors and Actuators,* Yokohama, Japan, pp. 24–27, 1993.

[99] V.A. Sandborn, "Surface Shear-Stress Fluctuations in Turbulent Boundary Layers," *Second Symp. on Turbulent Shear Flows*, London, 1979.

[100] K.C. Saraswat and H. Singh, "Thermal Oxidation of Heavily Phosphorous-Doped Thin Films of Polycrystalline Silicon," *J. Electrochem. Soc.*, Vol. 129, pp. 2321-2326, 1982.

[101] M.A. Schmidt, R.T. Howe, S.D. Senturia and J.H. Haritonidis, "Design and Calibration of a Microfabricated Floating-Element Shear-Stress Sensor," *IEEE Trans. Electronics Devices*, 35(6), pp. 750–757, 1988.

[102] M. Sekimoto, H. Yoshihara and T. Ohkubo, "Silicon nitride single-layer X-ray mask," *J. Vac. Sci. Tech.*, vol.21, p. 1017, 1982.

[103] J. Shajii, K.Y. Ng and M.A. Schmidt, "A Microfabricated Floating-Element Shear-Stress Sensor Using Wafer-Bonding Technology," *J. Microelectromechanical Sys.*, Vol. 1, No. 2, 1992.

[104] K. Shimaoka, "Micro Pressure Sensor," *Tech. Digest of 9th Sensor Symposium*, pp. 47-50, 1990.

[105] J.K. Stanley, Electrical and Magnetic Properties of Metals, American Society for Metals, 1963.

[106] G.N. Stemme, "A Monolithic Gas Flow Sensor with Polyimide as Thermal Insulator," *IEEE Trans. Elec. Devices*, ED-33, p. 1470, 1986.

[107] V.L. Streeter, Fluid Mechanics, McGraw Hill, 1966.

[108] S.M. Sze, VLSI Technology, 2nd Ed., McGraw-Hill, 1988.

[109] Y.C. Tai and R.S. Muller, "IC-Processes Electrostatic Synchronous Micromotors," *Sensors and Actuators,* Vol. 20 (1-2), pp. 49-55, 1989.

[110] Y.C. Tai and R.S. Muller, "Lightly-Doped Polysilicon Bridge as a Flow Meter," *Sensors and Actuators*, Vol. 15, pp. 63-75, 1988.

[111] Y.C. Tai and R. S. Muller, "Fracture Strain of LPCVD Polysilicon," *Technical Digest, IEEE Solid-State Sensors and Actuators Workshop*, Hilton Head Island, SC, USA, pp. 88-91, 1988.

[112] T. Tagaki and N. Nakajima, "Architecture Combination by Micro Photoforming Process," *Proceedings, IEEE Micro Electro Mechanical Systems, 1994,* Oisa, Japan, pp. 211–216, 1995.

[113] M. Takahashi, "Induced Magnetic Anisotropy of Evaporated Films Formed in a Magnetic Field," J. Appl. Phys., Supplement to Vol. 33, No. 3, pp. 1101–1106, 1962.

[114] N. Takeshimo, K.J. Gabriel, M. Ozaki, J. Takahashi, H. Horiguchi and H. Fujita, "Electrostatic parallelogram Actuators," *Proceedings, 1991 International Conference on Solid-State Sensors and Actuators*, pp. 63-66, 1991.

[115] W.C. Tang, T.C. Nguyen and R.T. Howe, "Laterally driven polysilicon resonant microstructures," *Sensors and Actuators*, 20, pp. 25-32, 1989.

[116] V. Temesvary, S. Wu, W.H. Hsieh, Y.C. Tai and D.K. Miu, "Design, Fabrication and Testing of Micromachined Electromagnetic Microactuators for Rigid Disk Drives" *IEEE Journal of Micro Electro Mechanical Systems*, Vol. 4, No. 1, pp. 18–27, March, 1995.

[117] S. Timoshenko, "Analysis of Bi-metal Thermostats", *Journal O.S.A and R.S.I 11*, pp. 233–255, September 1925.

[118] O. Tobata, "Fast-Response Silicon Flow Sensor with an On-Chip Fluid Temperature Sensing Element," *IEEE Trans. Elec. Devices*, Vol. 33, pp. 361–365, 1986.

[119] G.A. Tokaty, A History and Philosophy of Fluid Mechanics, Dover Publications, New York, 1994.

[120] L. Tong, M. Mehregany and L.G. Matus, "Amorphous Silicon Carbide Films by Plasma-Enhanced Chemical Vapor Deposition," *Proceedings, IEEE 1993 Micro Electro Mechanical Workshop, MEMS'93*, pp. 242–247, 1993.

[121] Q.Y. Tong and U. Gösela, "Semiconductor Wafer Bonding: Recent Developments," *Materials Chemistry and Physics,* 37, pp. 101–127, 1994.

[122] Cr mask etchant, Transene Co., USA.

[123] S. Tung, personal communication.

[124] S. Tung, W. Hong, J.B. Huang, C.M. Ho, C. Liu, Y.C. Tai, "Control of Streamwise Vortices in 2-D Channel Flow," *Proceedings, Sixth Asian Congress on Fluid Mechanics*, Hong Kong, Vol. 2, p. 805, May 1995.

[125] S. Tung, W. Hong, J.B. Huang, C.M. Ho, C. Liu, Y.C. Tai, "Control of a Streamwise Vortex by a Mechanical Actuator," *Tenth Symp. on Turbulent Shear Flows*, Penn. State. Univ. University Park, PA, Vol. I, pp. 1/19-1/24, August 14-16, 1995.

[126] B.W. van Oudheusden and A.W. van Herwaarden, "High Sensitivity 2-D Flow Sensor with an Etched Thermal Isolation Structure," *Sensors and Actuators*, A 21–23, pp. 425–430, 1990.

[127] B.W. van Oudheusden, "Silicon Thermal Flow Sensors," *Sensors and Actuators*, A. 30, pp. 5–26, 1992.

[128] B. Wagner, W. Benecke, G. Engelmann and J. Simon, "Microactuators with Moving Magnets for Linear, Torsional or Multi-axial Motion," *Sensors and Actuators*, A(32), pp. 598–603, 1992.

[129] Z.Y. Wang, "Experimental study of a wall shear stress sensor based on a porous element," *Experiments in Fluids*, 14, pp. 153–157, 1993.

[130] K. Watanabe and H. Komiyama, "Micro/Marcocavity Method Applied to the Study of the Step Coverage Formation Mechanism of SiO2 Films by LPCVD," *J. Electrochem. Soc.*, Vol. 137, No. 4, p. 1222, 1990.

[131] R.C. Weast, CRC Handbook of Chemistry and Physics, 67th ed., CRC Press, 1988.

[132] S. Wolf and R.N. Tauber, Silicon Processing for the VLSI Era, Volume 1 - Process Technology, Lattice Press, 1986.

[133] K. Yanagisawa, A. Tago, T. Ohkubo and H. Kuwano, "Magnetic Micro Actuator," *Proceedings of IEEE Micro Electro Mechanical Systems*, Nara, Japan, pp. 120-124, 1990.

[134] Y. Yee, K. Chun and J.D. Lee, "Polysilicon Surface Modification Technique to Reduce Sticking of Microstructures," *1995 International Conference on Solid-State Sensors and Actuators*, pp. 206–209.

[135] W.C. Young, Roark's Formulas for Stress and Strain, 6th Ed., McGraw-Hill, 1989.

[136] S.W. Yuan, Foundations of Fluid Mechanics, Prentice Hall, 1972.

[137] S. Zurn, Q. Mei, C. Ye, T. Tamagawa and D.L. Polla, *1991 Sealed Vacuum Electronic Devices by Surface Micromachining, Proc. International Electronics Device Meetings (IEDM) '91*, pp. 205–208, Washington D.C., 1991.